IMPROVEMENTS TOWARD HIGH-EFFICIENCY VERTICAL-CAVITY SURFACE-EMITTING LASERS

A DISSERTATION SUBMITTED

TO THE DEPARTMENT OF ELECTRICAL ENGINEERING

AND THE COMMITTEE ON GRADUATE STUDIES

OF STANFORD UNIVERSITY

IN PARTIAL FULFILLMENT OF THE REQUIREMENTS

FOR THE DEGREE OF

DOCTOR OF PHILOSOPHY

Kenneth Louis Bacher

June 1995

I certify that I have read this dissertation and that in my opinion it is fully adequate, in scope and quality, as a dissertation for the degree of Doctor of Philosophy.

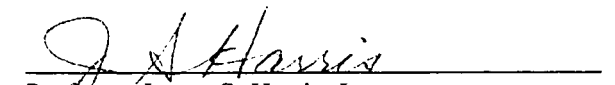

Professor James S. Harris, Jr.
Principal Advisor

I certify that I have read this dissertation and that in my opinion it is fully adequate, in scope and quality, as a dissertation for the degree of Doctor of Philosophy.

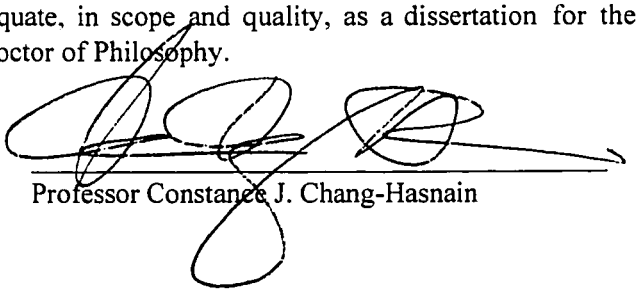

Professor Constance J. Chang-Hasnain

I certify that I have read this dissertation and that in my opinion it is fully adequate, in scope and quality, as a dissertation for the degree of Doctor of Philosophy.

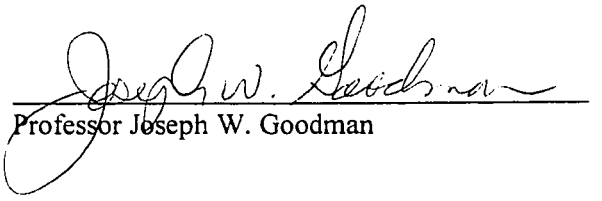

Professor Joseph W. Goodman

Approved for the University Committee on Graduate Studies:

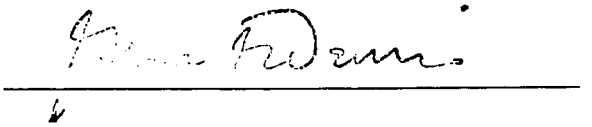

Abstract

Vertical-cavity surface-emitting lasers (VCSELs) have been proposed for many applications including communications, two-dimensional optical interconnects, optical computing, and image processing. The vertical optical cavity and surface-normal output provide advantages in two-dimensional packing density, output beam size and quality, and fabrication ease as compared with edge-emitting designs. Furthermore, these devices inherently operate in a single longitudinal mode due to the very short optical cavities.

The vertical geometry, however, places severe demands on the growth and design of high-efficiency lasers. The large longitudinal mode spacing, for example, places the tolerances on layer thickness control at or beyond the limits of conventional crystal growth calibration methods. If the spectral position of the cavity mode, determined by the cavity thickness, does not overlap correctly with the material gain, the laser will have a high threshold current if it operates at all. Additionally, the multiple heterointerfaces of the Distributed Bragg Reflector (DBR) mirrors cause the devices to exhibit high series resistance. This reduces efficiency not only due to the electrical power lost, but also because the ohmic heating seriously degrades the intrinsic optical performance of these lasers.

This thesis describes improvements in crystal growth techniques and design of VCSELs to achieve high-efficiency operation. An in-situ growth characterization technique was developed to accurately position the cavity mode of a VCSEL at the designed wavelength during growth. Compositional grading and modulation doping are utilized to decrease the resistance of the p-type DBR mirror. A wet-etching process was developed for realizing an intracavity contact to bypass the resistance of the n-type mirror. These improvements should combine to yield high-efficiency vertical-cavity surface-emitting lasers.

Acknowledgments

I am grateful for help and support from a number of people during my studies at Stanford. First, I would like to thank my advisor, Professor Jim Harris, for creating an outstanding environment to conduct research. In addition to assembling a talented group of students, postdocs, and visitors from electrical engineering, applied physics and material science, he has made an incredible array of equipment and facilities available for our use. While offering valuable insights and direction, he also affords his students a remarkable degree of freedom with which to seek out and pursue research topics.

My associate advisor, Professor Connie Chang-Hasnain, has also been very helpful in the development of this work. I have learned a lot both from her course on semiconductor lasers and collaborations with her research group. I would also like to thank Professors Joseph Goodman and Hector Garcia-Molina for sitting on my orals committee, especially since my defense took place only two days before winter break, and Dr. Goodman again for agreeing to read my dissertation.

I would like to thank the members of the Harris group as a whole for their support. I have enjoyed the technical discussions, impromptu stairway/hallway bull sessions, and general camaraderie- like being part of a very large family. I also gratefully acknowledge the outstanding administrative support from Gail Chun-Creech, Susie Burns, and Lu Miao who managed to keep everything running- many headaches have been cured and much time saved with their (continued) help.

A few of my colleagues in particular deserve special recognition for there contributions to this work: Lars Eng, for collaborations on VCSELs, Mike Larson, for insights into etching, and Bardia Pezeshki, for help with in-situ measurements.

Finally, I would like to thank my family for their support and my girlfriend, Dana Cunningham, for listening to my babbling and informing me when I had completely lost perspective.

Table of Contents

List of Tables

List of Figures

1. Introduction

Vertical-Cavity Surface-Emitting Lasers (VCSELs) have been considered for many applications, including; fiber optic communications,[1] two-dimensional optical interconnect, optical computing and image processing. Depending on the specific application, different operating characteristics- threshold current, threshold voltage, differential efficiency, output power, or series resistance- must be optimized. Because these factors are interrelated, optimizing one characteristic often requires trade-offs with others. One might easily sacrifice high output power and differential efficiency, for example, to obtain a device with extremely low threshold current. Because all of these operating characteristics influence the total electrical to optical power conversion efficiency, however, it is often used as a global performance metric to compare device designs without regard to a specific application.

This thesis is concerned with the factors that influence the efficiency of vertical-cavity surface-emitting lasers. Chapter 2 provides a general background and motivation for the work, including an introduction to semiconductor lasers, specific components of VCSELs, the crystal growth technology, and problems for achieving high-efficiencies in these devices. The next three chapters describe solutions to these problems. Chapter 3 presents an in-situ growth correction technique that enables the operating wavelength of the VCSEL to be accurately positioned so that it coincides with the peak of the material gain. Chapter 4 demonstrates an improved mirror design, employing compositional grading and p-n modulation doping at the heterojunction interfaces to reduce the electrical and optical losses of the p-type Distributed Bragg Reflector (DBR) mirror. Chapter 5 demonstrates a selective etching and undercut process to achieve a very low resistance n-type intracavity contact with lateral current confinement. Finally, Chapter 6 concludes this work with a summary of accomplishments and suggestions for further work.

2. Background

After a brief introduction to lasers in general, information specific to vertical-cavity surface-emitting lasers in particular will be presented. An overview of molecular beam epitaxy, the crystal growth technique used for all of the devices presented in this thesis, follows. Finally, the problems which must be solved to achieve high-efficiency VCSELs will be given as motivation for this work

2.1 Laser Background

A laser basically consists of a gain medium surrounded by mirrors configured to provide positive feedback, Figure 2-1. Energy input to the gain region to causes it to be in a non-equilibrium state necessary to provide amplification of an optical signal. This non-equilibrium state is termed a population inversion because more high-energy states are occupied than low energy ones. One (or both) of the mirrors is made to partially transmit the circulating light as output.

The excited population in the gain medium will decay toward its thermal equilibrium value by spontaneously emitting photons with random direction and phase. An existing photon with the right energy can also stimulate downward transitions. In this case, however, the emitted photon is released with the same direction and phase as the one which stimulated the transition. The rate of spontaneous emission for a given material is dependent on the degree of deviation from thermal equilibrium, whereas the

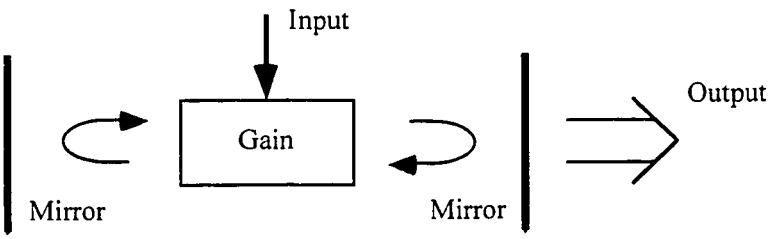

Figure 2-1: Schematic of a basic laser.

stimulated emission is additionally proportional to the incident photon flux. The role of the optical feedback, then, is to build up the photon density in the cavity to preferentially select stimulated emission transitions. This gives rise to the coherent output from the laser. Although the excited population can also decay through non-radiative means, once the photon density in the cavity is high enough, the decay rate of the excited state(s) will be dominated by the stimulated emission rate.

2.1.1 Fabry-Perot Cavities and Laser Threshold

The simple feedback mechanism of Figure 2-1, consisting of two plane parallel mirrors separated, by a length, L, is termed a Fabry-Perot cavity. It is interesting to examine the properties of the Fabry-Perot cavity since they have such a profound effect on the properties of the resulting laser. The mirrors, for the moment considered lossless, will be characterized by their amplitude reflection and transmission coefficients, r and t. With reference to Figure 2-2, the relationships between the amplitude of the incident and circulating fields can be related by,

$$E_{circ} = it_1 E_{inc} + r_1 r_2 e^{i2\gamma L} E_{circ}, \tag{2-1}$$

where the additional factor of i in the transmission accounts for the finite thickness of the mirror given that the reference planes for the right- and left-side reflections from the mirror are taken at the respective surfaces.[2]

The exponent in the propagation term can be split into its real and imaginary components related to the round-trip amplitude and phase change. The ratio of the fields

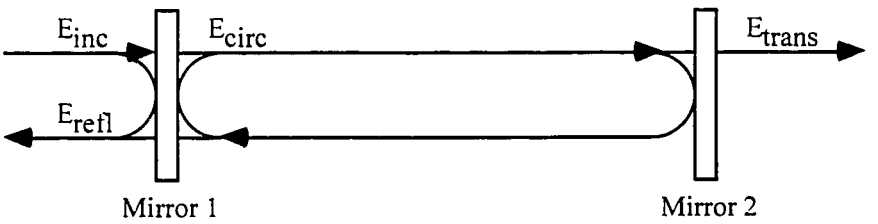

Figure 2-2: Schematic of a Fabry-Perot cavity.

then becomes,

$$\frac{E_{circ}}{E_{inc}} = \frac{it_1}{1 - r_1 r_2 e^{(g-\alpha)L} e^{i2k_0 nL}}, \tag{2-2}$$

where the g and α are the power gain (modal) and loss coefficients and $k_0 = 2\pi/\lambda$. If the denominator of equation (2-2) is equal to zero, a self-sustaining E_{circ} can be maintained with no additional input. This is the condition for the lasing threshold wherein a large circulating intensity can build up into the lasing mode in the cavity from a relatively small amount of spontaneous emission.

The threshold condition can be separated into constraints on the round-trip amplitude and phase change,

$$r_1 r_2 e^{(g-\alpha)L} = 1 \quad \Rightarrow \quad g_{th} = \alpha + \frac{1}{2L} \ln\left(\frac{1}{R_1 R_2}\right) \text{ and} \tag{2-3}$$

$$e^{i2k_0 nL} = 1 \quad \Rightarrow \quad nL = m\lambda/2. \tag{2-4}$$

The amplitude constraint dictates that the threshold gain must equal the losses, including output coupling, and the phase constraint dictates that the optical length of the cavity must be an integral number of half wavelengths.

It is important to note that the effect of the cavity resonance can be seen in the reflection from a passive cavity. The amplitude of the reflected field will be the sum of the reflection of the incident field and the transmission of the circulating field at mirror 1,

$$E_{refl} = r_1 E_{inc} + it_1 r_2 E_{circ} \quad \Rightarrow \quad \frac{E_{refl}}{E_{inc}} = r_1 - \frac{t_1^2 r_2 e^{i2\gamma L}}{1 - r_1 r_2 e^{i2\gamma L}}. \tag{2-5}$$

It can easily be shown that, regardless of the values of r_1, r_2, and α, the intensity of the reflection will be a minimum whenever $\sin(2k_0 nL) = 0$, which is equivalent to the resonance condition in equation (2-4). Thus, except for a small shift due to a slight, carrier-induced index change, the lasing wavelength can be determined by the reflectivity dip in a measurement of the passive cavity.

2.1.2 Semiconductor Lasers

Gain in semiconductor lasers is provided by excess carrier populations. If the material has a direct bandgap, it will exhibit gain for photon energies which satisfy

$$E_g < h\nu < F_n - F_p, \tag{2-6}$$

where E_g is the bandgap of the semiconductor, $h\nu$ is the photon energy, and F_n and F_p are the quasi-Fermi levels for the electrons and holes.[3] In an electrically operated semiconductor laser, the excess carriers are supplied by injection across a forward-biased P-N (or P-I-N) diode.

For a simple edge-emitting laser such as that shown in Figure 2-3, the cavity is defined by the cleaved endfaces of the crystal, which provide about 30% power reflectivity. The carriers are injected in the vertical direction and the transverse extent of the waveguide mode is controlled by the material composition in the vertical direction and either gain-guiding or device processing laterally. The high material gain allows lasers to operate with cavity lengths as short as a few 100 microns even with the gain from a relatively thin gain region coupling into only a few percent of the modal volume.

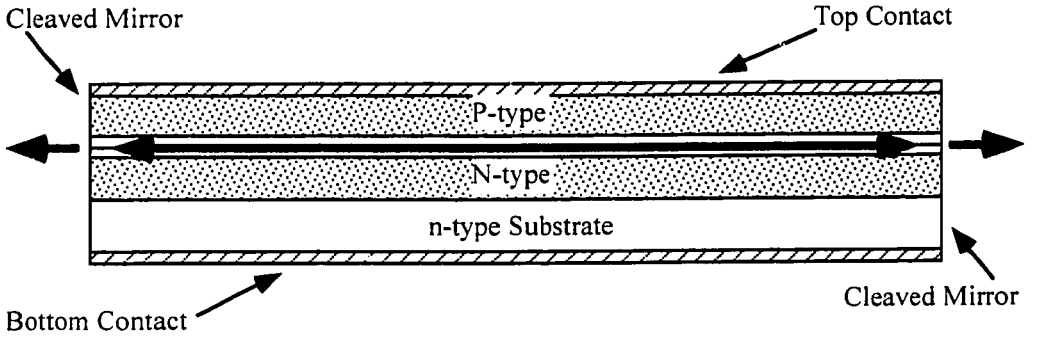

Figure 2-3: Schematic of an edge-emitting semiconductor laser.

2.1.3 Efficiency

There are three different efficiency characteristics generally used to describe semiconductor lasers: internal quantum efficiency, differential quantum efficiency, and

wallplug efficiency. The internal quantum efficiency, η_i, is the percentage of injected carriers that recombine radiatively in the gain region. All additional carriers injected into the active region beyond that required to reach threshold will recombine through stimulated emission, so well above threshold the internal quantum efficiency should approach the percentage of injected carriers that reach the active region. For a well designed active region and good material quality, η_i can be made greater than 90%. The differential quantum efficiency, η_d, is the differential increase in photons emitted due to an increase in the number of injected carriers. When multiplied by hv/q to convert the units to mW/mA, it is the slope of the L-I curve and is often referred to as the slope efficiency, η_s. The internal efficiency is the percentage of injected carriers which are converted to photons, so the differential quantum efficiency is just η_i times the escape probability of a photon. Since an emitted photon can leave the lasing mode either through optical loss (by absorption, scattering or diffraction) or output coupling, the escape probability will be the output coupling divided by the sum of the loss and the output coupling,

$$\eta_d = \eta_i \left(\frac{\ln(\frac{1}{R_1 R_2})}{2\alpha_0 L + \ln(\frac{1}{R_1 R_2})} \right). \tag{2-7}$$

Finally, the wallplug efficiency or total external quantum efficiency is simply the total optical power output divided by the total electrical power input,

$$\eta_{wp} = \frac{P_{out}}{P_{in}}. \tag{2-8}$$

These terms will be examined more closely in their application to vertical-cavity surface-emitting lasers in section 0.

2.2 Vertical-Cavity Surface-Emitting Lasers

Although edge-emitting lasers and vertical-cavity lasers share fundamental operating principles, geometry differences raise different concerns in the design of high-efficiency devices. For VCSELs, the current injection and optical propagation are in the same direction, normal to the wafer surface, creating tradeoffs for efficient optical and electrical optimization of the devices. Furthermore, the short cavity length which is defined by the epitaxial growth makes the device characteristics very dependent on the layer thickness accuracy. Additional differences arise from the distributed nature of the mirrors.

2.2.1 Distributed Bragg Reflectors

Mirrors for VCSELs generally rely on the reflections at the interfaces between multiple layers of material to achieve very high reflectivity. A schematic of such a mirror, called a Distributed Bragg Reflector (DBR), is shown in Figure 2-4. While the reflection at each of the material interfaces may be small, the aggregate reflectivity from a multilayer stack can approach unity.

At normal incidence, the amplitude reflectance at an interface from material 1 to material 2 is given by the Fresnel reflection coefficient.[4]

$$\rho = \frac{n_1 - n_2}{n_1 + n_2} = \frac{1 - n_2/n_1}{1 + n_2/n_1}, \tag{2-9}$$

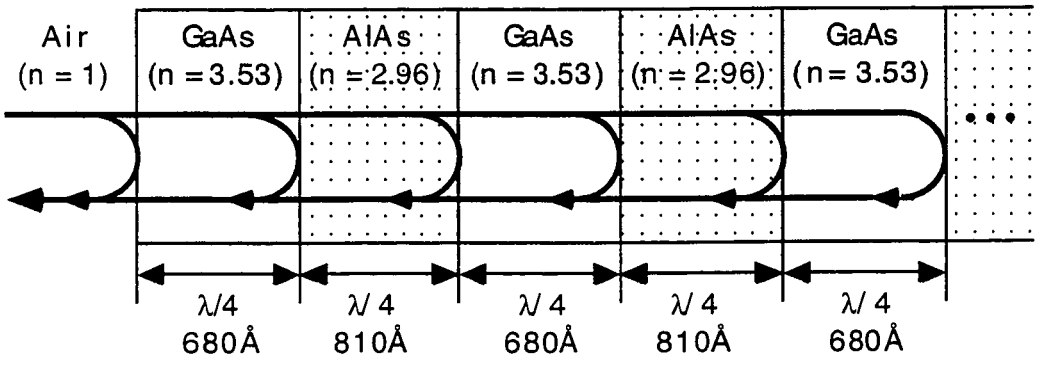

Figure 2-4: Schematic of a GaAs/AlAs DBR mirror centered at 960 nm.

where n_1 and n_2 are the indices of refraction for the two materials. As can be seen, the closer the indices, the smaller the reflectance from the interface. For the materials of interest for this work, GaAs and AlAs, the indices are about 3.54 and 2.96, yielding an amplitude reflectivity of 8.9% or a power reflectivity, $R = \rho^2$, of 0.8%. Although this is a very small value, if the thickness of layers in a multiple layer stack is adjusted so that each is one quarter wavelength, the reflectance from each interface adds in phase to produce a very high total reflectivity. In general, calculation of the reflectivity of a multilayer stack must be accomplished with a numerical technique, such as that of section 3.1. For the specific case of alternating quarter wave layers of two materials, however, a closed-form solution for the maximum reflectivity exists and can be approximated as,[5]

$$R_{max} \approx \left[1 - 2\left(\frac{n_i}{n_t}\right)\left(\frac{n_L}{n_H}\right)^{2p}\right]^2 \approx 1 - 4\left(\frac{n_i}{n_t}\right)\left(\frac{n_L}{n_H}\right)^{2p}, \tag{2-10}$$

where n_i and n_t are the refractive indices for the incident and transmitted media, n_L and n_H are the indices for the low and high index mirror layers, and p is the number of layer pairs. For a fifteen pair GaAs/AlAs mirror on a GaAs substrate (n_i = 1.00 and n_t = 3.53) for example, the peak reflectivity is about 99.4%.

The resonant nature of these mirrors which gives rise to very high reflectivity, also causes the reflectivity and phase to be wavelength dependent. This is illustrated in Figure 2-5 for a 20 period GaAs/AlAs DBR mirror. The reflectivity remains very close to 1 for wavelengths from 9300 Å to 9900 Å. However, as the constituent layers begin to look less and less like quarter wave thicknesses, the reflectivity starts decreasing rapidly. The first node on either side of the center wavelength is approximately equally spaced in energy from the center.[6] As a result, the center wavelength can be determined from the positions of the nodes by

$$\frac{1}{\lambda_0} = \frac{1}{2}\left(\frac{1}{\lambda_1} + \frac{1}{\lambda_2}\right), \tag{2-11}$$

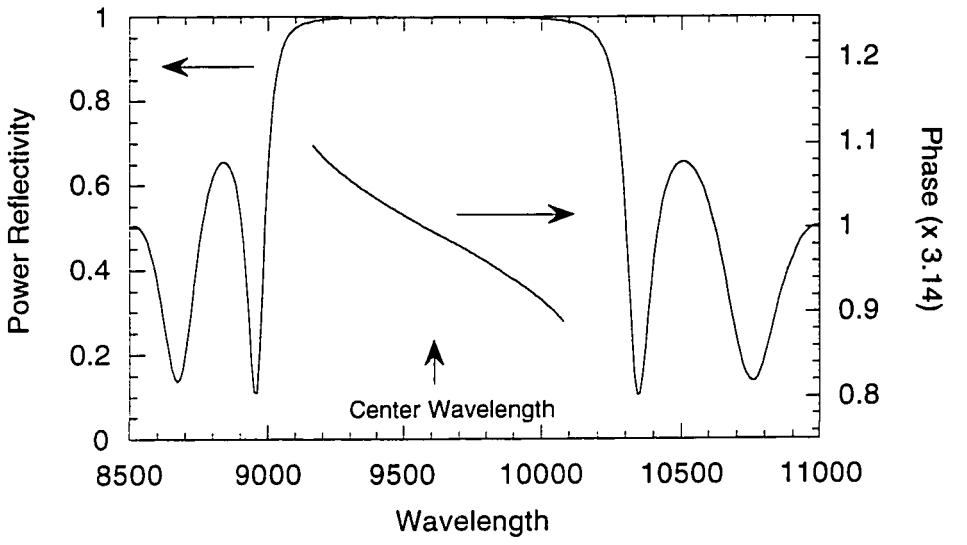

Figure 2-5: Reflectivity and phase change for a 20 period GaAs/AlAs DBR mirror.

where λ_0 is the center wavelength of the mirror and λ_1 and λ_2 are the wavelengths of the two nodes.

In the region of high reflectivity, the reflected phase varies linearly with wavelength. This linear phase response can be interpreted as coming from propagation of a distance, L, though a medium with index, n, in front of a perfect mirror, one with flat phase characteristics. The phase associated with the round-trip propagation is,

$$\phi = 2\left(\frac{2\pi}{\lambda} nL\right). \tag{2-12}$$

Taking the derivative of the phase change with respect to wavelength, one finds the effective displacement of the reflection to be,

$$nL = -\frac{\lambda^2}{4\pi}\left(\frac{d\phi}{d\lambda}\right). \tag{2-13}$$

As will be demonstrated in section 3.1.2, this displacement, is also the length over which the optical intensity decays to 1/e of its value at the true surface of the mirror. As such, it is a measure of the optical penetration depth into the mirror.

A closed-form solution for $d\phi/d\lambda$ at the reflectivity maximum[7] reveals it to be inversely proportional to the index difference between the two layers. This dependence on the difference of the indices is not surprising: the closer the indices, the lower the reflection from each interface and the higher the penetration of the optical field into the mirror. This, in turn, leads to a large phase dispersion in the reflectivity.

The optical penetration into the DBR mirrors is important not only in determining the cavity resonance condition, but also in the electrical design of the device. The free-carrier losses at a particular point in the mirror, for example, will be proportional to the product of the free-carrier density and the optical intensity at that point.[8] For longer optical penetration depths, then, one must keep the free-carrier density at a low level further into the mirror. This point will be addressed in more detail in section 4.3.4.

It is important to note that the properties of a DBR mirror are primarily dependent on the mirror period rather than the duty cycle. In other words, the peak reflectivity will occur, to first-order, at the wavelength for which the mirror period (two alternating layers) is one half wavelength. The reduction in the reflectivity due to the deviation of the constituent layers from the ideal quarter wavelength will be a second-order effect. Figure 2-6 illustrates this point for a 15 period GaAs/AlAs DBR with varying duty cycle of the low- and high-index layers. This implies that the center wavelength and phase characteristics of the DBR mirror are determined mostly by the material indices (or reflectivity per interface) and the average growth rate.

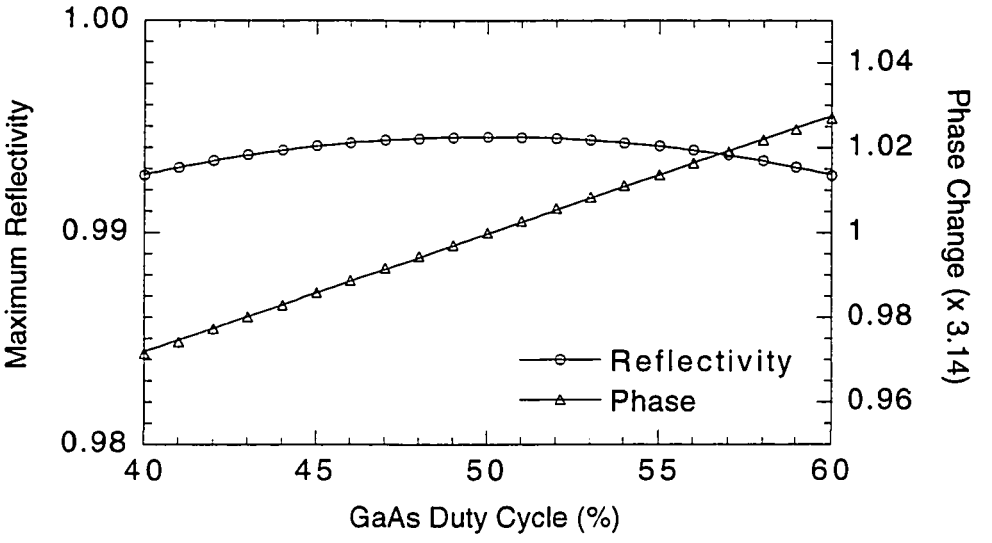

Figure 2-6: Simulated variation the maximum reflectivity and phase shift of a 15 period GaAs/AlAs DBR mirror as a function of the percentage (optical length) of GaAs. The solid lines are parabolic (reflectivity) and linear (phase shift) fits.

2.2.2 VCSEL Fabry-Perot Cavities

Fabry-Perot cavities for VCSELs are created by two DBR mirrors usually separated by one wavelength of material in which the active region is placed. Because of its short gain length, a VCSEL needs very high reflectivity mirrors and low optical losses to operate. Figure 2-7 shows the optical intensity distribution at resonance for such a configuration illustrating the field build-up in the cavity and optical penetration into the mirrors.

Because of the phase dispersion of the DBR mirrors, the resonance condition is no longer simply related to the physical length of the cavity. The resonance condition, that the round-trip phase change be an integer times 2π, must be satisfied by including the phase properties of the mirrors as well. In addition, any property, such as the longitudinal mode spacing, which depends on the change in phase as function of wavelength must then depend on an effective cavity length, which includes the optical

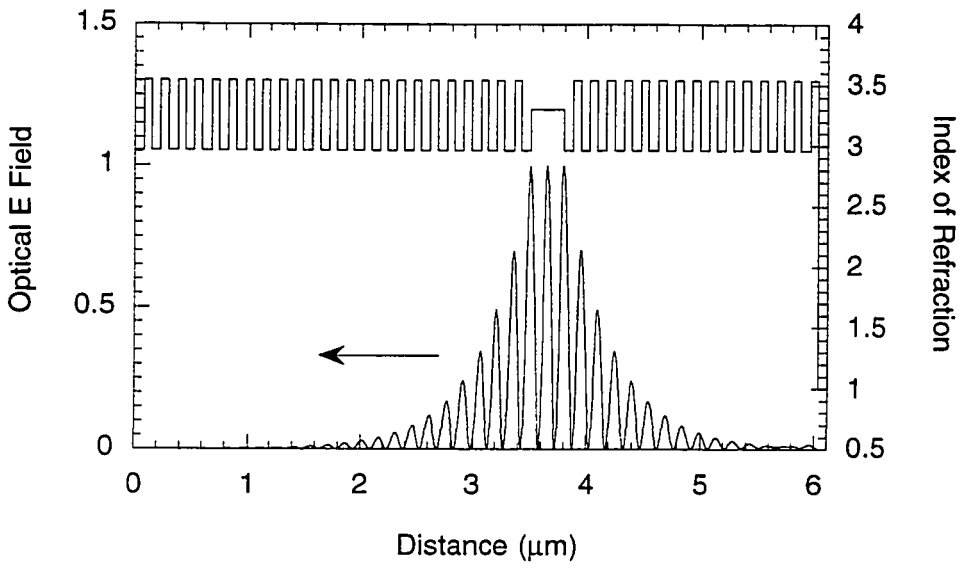

Figure 2-7: Distribution of optical electric field squared at resonance and refractive index profile for a Fabry-Perot cavity consisting of two DBR mirrors separated by one wavelength of material.

penetration into the mirrors, rather than just the physical cavity length. For the example of a 1 wavelength cavity with very high reflectivity GaAs/AlAs DBR mirrors centered at 1 micron, the effective cavity length is 3.7 wavelengths. This would translate into a cavity mode spacing of approximately 134 nm (as opposed to 500 nm neglecting the effects of the mirrors) if the high reflectivity bands of the mirrors were large enough to accommodate it. In general, even including the optical penetration into the mirrors, at most one longitudinal cavity mode can be supported in these structures.

From the reflectivity spectrum of the Fabry-Perot cavity, Figure 2-8, and the target design, all the pertinent information about the structure can be determined. The center wavelength of the DBR mirrors can be determined by the nodes on either side of the high reflectivity region. Along with the material indices, this can be used to determine the phase contribution from the mirrors. Finally, the resonance wavelength in combination with the mirror characteristics can be used to determine the physical length of the cavity.

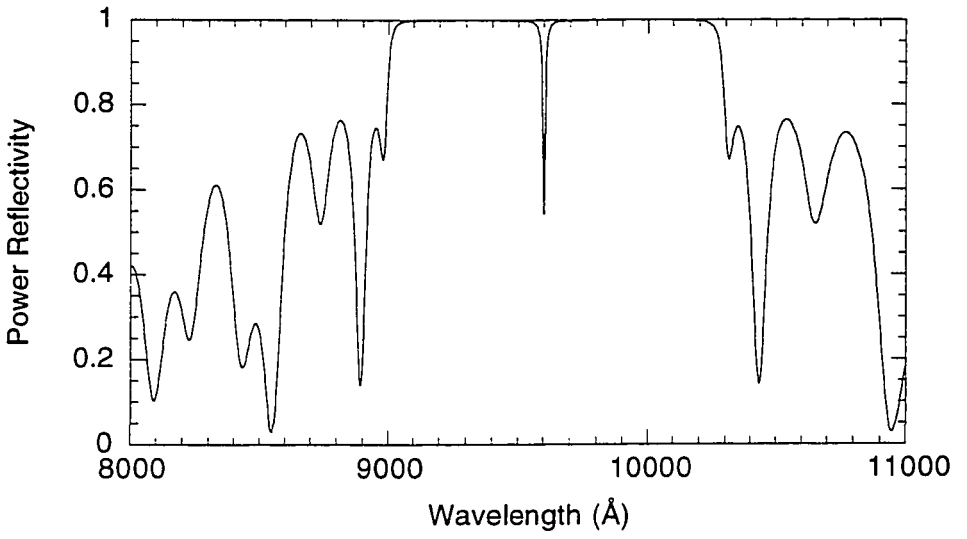

Figure 2-8: Simulated reflectivity spectrum of a DBR Fabry-Perot cavity.

2.2.3 VCSEL efficiency

Since both edge-emitting and vertical-cavity surface-emitting lasers use similar active region designs, they can be expected to have similar internal quantum efficiency.[9] Because of the design complications associated with current injection in the vertical-cavity geometry, however, VCSELs have lagged behind edge-emitters in differential efficiency and especially wall-plug efficiency. A closer look at these factors with assumptions applicable to VCSELs will show which areas need to be addressed in order improve the efficiency.

Vertical -cavity surface-emitting lasers generally have a very short gain medium length which translates into small round-trip gain, loss, and output coupling in operational devices. These quantities can be described with the use of Siegman's delta-notation,[10]

$$
\begin{aligned}
e^{g2L} &= e^{\delta_m} \approx 1+\delta_m \\
e^{-\alpha 2L} &= e^{-\delta_0} \approx 1-\delta_0 \\
R_{1,2} &\equiv e^{-\delta_{1,2}} \approx 1-\delta_{1,2}.
\end{aligned}
\tag{2-14}
$$

Any optical loss in the distributed mirrors is included in the round-trip cavity loss term, δ_0. Typically one mirror will have a much larger output coupling than the other so that the energy is extracted from only one side of the cavity. For $\delta_e = \delta_1 \gg \delta_2$, equation (2-7) can then be written as,

$$\eta_d = \eta_i \left(\frac{\delta_e}{\delta_0 + \delta_e} \right). \tag{2-15}$$

Although, the differential efficiency can be improved by increasing the output coupling, this will also increase the threshold gain and therefore the threshold current. The effect this has on the output power is more complex. As the output coupling is increased from zero, the output power will also increase from zero. At some point a maximum is reached and the output power will decrease with increasing output coupling until the output coupling plus round-trip loss equals the round-trip gain and lasing ceases.

For the case of low output coupling necessitated by the low round-trip gain of VCSELs, the optimum output coupling for a given material gain, determined by the excitation current, will be[11]

$$\delta_{e,opt} = (\sqrt{\delta_{m0}/\delta_0} - 1)\delta_0, \tag{2-16}$$

where δ_{m0} is the unsaturated material gain. Decreasing the optical losses will thus improve the differential efficiency not only directly, through equation (2-15), but also indirectly, by allowing the optimum output coupling to increase.

Another difference between edge-emitters and VCSELs is evident from equation (2-16). A long cavity length creates closely spaced cavity resonances, so there will always be one mode, and perhaps many, near the peak of the gain spectrum. In edge-emitting lasers, therefore, the value of δ_{m0} in equation (2-16) will always be close to the peak material gain for a given injection current. This is not the case for VCSELs, where the gain at a wavelength that satisfies the cavity resonance condition, might be significantly lower than the peak gain in the material. To optimize the differential

efficiency, it is important to reduce the optical losses and increase the output coupling at least to the point which maximizes the output power. Accurate growth of the device is also needed to ensure that the laser operates at a wavelength such that it takes advantage of the peak gain available at a given pumping level.

Insight into increasing the wallplug efficiency of a VCSEL can be obtained by looking first at the V-I and L-I curves of a laser with no electrical losses, Figure 2-9. For this case the wallplug efficiency is easily determined to be,

$$\eta_{wp} = \frac{P_{out}}{P_{in}} = \frac{\eta_s (I - I_{th})}{IV} = \eta_d \frac{I - I_{th}}{I}, \tag{2-17}$$

where the voltage drop is related to the photon energy by $qV = h\nu$. At high current injection, where the power lost to spontaneous emission that does not couple into the lasing mode is small compared with the output power, the wallplug efficiency is limited to the value of the differential quantum efficiency.

If electrical loss is included, the voltage drop at a given operating point will be increased to $V + \Delta V$, which will lower the wallplug efficiency to,

$$\eta_{wp} = \eta_d \left(\frac{I - I_{th}}{I} \right) \left(\frac{V}{V + \Delta V} \right). \tag{2-18}$$

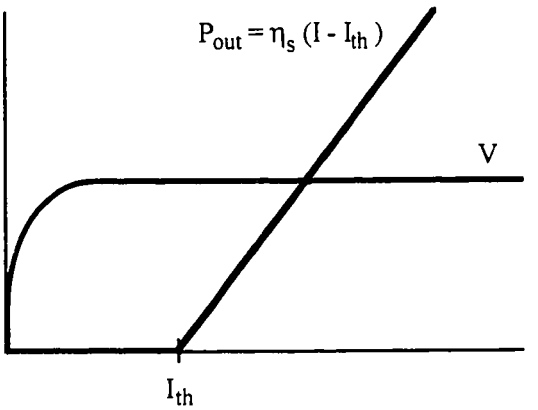

Figure 2-9: Idealized L-I and V-I curves for a semiconductor laser.

To optimize the wallplug efficiency, it is necessary to minimize the optical losses, optimize the output coupling for an operating point significantly above threshold, ensure that the cavity mode selects a wavelength near the peak in the gain spectrum at this operating point, and minimize the electrical losses. The second point can be accomplished in a straight forward manner from equation (2-16) with estimates of the material gain and loss. Chapter 3 of this thesis will address the third point and chapters 4 and 5 will discuss reducing the electrical losses without increasing the optical losses.

2.3 Molecular Beam Epitaxy

Molecular Beam Epitaxy (MBE) is a technique used for the ordered deposition of single crystal thin films on a single crystal substrate. "Molecular beam" refers to the method of transporting the source materials to the substrate, as will be described later, and epitaxy refers to the ordered deposition. Because the material is deposited on the substrate in such a way that it extends the substrate's crystal lattice the deposition is often referred to as crystal growth.

This work is concerned with the growth of $Al_xGa_{1-x}As$ ($0 \leq x \leq 1$) and $In_yGa_{1-y}As$ ($0 \leq y \leq 0.2$) materials on GaAs substrates. To perform the deposition, the elemental source materials are heated in effusion furnace to evaporation. Because the growth chamber is kept in ultra-high vacuum (UHV) conditions, few scattering collisions occur and the evaporated flux of material travels toward the substrate in a line-of-sight "molecular beam" unless blocked by a mechanical shutter, Figure 2-10. The substrate is heated to give the adsorbed material on the surface enough thermal energy to find its proper lattice site for incorporation into the crystal. The walls of the chamber are kept at liquid nitrogen temperatures to adsorb any material that does not hit the substrate so that it cannot contaminate subsequently grown layers.

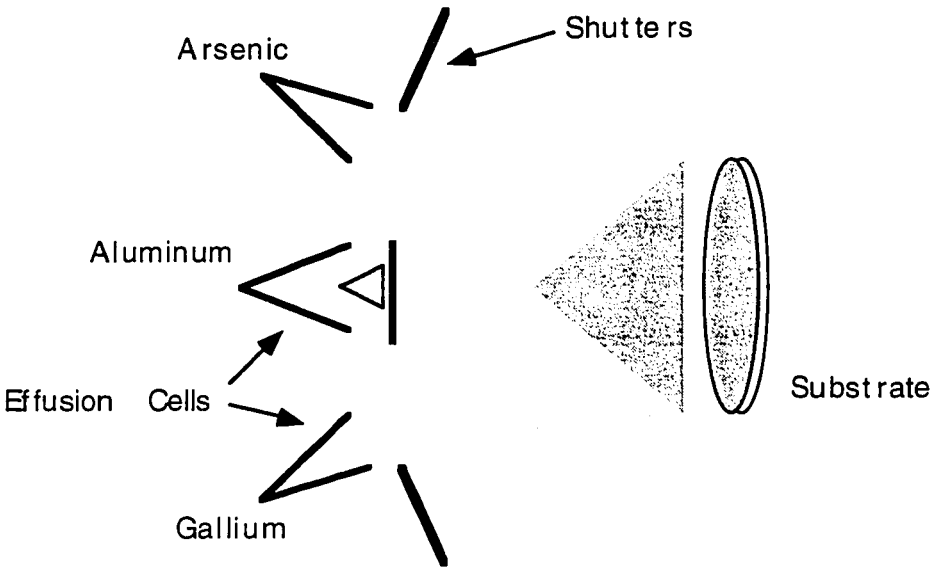

Figure 2-10: Schematic illustrating the MBE growth of GaAs on the substrate.

Because the molecular beams are incident on the substrate at an angle, there will be a large inherent non-uniformity in the deposition rate across the substrate due to the $1/r^2$ dependence of the flux density. When projected on the plane of the substrate, the dominant effect is a linear gradient across the wafer, highest at the point closest to the source and lowest at the point farthest away. This gradient can cause growth rate variations of over 65% (of the thickness at the wafer's center) across the central two inches of a three inch wafer. [12] We have measured non-uniformity of 24% across the central three centimeters of a wafer in our MBE machine at Stanford.[13]

In order to increase uniformity, the substrate is rotated during growth, averaging out linear growth rate variations. As shown in Figure 2-11, the uniformity is much improved. A 0.7% variation is measured across the central 1.5 inches and only a 1.25% variation is measured across the whole 2 inch wafer. By the parabolic fit of the radial thickness, it is clear that the linear growth rate variation has been averaged out entirely.

For normal growth of III-IV materials, the column V material, in this case arsenic, is present in excess and the growth rate is controlled by the arrival rate of the column III

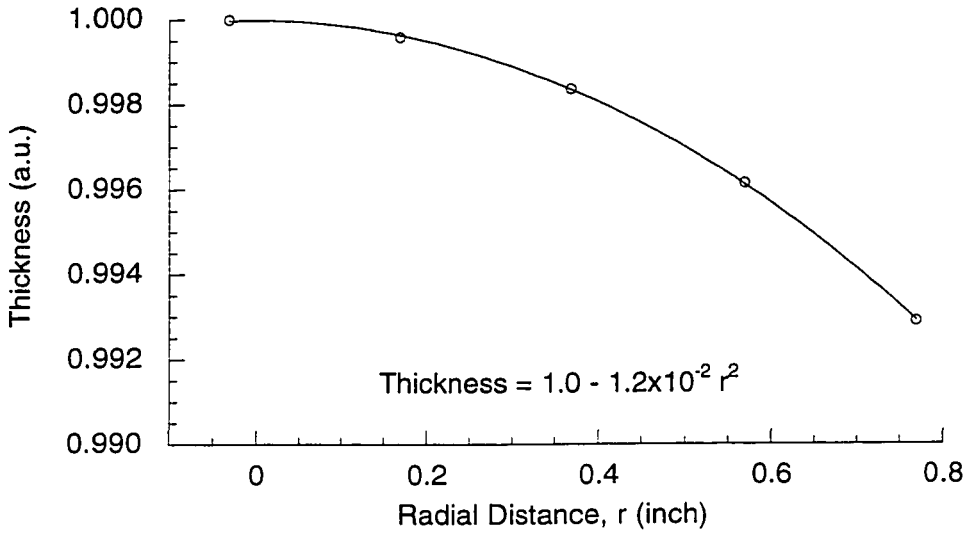

Figure 2-11: Proportional thickness as a function of the distance from the wafer center indicating the radial growth rate variation for MBE growth on a rotating substrate.

materials. This rate, in turn, is controlled by the temperature of the effusion cell. A thermocouple pressed against the back side of the crucible which holds the source material in the effusion cell is used in a feedback loop to maintain a constant temperature, and thus a constant growth rate.

Modern effusion cell controllers can normally maintain the thermocouple temperature to within ±0.1° C for periods of many hours, enabling the material flux from the effusion cell to remain very stable.[14] Problems can be introduced, however, when the temperature setpoint is altered. Although the material flux does follow an exponential dependence on the cell temperature as expected, the accuracy of determining the new flux based on the temperature change however is limited to a few percent in practice.[15] This is probably due to small shifts in the thermocouple contact with the crucible as the temperature is adjusted.

As a result, once the cell has stabilized at the growth temperature, the material flux or growth rate is measured directly and the effusion cells are maintained at a constant

temperature for the entire growth. When extreme growth rate accuracy is needed, one conventionally resorts to Reflection High-Energy Electron Diffraction (RHEED) to measure the growth rate on a specially prepared sample.[16] An accuracy of 1% is typically obtained this way. At Stanford we have found that this degree of accuracy is also obtainable with a much simpler, automated ionization gauge measurement of the material flux if the ratio between growth rate and flux for each of the sources has previously been determined.[17]

2.4 Problems for Achieving High-Efficiency VCSELs

Major difficulties in achieving high-efficiency operation of vertical-cavity surface-emitting lasers have involved both the growth and design of these structures. Because the material gain bandwidth is typically about 1% of the optical frequency[18] and the operating frequency, as has been discussed, is proportional to the layer thicknesses, a growth accuracy of about 1% is required just to insure a device will operate at all.

The growth rate determination accuracy of 1% mentioned in the preceding section is thus barely sufficient for producing operational devices. As pointed out by Young, et al.,[19] and evident from equation (2-16), the operating characteristics of VCSELs are very dependent on the precise overlap of the cavity mode with the gain spectrum. To repeatably produce high-efficiency lasers, this overlap must be optimized and precisely controlled. Clearly, some method to improve the accuracy of VCSEL growth is needed to accomplish these ends.

Additional challenges are faced in the design of efficient VCSELs. Since the optical wave and electrical current propagate in the same direction, normal to the surface, the design is often seen as a compromise between optimizing the electrical or optical characteristics of the device. In particular, the GaAs/AlAs heterojunctions which give rise to high reflectivity DBR mirrors can prove very resistive to current flow, especially on the p-side of the device.

Abrupt heterojunctions and low doping levels are ideal for reducing the optical losses of the device, but cause unacceptable electrical losses. In addition to lost power, the resulting heating can increase non-radiative carrier recombination which raises the threshold current and increase free-carrier absorption which additionally decreases the differential quantum efficiency. Very gradual changes between materials and higher doping, on the other hand, are optimal for electrical conduction, but cause increased optical penetration into the mirrors and higher free-carrier levels- both of which increase the optical losses.

The following chapters will detail improvements to the growth, design, and processing of VCSELs to remedy these problems. First, an in-situ method to correct the growth of these devices is presented which enables accurate positioning of the operating wavelength with respect to the gain spectrum. Second, an improvement to the design of the p-type DBR mirrors is presented which offers the potential of obtaining high reflectivity per mirror pair, very low resistance, and low free carrier levels simultaneously. Finally, an alternative fabrication process is presented to realize a low resistance intracavty n-type contact to a VCSEL structure. Taken together, these improvements should enable the fabrication of high-efficiency vertical-cavity surface emitting lasers.

3. In-Situ Corrections for MBE Growth

This chapter will discuss an in-situ method for correcting the growth of vertical cavity optical devices. The first section deals with the calculation of the optical properties, reflectivity, transmission, absorption, reflected phase and optical electric field distribution, of a collection of thin films on a substrate. As well as being useful as a design tool, these calculations are used to model growth errors to determine the magnitude of corrections to be applied. The second section deals with the theory and practice of using in-situ reflectivity measurements to correct the growth of vertical-cavity optical devices. Results will be presented of the application of this technique to correcting the growth of simple VCSELs and other more demanding device designs.

3.1 Thin Film Calculations

A layer is termed a thin film when interference effects are important in determining its reflection and transmission properties. This implies that the optical path difference between reflections from the film's interfaces is smaller than the coherence length of the illuminating light. If, for example, one is observing the reflected or transmitted light with a spectrometer with a resolution of 1 nanometer, a layer with index of refraction equal to 3.5 can be considered thin if it is less that about 150 microns thick. As a result, a GaAs substrate, 350-500 microns, would be considered thick while MBE grown multilayer structures, generally less than 1-10 microns total thickness, would be considered thin.

3.1.1 Theory

First, a simple interface will be analyzed and the results generalized with the concept of the optical admittance. From the optical admittance of the incident medium and the substrate, the reflection and transmission of the interface can be determined. A thin film on a substrate can then be analyzed in a straight forward manner by how it

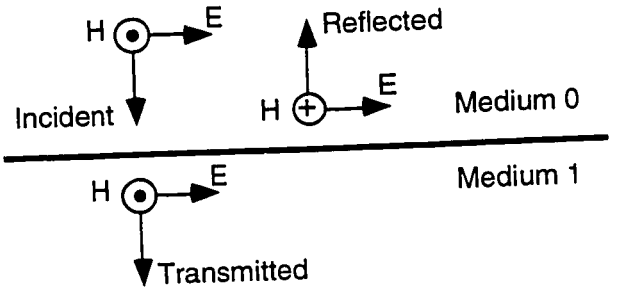

Figure 3-1: Conventions for positive direction of vectors in boundary analysis.

changes the optical admittance of the substrate as seen by the incident wave. This process can be repeated for additional layers, so the reflection and transmission properties of an assembly of thin film layers can be determined. This derivation follows the admittance matrix approach of MacLeod. [20]

For normal incidence, the convention to be used for the orientations of the E- and H-fields for the incident, reflected, and transmitted waves are shown in Figure 3-1. The tangential components of the two fields are continuous across the interface, leading to

$$\mathcal{E}_{inc} + \mathcal{E}_{refl} = \mathcal{E}_{trans}, \text{ and} \tag{3-1}$$

$$\mathcal{H}_{inc} - \mathcal{H}_{refl} = \mathcal{H}_{trans} \Rightarrow y_0\mathcal{E}_{inc} - y_0\mathcal{E}_{refl} = y_1\mathcal{E}_{trans}, \tag{3-2}$$

where the subscripts inc, refl, and trans refer to the incident, reflected and transmitted waves, the subscripts 0 and 1 refer to the two media, and the optical admittance, y_n, is the ratio of the E- and H-fields in a given media. The optical admittance is related to the index of refraction by

$$y = n\sqrt{\varepsilon_0/\mu_0}\,. \tag{3-3}$$

The amplitude transmission and reflection coefficients can be determined from equations (3-1) and (3-2) to be,

$$\tau = \frac{\mathcal{E}_{trans}}{\mathcal{E}_{inc}} = \frac{2y_0}{y_0 + y_1} = \frac{2n_0}{n_0 + n_1}, \text{ and} \tag{3-4}$$

$$\rho = \frac{\mathcal{E}_{refl}}{\mathcal{E}_{inc}} = \frac{y_0 - y_1}{y_0 + y_1} = \frac{n_0 - n_1}{n_0 + n_1}. \tag{3-5}$$

The power reflectivity and transmission can then be derived by the ratio of the reflected and transmitted intensity to the incident intensity,

$$R = \frac{I_{refl}}{I_{inc}} = \rho^2$$

(3-6)

$$T = \frac{I_{trans}}{I_{inc}} = \frac{y_1}{y_0}\tau^2.$$

To treat oblique incidence, one can again match the tangential components of the E and H fields across the boundary. If, however, the transmission coefficient is still defined in terms of the original fields, $\mathcal{E}_{trans}$ and $\mathcal{E}_{inc}$, the expected relationship that R+T=1 will no longer hold. This occurs because the transmitted wave has a different inclination with respect to the boundary than the incident and reflected waves as determined by Snell's law,

(3-7) $$n_0 \sin\theta_{inc} = n_0 \sin\theta_{refl} = n_1 \sin\theta_{trans}.$$

Defining the transmission and reflection components as ratios of the tangential components of the waves will correct the apparent contradiction by considering energy flow in the direction perpendicular to the boundary. In this case, the form of equations (3-4) and (3-5) can be retained for oblique incidence if y for each medium is replaced by the modified optical admittance, η, which is the ratio of the tangential components of $\mathcal{H}$ and $\mathcal{E}$:

(3-8) $$\eta = \frac{\mathcal{H}_{tangential}}{\mathcal{E}_{tangential}} = \frac{H}{E},$$

where the non-script E and H refer to the tangential components of the fields. Two cases must be considered for oblique incidence: transverse electric (TE), where the electric-field vector is parallel to the boundary, and transverse magnetic (TM), where the magnetic-field vector is parallel to the boundary.[21] With reference to Figure 3-2, η for each case is

(3-9) $$\eta_{TE} = y\cos\theta \quad \eta_{TM} = \frac{y}{\cos\theta},$$

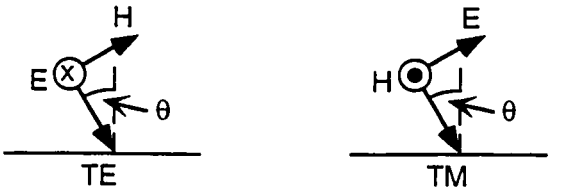

Figure 3-2: Orientation of TE and TM polarizations.

where θ is the angle of the incident wave with respect to the interface normal, and the TE and TM subscripts refer to transverse electric and transverse magnetic cases.

Absorbing material can be treated by replacing n in equation (3-3) by the complex index of refraction, N,

(3-10) $$N = n - ik.$$

While all the amplitude relationships, τ and ρ, are still valid, because of the coupling between the forward and backward waves by the material absorption, it is no longer valid to relate these fields to forward and backward going intensities. As a result, the power reflectivity will only have meaning if the incident medium is transparent.

To extend the one boundary analysis to a thin film, one must account for the multiple reflections that can occur between the interfaces of the layer, Figure 3-3. These multiple reflections are summed to a resultant forward going and backward going wave in each medium, except that there is no backward wave in the substrate. Again, looking only

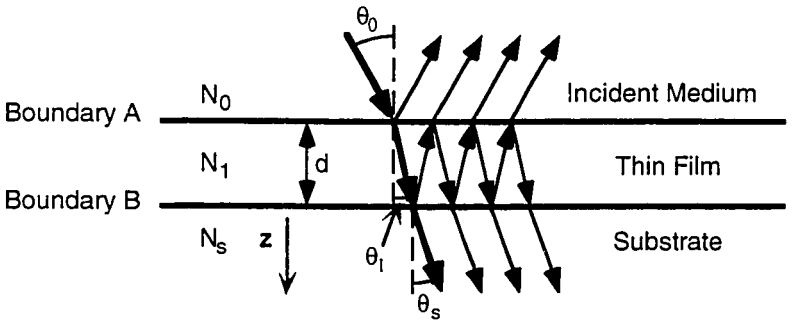

Figure 3-3: Analysis of a thin film illustrating multiple reflections from the interfaces.

at the tangential components of the waves, the forward and backward waves in the thin film can be summed at the substrate interface to yield,

(3-11) $$E_B = E_{1B}^{+} + E_{1B}^{-} \text{ and}$$

(3-12) $$H_B = H_{1B}^{+} - H_{1B}^{-} = \eta_1 E_{1B}^{+} - \eta_1 E_{1B}^{-},$$

where the + and - superscripts refer to the wave's direction and the subscripts indicate that we are interested in the fields in medium 1 at interface B. The subscript for the medium is not needed for the total fields, because these are continuous across the boundary. The forward and backward going waves can then be represented in terms of the fields at the interface by rearranging terms,

(3-13) $$E_{1B}^{+} = \frac{1}{2}(E_B + H_B/\eta_1) \quad E_{1B}^{-} = \frac{1}{2}(E_B - H_B/\eta_1)$$

(3-14) $$H_{1B}^{+} = \frac{1}{2}(H_B + \eta_1 E_B) \quad H_{1B}^{-} = \frac{1}{2}(H_B - \eta_1 E_B).$$

These waves will be related to their counterparts at interface A by a phase factor for propagation through the layer at an angle θ_1 (see Figure 3-3) with respect to the interface normal,

(3-15) $$E_{1A}^{+} = E_{1B}^{+}\exp(-i\delta) \quad E_{1A}^{-} = E_{1B}^{-}\exp(i\delta)$$

(3-16) $$H_{1A}^{+} = H_{1B}^{+}\exp(-i\delta) \quad H_{1A}^{-} = H_{1B}^{-}\exp(i\delta)$$

(3-17) $$\text{where } \delta = 2\pi N_1 d\cos\theta_1/\lambda.$$

The total tangential fields at interface A can then be written in terms of those at interface B by combining equations (3-13) through (3-16),

(3-18) $$E_A = (\cos\delta)E_B - \frac{i\sin\delta}{\eta_1}H_B$$

(3-19) $$H_A = (-i\eta_1\sin\delta)E_B + (\cos\delta)H_B.$$

This can be written in matrix form as

(3-20) $$\begin{bmatrix} E_A \\ H_A \end{bmatrix} = \begin{bmatrix} B \\ C \end{bmatrix} E_B = \begin{bmatrix} \cos\delta & -\frac{i\sin\delta}{\eta_1} \\ -i\eta_1\sin\delta & \cos\delta \end{bmatrix} \begin{bmatrix} 1 \\ \eta_2 \end{bmatrix} E_B.$$

The input optical admittance, Y, can then be defined by analogy with equation (3-8),

$$Y = \frac{H_A}{E_A}. \tag{3-21}$$

The thin film can be seen as transforming the optical admittance of the substrate, η_2, into the new admittance Y by,

$$\begin{bmatrix} 1 \\ Y \end{bmatrix} = \begin{bmatrix} \cos\delta & -\frac{i\sin\delta}{\eta_1} \\ -i\eta_1\sin\delta & \cos\delta \end{bmatrix} \begin{bmatrix} 1 \\ \eta_2 \end{bmatrix}. \tag{3-22}$$

The 2x2 matrix is the characteristic matrix of the thin film and is dependent only on the physical thickness of the layer, its index, and the angle of propagation though the layer. By an analysis similar to that leading to equations (3-4) through (3-6), the amplitude and power reflectivity of the thin film can be derived:

$$\rho = \frac{\eta_0 - Y}{\eta_0 + Y}$$
$$R = \left(\frac{\eta_0 - Y}{\eta_0 + Y}\right)\left(\frac{\eta_0 - Y}{\eta_0 + Y}\right)^*. \tag{3-23}$$

The analogous transmission properties, however, would be only into, but not through the thin film. From equation (3-20), the incident intensity can be easily related to the transmitted intensity and the transmission and absorption properties of the film can be obtained as well.

$$\rho = \frac{\eta_0 B - C}{\eta_0 B + C}$$
$$R = \left(\frac{\eta_0 B - C}{\eta_0 B + C}\right)\left(\frac{\eta_0 B - C}{\eta_0 B + C}\right)^*$$
$$T = \frac{4\eta_0\,\mathrm{Re}(\eta_2)}{(\eta_0 B + C)(\eta_0 B + C)^*} \tag{3-24}$$
$$A = \frac{4\eta_0\,\mathrm{Re}(BC^* - \eta_2)}{(\eta_0 B + C)(\eta_0 B + C)^*},$$

An additional layer can be handled in a straight forward manner by left multiplying equation (3-20) by the characteristic matrix of the new layer. Repeating this procedure, one finds that the characteristic matrix of an assembly of x thin film layers is just the product of the characteristic matrices of the individual layers in the correct order.

$$\begin{bmatrix} B \\ C \end{bmatrix} E_s = \left(\prod_{r=1}^{x} \begin{bmatrix} \cos\delta_r & -\frac{i\sin\delta_r}{\eta_r} \\ -i\eta_r \sin\delta_r & \cos\delta_r \end{bmatrix} \right) \begin{bmatrix} 1 \\ \eta_s \end{bmatrix} E_s . \tag{3-25}$$

The optical properties of the assembly can be then be determined by applying the formulas in (3-24) to the resultant 1x2 matrix. It is important to note, that the characteristic matrix must be recomputed for each wavelength and angle to be examined, so a spectrum from an arbitrary assembly of even a moderate number of layers requires the use of a computer.

3.1.2 Closed Form Solutions for Distributed Bragg Reflectors

Analytic solutions and approximations can be found for the special case of an assembly of alternating high and low index quarter wave layers at and near the design wavelength. The characteristic matrix for a quarter wave layer has zeros in its diagonal elements,

$$M_{\lambda/4} = \begin{bmatrix} 0 & -i/\eta \\ -i\eta & 0 \end{bmatrix}. \tag{3-26}$$

As a result, the characteristic matrix for a pair of high and low index quarter wave layers is diagonal,

$$M_{Pair} = \begin{bmatrix} 0 & -i/\eta_H \\ -i\eta_H & 0 \end{bmatrix} \begin{bmatrix} 0 & -i/\eta_L \\ -i\eta_L & 0 \end{bmatrix} = \begin{bmatrix} -\eta_L/\eta_H & 0 \\ 0 & -\eta_H/\eta_L \end{bmatrix}, \tag{3-27}$$

where the low index layer is assumed closest to the substrate. Since the matrix is diagonal, raising it to a power to account for multiple pairs is equivalent to raising the diagonal elements to the same power,

(3-28) $$\left(M_{pair}\right)^p = \begin{bmatrix} \left(-\eta_L/\eta_H\right)^p & 0 \\ 0 & \left(-\eta_H/\eta_L\right)^p \end{bmatrix}.$$

The power reflectivity can then be determined from equations (3-24) and (3-25). The ratios of admittance can be replaced by ratios of complex refractive index. Assuming the layers of the assembly and substrate are non-absorbing, the reflectivity is,

(3-29) $$R = \left[\frac{n_0\left(-n_L/n_H\right)^p - n_S\left(-n_H/n_L\right)^p}{n_0\left(-n_L/n_H\right)^p + n_S\left(-n_H/n_L\right)^p}\right]^2 \approx 1 - 4\left(n_0/n_S\right)\left(n_L/n_H\right)^{2p},$$

where n_0 and n_S are the incident medium and substrate refractive indices.

The error in the above approximation is less than $\frac{1}{2}(1-R)^2$.

The effects of slight thickness or wavelength deviations from the ideal can be analyzed by altering the phase thickness of the layers slightly,

(3-30) $$\delta = \pi/2 + \Delta.$$

Since we are interested in the characteristics of the mirrors as seen from the cavity, we will start with the outside of the mirror and work toward the cavity. For the top mirror, the characteristic matrix of a mirror pair is,

(3-31) $$\begin{bmatrix} -\Delta_L & -i/n_L \\ -in_L & -\Delta_L \end{bmatrix}\begin{bmatrix} -\Delta_H & -i/n_H \\ -in_H & -\Delta_H \end{bmatrix} = \begin{bmatrix} -n_H/n_L & i\left(\Delta_L/n_H + \Delta_H/n_L\right) \\ i\left(\Delta_H n_L + \Delta_L n_H\right) & -n_L/n_H \end{bmatrix},$$

where the approximations $\sin(\pi/2+\Delta) \approx 1$ and $\cos(\pi/2+\Delta) \approx -\Delta$ have been made and the second order terms neglected in the multiplication as well. For a p pair mirror, the characteristic matrix, again ignoring second and higher order terms in Δ, will have the form,

(3-32) $$\begin{bmatrix} -n_H/n_L & i\left(\Delta_L/n_H + \Delta_H/n_L\right) \\ i\left(\Delta_H n_L + \Delta_L n_H\right) & -n_L/n_H \end{bmatrix}^p = \begin{bmatrix} M_{11} & -iM_{12} \\ -iM_{21} & M_{22} \end{bmatrix}.$$

After suitable manipulation, one finds,

$$M_{11} = (-n_H/n_L)^p = 1/M_{22}$$

(3-33)
$$M_{12} = \frac{(-n_H/n_L)^p n_H n_L (\Delta_L/n_H + \Delta_H/n_L)}{n_H^2 - n_L^2}\left[1 - \left(\frac{n_L}{n_H}\right)^{2p}\right]$$

$$M_{21} = \frac{(-n_H/n_L)^p n_H n_L (n_H\Delta_L + \Delta_H n_L)}{n_H^2 - n_L^2}\left[1 - \left(\frac{n_L}{n_H}\right)^{2p}\right].$$

The term $(n_L/n_H)^{2p}$ will be small compared to 1 for a high reflectivity mirror and so can be ignored here. Inserting these results in equations (3-24) and (3-25) will yield,

(3-34)
$$\rho = \frac{n_C^2 M_{11}^2 - n_S^2 M_{22}^2 + i2n_C(M_{11}M_{21} - n_S^2 M_{22}M_{12})}{(n_C M_{11} + n_S M_{22})^2},$$

where n_S is the substrate index and n_C is the cavity (incident) index. The result for the power reflectivity, $R = \rho\rho^*$, is the same as equation (3-29), indicating that the magnitude of R is unaffected to first-order by a small error in layer thickness.

The reflected phase, however, will be affected by the deviation from quarter wavelength layers. The tangent of the phase angle is determined by the ratio of the imaginary and real parts of ρ. Since the angle is small, one can approximate the tangent by the angle itself or π plus the angle. From the signs of the numerator and denominator, the angle is in the 1st or 4th quadrant yielding,

(3-35)
$$\phi = \frac{2n_H n_L (n_L\Delta_H + n_H\Delta_L)}{n_C(n_H^2 - n_L^2)}.$$

The bottom DBR mirror will have an odd number of layers, with an extra low index layer on the substrate side of the stack compared to the mirror analyzed above. This can be incorporated by right multiplying equation (3-33) by a low index characteristic matrix. One finds that the reflectivity and phase of the bottom DBR mirror are,

(3-36)
$$R \approx 1 - 4\frac{n_L^{\,2}}{n_C n_S}\left(\frac{n_L}{n_H}\right)^{2p}$$
$$\phi = 2\frac{n_H n_L\left(n_L\Delta_H + n_H\Delta_L\right)}{n_C\left(n_H^{\,2} - n_L^{\,2}\right)}.$$

Again, the reflectivity is not effected to first order by the deviation from quarter wave layers. The phase change is the same as in equation (3-35), indicating that it is determined only by the characteristics of the "front" of the mirror.

As mentioned in the DBR background section, this phase change is correlated with the optical penetration into the DBR mirror. The phase thickness of the individual layers is given by equations (3-17) and (3-30), so the error introduced by changing the wavelength is,

(3-37)
$$\frac{d\Delta}{d\lambda} = \frac{d\delta}{d\lambda} = -\frac{\delta}{\lambda} \approx -\frac{\pi}{2\lambda}.$$

Because this is an optical thickness error, it will be the same for both high and low index layers. The effect of this error can be seen from equation (3-35) with $\Delta_H = \Delta_L = \Delta$,

(3-38)
$$\frac{d\phi}{d\Delta} = \frac{2n_H n_L}{n_C\left(n_H - n_L\right)}.$$

The change in reflected phase as a function of wavelength is then

(3-39)
$$\frac{d\phi}{d\lambda} = \left(\frac{d\phi}{d\Delta}\right)\left(\frac{d\Delta}{d\lambda}\right) = \frac{-\pi n_H n_L}{n_C\left(n_H - n_L\right)\lambda},$$

and the optical length associated with this phase change is

(3-40)
$$L_{opt} = -\frac{\lambda^2}{4\pi}\left(\frac{d\phi}{d\lambda}\right) = \frac{\lambda n_H n_L}{4n_C\left(n_H - n_L\right)}.$$

The optical penetration into the DBR mirror can also be estimated directly from the evolution of the electric field squared as additional mirror pairs are added. Nodes and anti-nodes will occur at alternating interfaces. As can be seen from equation (3-27), the magnitude of successive anti-nodes will decay by a factor of $(n_L/n_H)^2$ each mirror pair, or

$\lambda/2$ penetration into the mirror. Approximating this by a continuous decay, the optical distance at which the intensity has decayed by a factor of e is

$$L_{opt} = -\frac{\lambda}{4\ln(n_L/n_H)}. \tag{3-41}$$

By expressing the indices as $n_L = n - \Delta n/2$ and $n_H = n + \Delta n/2$, the natural log can be approximated very accurately by

$$\ln(n_L/n_H) \approx -2\left(\frac{\Delta n}{2n}\right) \tag{3-42}$$

because the second order terms in $\Delta n/2n$ cancel. The ratio of equations (3-40) and (3-41) is then seen to be n/n_C. The slight inequality of the two distances arises from ignoring the effects of the cavity/mirror interface in the simple derivation leading to equation (3-41).

3.1.3 Numerical Simulations

The equations (3-17), (3-24), and (3-25) can readily be programmed to produce numerical results for the reflection, transmission, absorption and phase as a function of wavelength. In theory one should determine the characteristic matrix of the structure for both TE and TM polarizations at each wavelength and angle of incidence of interest. The predicted characteristics of the mirror, would then be a suitable average over polarization and angle. Fortunately, this level of complexity is not necessary to match experimental results.

With reference to equations where the non-script E and H refer to the tangential components of the fields. Two cases must be considered for oblique incidence: transverse electric (TE), where the electric-field vector is parallel to the boundary, and transverse magnetic (TM), where the magnetic-field vector is parallel to the boundary. With reference to Figure 3-2, η for each case is

(3-9) and (3-17), the effects of oblique incident light are to decrease the optical thickness and alter the effective admittance of the thin film layers. The dominant effect will be to

shift the spectral features to shorter wavelengths through the factor of cos(θ). The large index of refraction for the semiconductor layers, however, dictates that the effects will be rather small. an incident angle of 25°-30° external to the semiconductor is necessary to reduce the cosine factor by 1%. Normal incidence is thus assumed for all the simulated data in this work.

The effects of index dispersion were initially included using the equations from Adachi[22] to model the refractive index as a function of wavelength, and AlGaAs composition. Figure 3-4 compares the measured reflectivity of a DBR mirror to that simulated with and without including dispersion. The mirror period in the simulations was adjusted so that the center wavelengths would coincide with that of the measured mirror. For the case neglecting dispersion, theoretical curve (a) in the figure, the index values for GaAs and AlAs at the center wavelength of the mirror are used. As can be seen, the agreement is very good for the simpler case and is not notably improved by including index dispersion, theoretical curve (b). Furthermore, at the GaAs band-edge, the

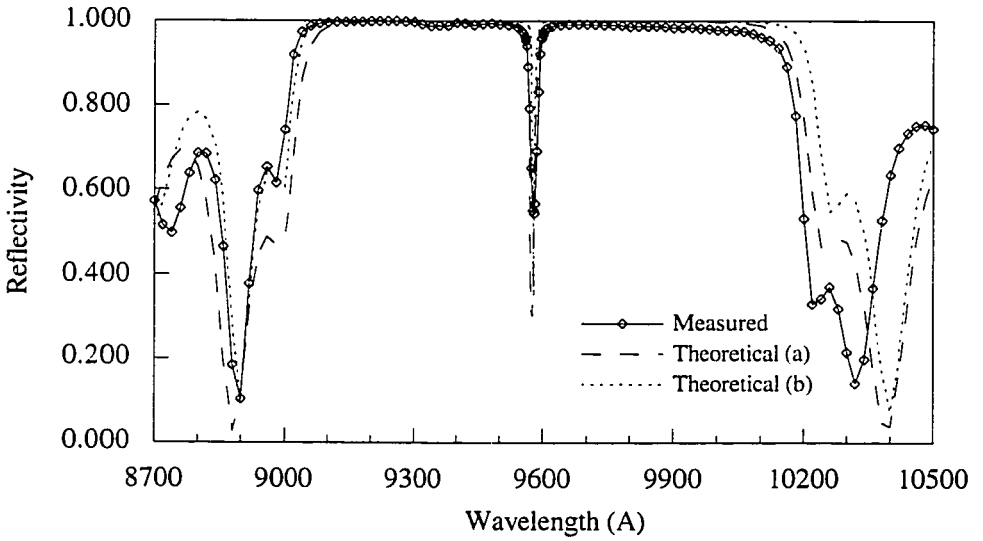

Figure 3-4: Measured and simulated reflectivity spectra for a Fabry-Perot cavity. Theoretical curve (a) neglects index dispersion, while (b) includes it.

index values from Adachi change abruptly, causing kinks which are not observed in the experimental spectra. Possibly the indices from Adachi are for undoped material which might exhibit a sharper index kink at the bandgap energy.[23] This suggests that the dispersion data in Adachi are not very accurate for modeling effects across the transition from non-absorbing to absorbing materials in these structures.

3.2 Corrections to the Growth of Vertical-Cavity Optical Devices

A simple technique was developed for correcting the growth of vertical-cavity optical devices which relies on information from reflectivity scans taken during growth interruptions. During the growth interruption, the wafer is cooled to room temperature and positioned in front of a viewport so the reflectivity can be measured. Although for the sake of measurement simplicity we generally transfer the wafer to the UHV transition tube which connects to the growth chamber of our MBE machine, we have performed these measurements through the pyrometer port in the growth chamber as well, so the wafer can remain in the growth position for the measurement if that is desired.

The measurement apparatus is shown in Figure 3-5. White-light, coupled into a fiber bundle, is imaged on the sample through the imaging lenses. The back reflection is collected by the fiber bundle and, with the beamsplitter, sent into the spectrometer for spectral analysis. The chopper and lock-in are included to reduce the signal from back-

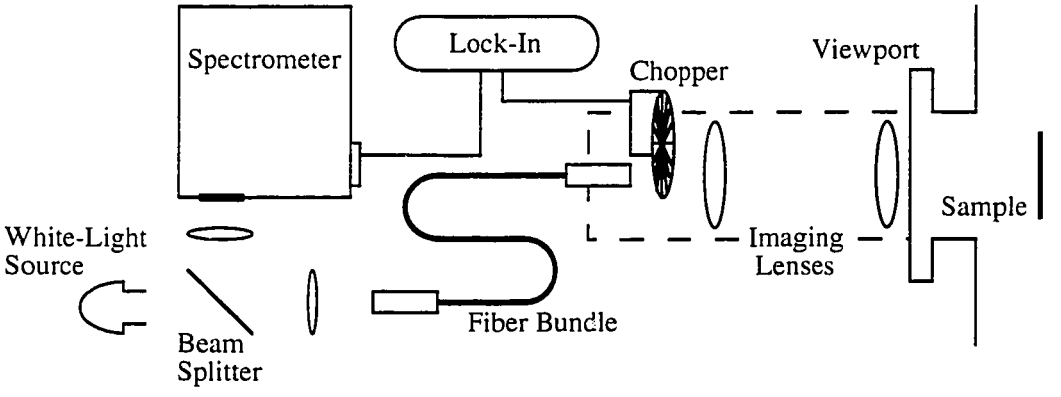

Figure 3-5: Schematic of reflectivity measurement apparatus.

reflections, especially off the end-faces of the fiber bundle. A silicon detector is mounted on the spectrometer to detect the light. This causes an apparent decrease in the reflected signal at longer wavelengths (> 950 nm) because of the lower detector responsivity. Generally, this is not a problem either because the decrease occurs beyond the spectral region of interest, or the decay rate is small compared to the rate of change of the spectral features being measured. If this is a problem, one can use the measurement of a spectrally flat reflector (e.g. a bare GaAs wafer in this spectral region) to normalize the system response or switch to an InGaAs detector, which has a flatter response from about 1000 nm out to longer than 1300 nm.

A growth interruption is made after the bottom mirror and cavity are grown to measure the cavity resonance wavelength before the top mirror is grown. Care must be taken so the growth interruption occurs at a point in the structure where the semi-conductor / vacuum interface will provide the correct reflected phase to satisfy the cavity resonance condition. If, for example, the first layer of the top DBR mirror will be a high-index layer (next to a low-index cavity), a quarter wavelength of the top mirror must be grown to observe the cavity resonance. In situations where the growth rates of the layers are not well known or the high-reflectivity region of the mirror will be very narrow, one can perform a prior measurement on the initial five mirror periods of the bottom DBR mirror to correct the average growth rate error and center the mirror reflectivity at the desired wavelength.

3.2.1 Growth Correction Theory

Although small, random variations in the layer thicknesses of a quarter-wave mirror have a very small effect on its reflectivity,[24] a systematic change in the mirror period will cause an almost proportional shift in the center wavelength.[25] By measuring the reflectivity spectrum of the mirror after only a few periods have been grown, one can determine the relative error in the center wavelength. If all subsequent layer thicknesses are corrected proportionally, the center wavelength of the corrected mirror will be very

near the desired wavelength. In practice, there will always be a residual error due to light reflected from the initial, uncorrected mirror periods and phase errors from the "half period" interfaces if the duty-cycle of the mirror deviates from the ideal 50%.

It is difficult to derive closed-form approximations to analyze the effects of the mirror correction on device performance, since, as shown in section 3.1.2, the mirror reflectivity is independent to first order on small deviations in layer thicknesses. One can, however, easily quantify both the amount of correction and the reduction in reflectivity expected through the use of numerical simulations.

Several mirrors were simulated to analyze the effects of the correction. It is assumed that the growth rates for the mirror layers are constant, but inaccurately known. As a result, all layers of the same material have the same thickness error. The errors for GaAs and AlAs layers were varied independently from -5% to 5% in 2.5% increments to cover a rather extreme range of expected errors. Five periods of each mirror were analyzed numerically to determine the wavelength of maximum reflectivity, λ_{Rmax}. Ten more mirror periods were added with the thicknesses adjusted by the factor $\lambda_{target}/\lambda_{Rmax}$ from the layers of the first 5 periods. For the growth of a real device, the adjustment would be accomplished by changing the amount of time the shutters were open for each layer by this factor. The properties of the resulting 15 period mirrors were simulated to determine the peak reflectivity and residual fractional deviation from the target wavelength.

The results of the 25 simulations are shown in Figure 3-6. Each cluster of points consists of mirrors with the same error in mirror period, but with varying duty cycle. As expected, the center wavelength and magnitude of the reflectivity are mainly dependent on the mirror period and are relatively insensitive to variations in the duty-cycle. In each case approximately 75% of the initial wavelength deviation is corrected with only a slight, second-order, effect on the magnitude of the peak reflectivity.

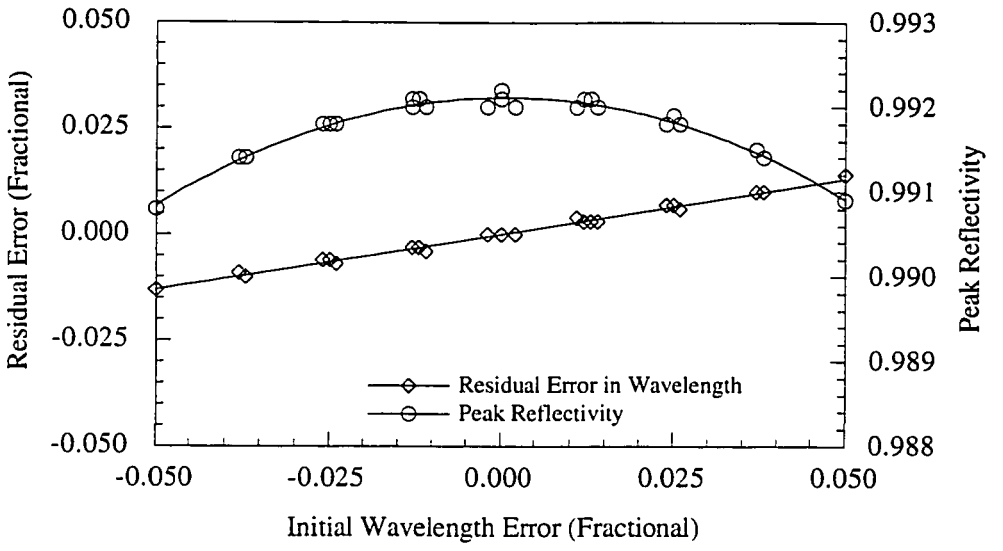

Figure 3-6: Plot of residual wavelength error and peak reflectivity of a corrected 15 period mirror as a function of the error in the initial 5 periods.

A 5% deviation of the center wavelength of the mirror from the target wavelength would have a disastrous effect on the device performance if left uncorrected because this shift is almost 1/2 the width of the high-reflectivity region. If such errors were expected, it would be necessary to perform the above correction to center the DBR mirrors to ensure that the device could operate (i.e. the mirror reflectivity was high enough) at the desired wavelength. Currently, however, our beam-flux calibration accuracy is such that the error is generally on the order of 1% or less. As a result, this correction is generally skipped without compromising the device performance.

After the bottom mirror and cavity are completed a growth interruption and reflectivity measurement are performed. From the measured resonance and the center wavelength of the mirror (determined by the extent of the high-reflectivity region) one can calculate the phase adjustment that must be made to move the resonance to the desired wavelength. This adjustment can be supplied by lengthening the cavity if the uncorrected resonance is at too short a wavelength or shortening the first mirror period if it is at too long a wavelength.

At this point it is illuminating to examine the consequences of the optical penetration into the DBR mirror for determining the cavity resonance wavelength. If the resonance condition for the physical cavity length is satisfied at the wavelength where the mirrors contribute no addition phase change, $n_L\Delta_H = -n_H\Delta_L$ from equation (3-35), the resonance wavelength will be unaffected by the mirrors. If, on the other hand, the bare cavity resonance occurs at a wavelength shorter than that for zero phase from the mirrors, equation (3-39) indicates that the mirrors will provide a positive addition to the round-trip phase. This will shift the resonance wavelength for the cavity plus DBR mirrors to a longer wavelength where less phase change is accumulated in traversing the cavity. The opposite will happen if the bare cavity resonance wavelength is longer than the wavelength for zero reflected phase from the mirrors. In either case, because of the penetration of the optical field into the DBR mirrors, the bare-cavity resonance will be shifted to toward the wavelength of zero reflected phase for the mirrors.

The net result is that one must consider the phase characteristics of both the mirror and the cavity in determining the phase addition that must be supplied to move the cavity resonance. Specifically, examining the resonance condition as a function of wavelength, one must supply

$$\Delta\phi \approx [2(d\phi/d\lambda)_{mirror} + (d\phi/d\lambda)_{cavity}]\Delta\lambda, \tag{3-43}$$

to move the resonance an amount, $\Delta\lambda$. The phase characteristic, $d\phi/d\lambda$, for the cavity is obtained by differentiating the expression for the round-trip phase change for propagation through the bare cavity,

$$\left.\frac{d\phi}{d\lambda}\right|_{cavity} = \frac{d}{d\lambda}\left(2\frac{2\pi nL}{\lambda}\right) = -\frac{4\pi nL}{\lambda^2}. \tag{3-44}$$

$d\phi/d\lambda$ for a DBR mirror is described by equations (3-39). For a VCSEL with a one wavelength cavity and GaAs/AlAs mirrors, the magnitude of these terms are,

$$\left.\frac{d\phi}{d\lambda}\right|_{mirror} \approx -\frac{17.3}{\lambda} \quad \text{and} \quad \left.\frac{d\phi}{d\lambda}\right|_{cavity} \approx -\frac{12.6}{\lambda}, \tag{3-45}$$

indicating that, for a typical GaAs/AlAs VCSEL design, the characteristics of the mirrors are almost 3 times as important in determining the resonance wavelength as the physical length of the cavity.

If the resonance is at too short a wavelength and the growth interruption has been made right after the cavity is grown, the additional phase can be supplied in a straight forward manner by simple addition to the cavity when growth is resumed. If, on the other hand, the resonance is at too long a wavelength or the interruption takes place at a point within the top DBR mirror, the phase change must be supplied by altering the thickness of a mirror layer.

With reference to Figure 3-7, the top DBR mirror can be analyzed as two mirrors, M_1 and M_2, separated by a spacer that differs from a quarter wavelength by Δx. Starting from Siegman's analysis,[26] one can determine the change in reflected phase looking from the cavity side as a function of Δx to be,

$$\Delta\phi \approx \left(\frac{4\pi n_L}{\lambda}\right)\frac{r_2(1-r_1^2)}{(r_1+r_2)(1+r_1r_2)}\Delta x, \tag{3-46}$$

where r_1 and r_2 are the amplitude reflection coefficients for mirrors M_1 and M_2 and n_L is the refractive index of the spacer layer. The change in magnitude for the power reflection

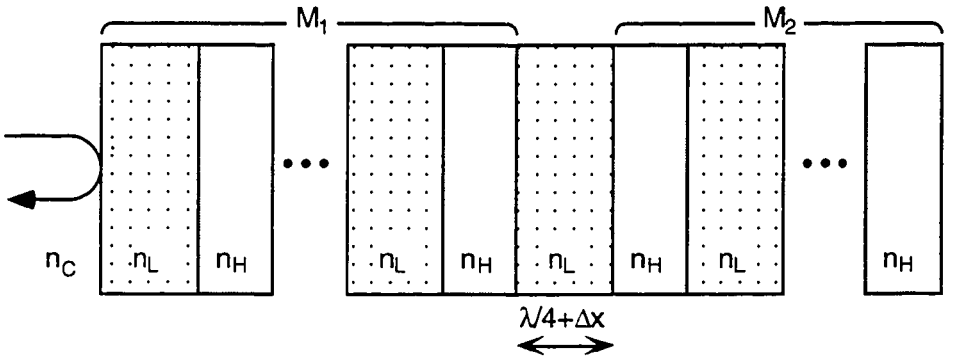

Figure 3-7: Schematic of top DBR mirror illustrating the effects of altering the thickness of one mirror layer.

for the top DBR mirror as a result of the correction is.

$$\Delta R \approx \left(\frac{4\pi n_L}{\lambda}\right)^2 r_1 r_2 \frac{(1+r_1r_2)^2-(r_1+r_2)^2}{(1+r_1r_2)^4}\Delta x^2. \tag{3-47}$$

Although the approximations in equations (3-43) and (3-46) give a feel for the importance of the various device parameters in determining the cavity resonance and are very effective for determining small corrections,[27] numerical simulations of the structure do not take much more time and are accurate for much larger corrections. To determine the correction numerically, one simulates the structure that exists at the time of the growth interruption. The bottom DBR mirror period in the simulation is adjusted so the center wavelength of the simulated and measured high-reflectivity bands are aligned. The cavity length and loss are also adjusted in the simulation so that the position and depth of the Fabry-Perot dip match the measurement. The correction is then determined in an iterative fashion by adjusting the thickness of the next layer to be grown in the simulation of the completed structure.

In this analysis, it is assumed the wavelength for zero reflected phase is known. In practice, however, one can substitute the mirror's center wavelength as long as the duty cycle of the mirror is close to 50%. The percentage error in estimating the zero phase wavelength by the center wavelength is shown in Figure 3-8. Even in the extreme case of a 2% error in the duty cycle, the error in the estimate of the zero phase wavelength is only 0.3%. Because of the competition between the cavity and mirror for determining the resonance wavelength, the resulting error in the position of the cavity resonance will be even smaller.

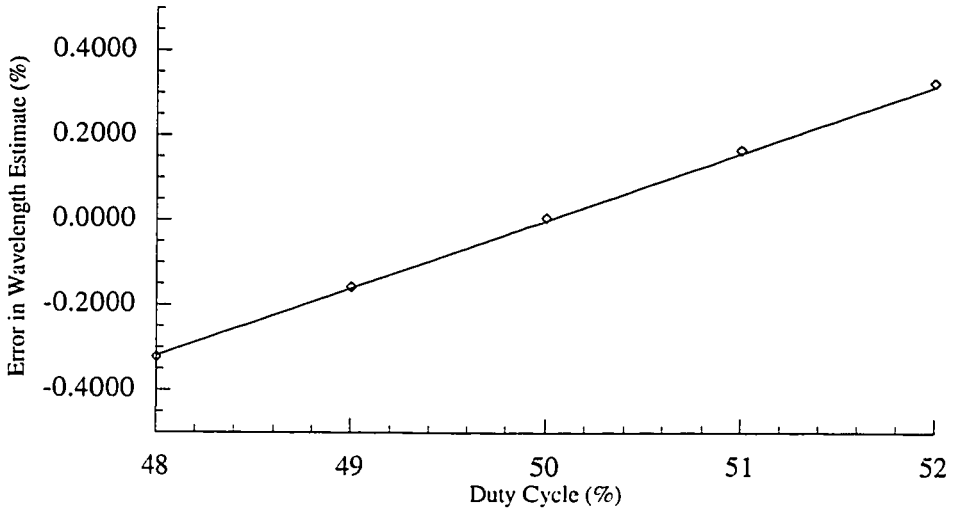

Figure 3-8: Percentage error in estimating the wavelength for zero reflected phase by the center wavelength as a function of the duty cycle.

3.2.2 Results: VCSELs and Multiple Wavelength VCSELs

The growth of a typical VCSEL will demonstrate this technique in practice. This example comes from the growth of wafer #3664. From the absorption peak of a test quantum well sample,[28] the target wavelength for the wafer was set to be 9680 angstroms. After the bottom mirror and cavity were grown, the wafer was cooled to room temperature and the reflectivity measured. The reflectivity spectrum at this point, Figure 3-9, revealed a center wavelength for the mirror at 9616 angstroms and a Fabry-Perot dip, corresponding to the cavity resonance, at 9500 angstroms. These features were matched in a simulation by assuming GaAs/AlAs mirror layer thicknesses of 681 Å/812 Å instead of the designed thicknesses of 685Å/818Å and a cavity shortened by about 3% from the design. Adding the top DBR mirror in the numerical simulation, it was determined that an additional 90Å should be added to the cavity to shift the cavity resonance to 9680Å. The reflectivity spectrum of the final structure in Figure 3-10 shows that the cavity resonance at wafer center has been shifted to 9700Å by this addition, only 0.2% from the target value.

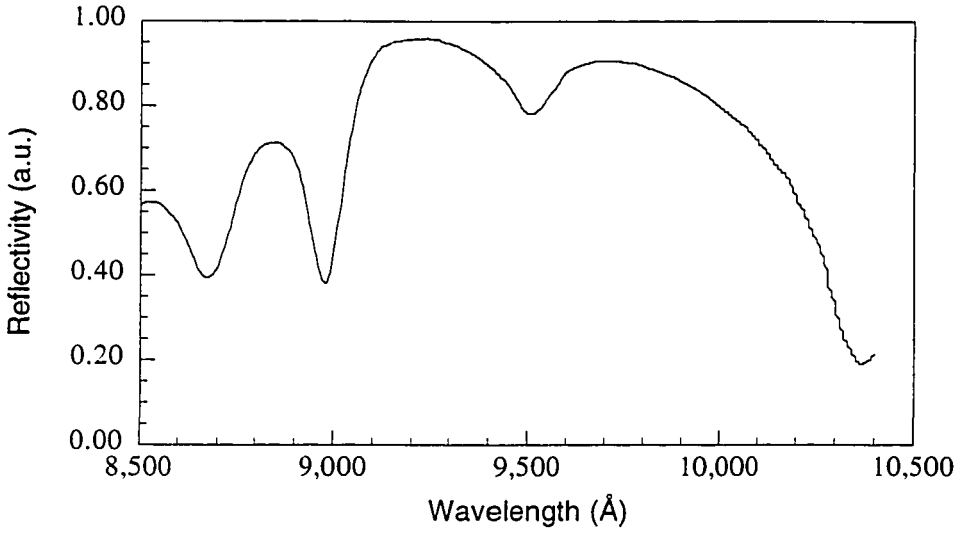

Figure 3-9: Reflectivity of wafer #3664 after bottom DBR mirror and cavity.

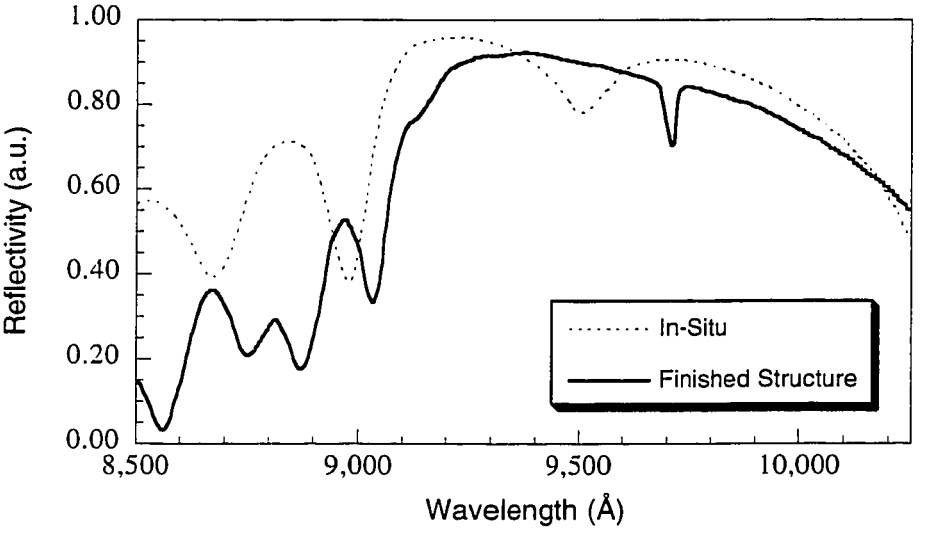

Figure 3-10: Reflectivity of wafer #3664 at growth interruption (In-Situ) and after completion (Finished Structure).

Another example illustrates the extreme of corrections that can be made with the technique. In order to enable the processing of multiple wavelength VCSEL arrays from a single wafer, a periodic temperature gradient was applied to a VCSEL wafer during growth.[29] The mirrors and active region were grown at a substrate temperature where the growth rate is insensitive to substrate temperature variations, but the cavity was grown at high temperature where the thermal desorption of gallium, which is exponentially dependent on temperature,[30] creates a cavity thickness variation corresponding to the applied temperature gradient.

The variation of growth rate due to gallium desorption, while producing the desired lateral variation of cavity resonance, also causes a large uncertainty in the average growth rate. The in-situ reflectivity measurement taken after the cavity was completed, Figure 3-11, illustrates this point. Although the mirror center wavelength was only 1.8% short of the target wavelength, the cavity resonance for the hot region at 9250 Å was well short of the desired wavelength of 9680 Å.

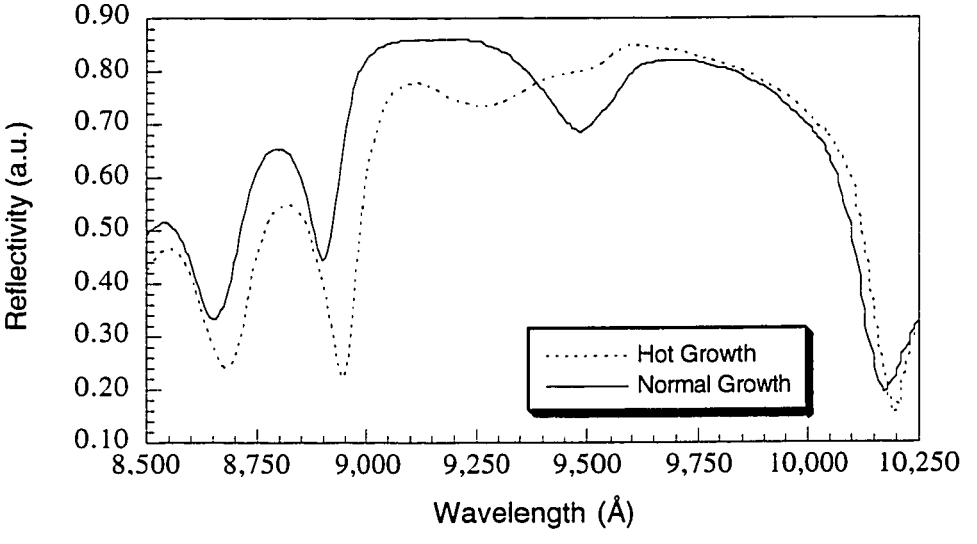

Figure 3-11: In-situ measurement of multiple wavelength VCSEL, wafer #3704.

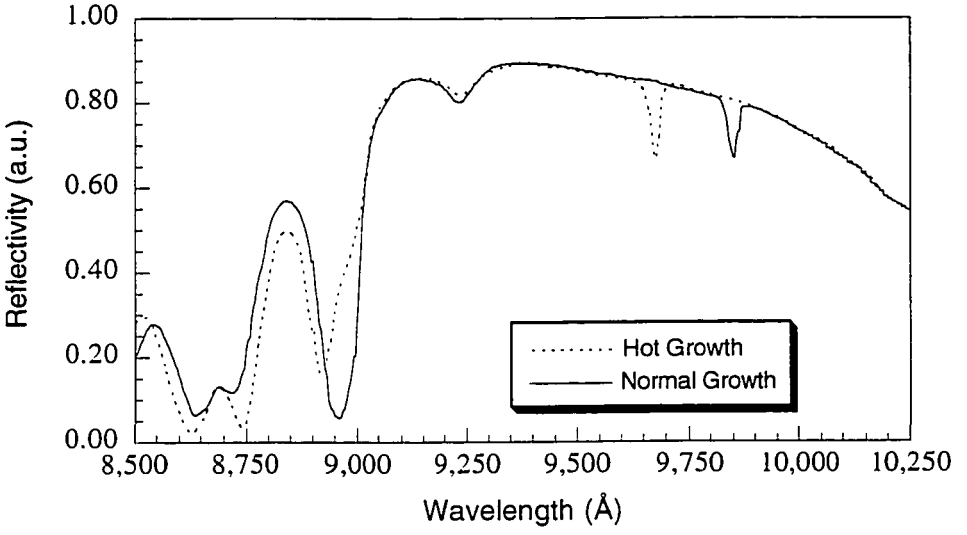

Figure 3-12: Final reflectivity measurement of wafer #3704 showing the cavity resonance extremes at 9675 Å and 9850 Å.

The cavity was extended 210 Å and the top DBR mirror grown to complete the structure. Figure 3-12 shows the reflectivity measurement of the final structure. The resonances in the two regions have been shifted approximately 400 Å to 9675 Å and 9850 Å, respectively.

As a result of the cavity correction, we were able to obtain working devices across the entire transition between the two regions. Arrays of broad-area lasers were fabricated from this wafer. Figure 3-13 shows the lasing wavelength as a function of position in an array situated in the transition area between the hot and cold growth regions, illustrating over 20 nanometers of wavelength shift across the array. Because the array was not in the center of the wafer, the wavelength extremes are slightly shorter than those indicated by the reflectivity measurements.

As a caveat, the light output vs. current curves for three lasers in the transition region are shown in Figure 3-14. Since the active region was grown at temperatures where there is no significant desorption of material, the gain spectrum is relatively uniform

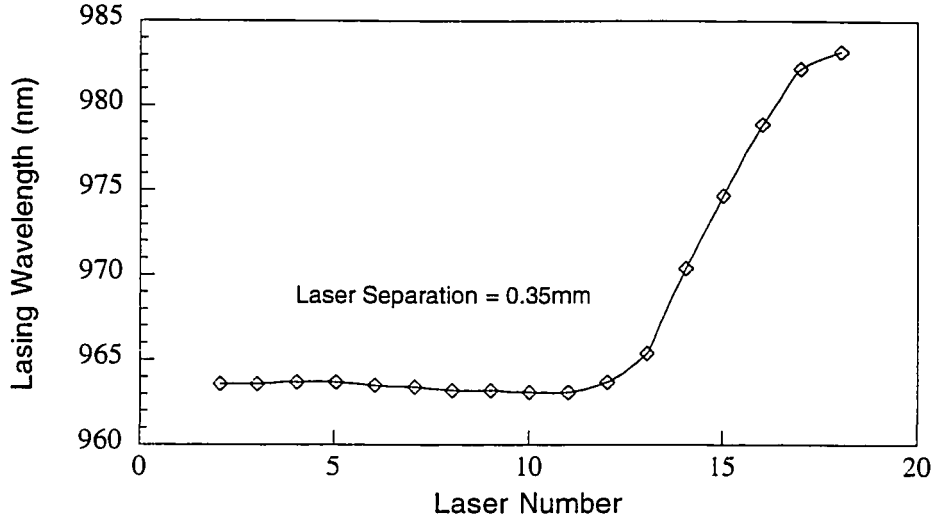

Figure 3-13: Lasing wavelengths of an array fabricated from wafer #3704.

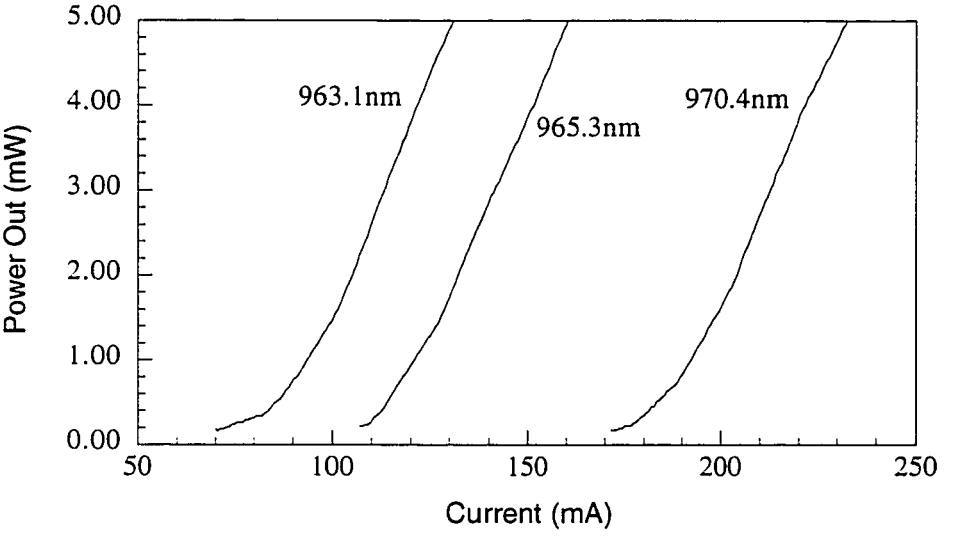

Figure 3-14: L-I curves of 3 lasers at different positions in the array.

across the array. As the lasing wavelength, determined by the cavity mode, shifts to longer wavelength, then, the overlap between the gain and the cavity mode is decreased. As a result, more current is needed to achieve lasing. This illustrates the importance of being able to accurately position the cavity resonance with respect to the gain spectrum for achieving efficient laser characteristics.

4. P-type DBR Mirrors

P-type mirrors have long been considered the bottleneck for improving the performance of electrically-pumped VCSELs and much work has been done to improve their design.[31,32,33] Not only does the high series resistance associated with the mirrors degrade the wallplug efficiency of devices though ohmic losses, but the resulting heating limits their operation at high injection levels. As the device heats up, the gain peak shifts to longer wavelength at the rate of about 3.5 Å/°C due to a reduction of the bandgap energy with temperature.[34] The Fabry-Perot resonance also shifts to longer wavelengths due to the temperature dependence of the refractive indices, however, at the much lower rate of 1.0 Å/°C.[35] This mismatch between the rates at which the gain and cavity mode shift with temperature causes the output power to decrease and lasing to terminate at high injection currents.[36] Since, from equation (2-18), high-efficiency performance requires operation well above threshold with a small voltage drop outside the active region, the importance of reducing the series resistance of the mirrors is clear. The following sections will discuss the origin of the high resistance and ways of reducing it. Finally a mirror design will be presented that provides very low resistance, high-reflectivity per period p-type DBR mirrors suitable for high-efficiency VCSELs.

4.1 Mirror Resistance

By their nature, distributed Bragg reflector mirrors require alternating layers of different materials to produce high reflectivity. The GaAs/AlAs material system is well suited for this purpose because it is very closely lattice matched and offers a reasonable change in refractive index. This index change is associated with differences in bandgap energies between the two materials,[37] however, which can lead to transport problems in electrically pumped devices.

Figure 4-1, shows a band diagram for a heterojunction in a p-type DBR mirror. Approximately 35% of the direct bandgap difference shows up as a discontinuity in the valence band.[38] This discontinuity leads to a barrier preventing holes from crossing the junction. A small positive bias on the AlAs side of the junction will reduce the barrier and allow holes to flow from the AlAs to the GaAs, but the opposite is not true, however. A small negative bias on the AlAs side will not significantly lower the barrier because the GaAs material near the junction is degenerate. Significant current will only flow from GaAs to AlAs when the bias is increased so that the barrier is thin enough for holes to tunnel through. This rectification by a single p-P heterojunction is demonstrated in the calculations of Yoffe,[39] shown in Figure 4-2. One forward-biased and one reverse-biased p-P junction is encountered every mirror period, potentially leading to very large voltage drops for the whole mirror.

Making matters worse, beryllium, the common p-type dopant in MBE, has a very high mobility in AlAs. This causes the doping concentration to decrease in the AlAs layers of the mirrors and accumulate on the GaAs side of the junction,[40] making the

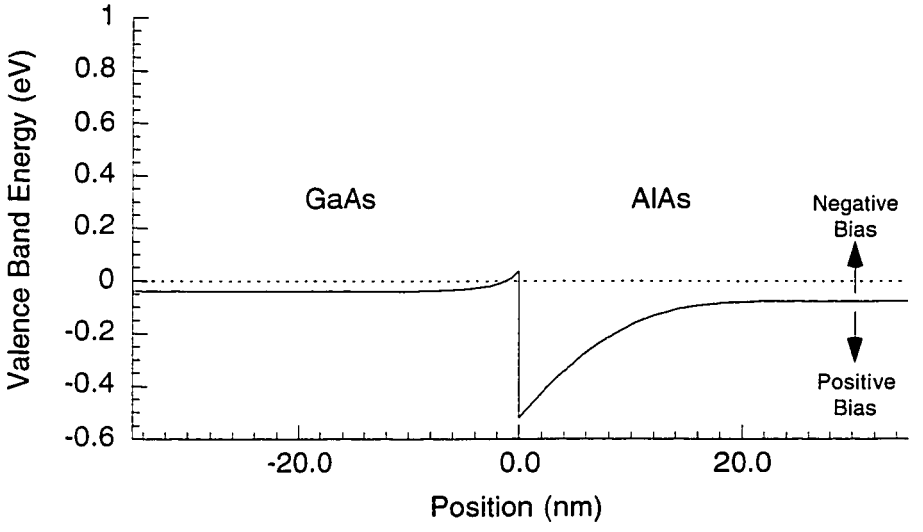

Figure 4-1: Plot of valence band energy at an abrupt, p-type GaAs/AlAs heterojunction.

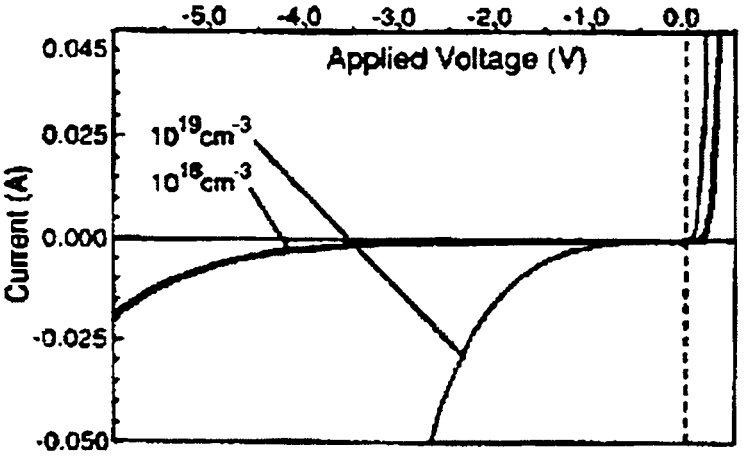

Figure 4-2: Calculated I-V characteristics of p-type GaAs/AlAs heterojunctions uniformly doped at 10^{18} cm^{-3} and 10^{19} cm^{-3} from reference 39. The device area is $5x10^{-5}$ cm^2.

barrier effectively wider.

The cumulative effects are illustrated in Figure 4-3 which shows the current-voltage relationship for two 10 period p-type DBR mirrors in series. The extreme of the

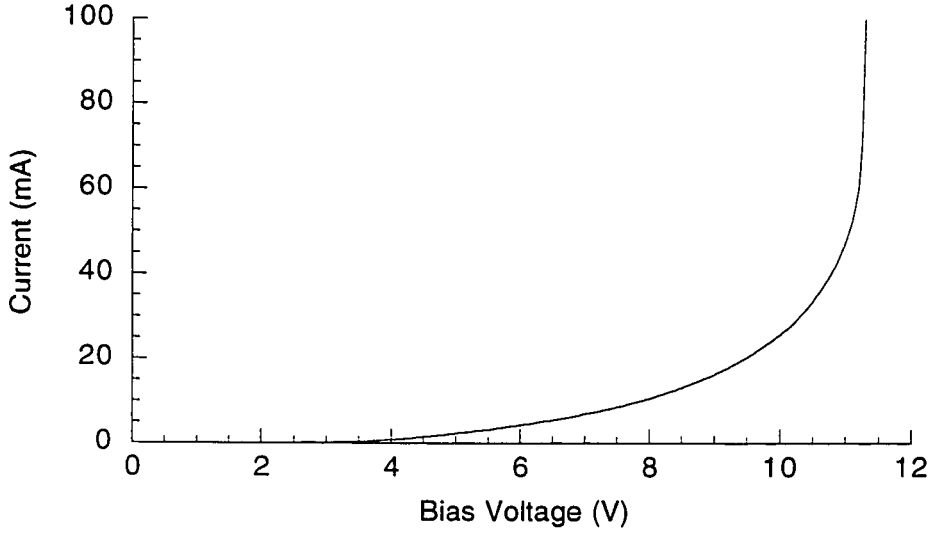

Figure 4-3: Current-voltage characteristics for 2 ten period GaAs/AlAs DBR mirrors in series.

current scale corresponds to the approximate current density for which lasing would be expected in a broad area VCSEL. Compared with the greater than 11 volt drop across the mirror, only 1.3 volts are needed to produce 960 nm photons. Thus, the power lost in the mirrors is almost an order of magnitude greater than that which is needed for an ideal laser. By equation (2-18), this alone would limit the wallplug efficiency of a laser with such mirrors to less than 11%, even if the laser were otherwise ideal.

4.2 Reducing Valence Band Discontinuities

It is not surprising, then, the amount work which has been done on reducing the valence band discontinuities and their effects on the p-type mirrors of VCSELs. The attempts can be generally grouped into two categories, higher doping and compositional grading. Both techniques on their own have drawbacks; however, a correct combination of the two can theoretically lead to an almost ideal electrical transition between the two mirror layers.

4.2.1 Compositional Grading

Compositional grading attempts to smooth the discontinuities by including intermediate $Al_xGa_{1-x}As$ compositions to spread the GaAs/AlAs transition over hundreds of angstroms. Figure 4-4 illustrates grading techniques which have been employed to improve the transport through DBR mirrors. The simplest, step grading, includes one or two intermediate composition layers on the order of 100 angstroms thick to accomplish the transition. This technique replaces the one large discontinuity with a few smaller discontinuities resulting in a significant improvement in the current-voltage characteristics for the mirror.[41]

Digital grading is an MBE technique to approximate a continuous compositional grade with a short period superlattice of varying duty cycle. [42,43] It is particularly suited to MBE because rapid transitions between the binary compositions can be accomplished with shutter operations, whereas continuous compositional grading would require

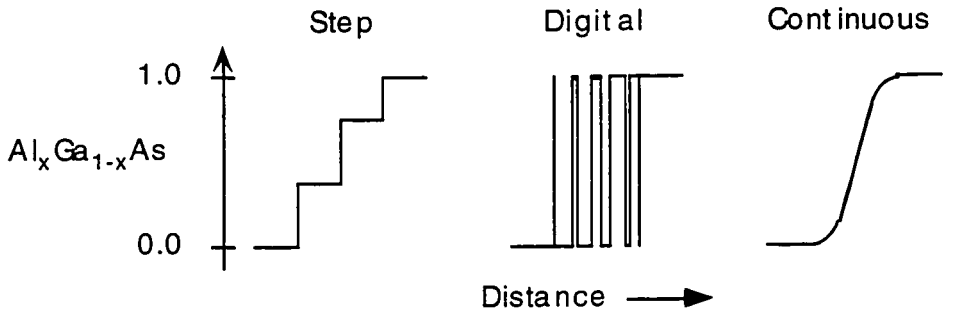

Figure 4-4: Techniques for grading between GaAs and AlAs in DBR mirrors.

adjusting effusion cell temperatures, a thermal (slow) process. If the period of the superlattice is small enough, a carrier will act as if it is in a material with composition equal to that of the local average of the superlattice.[44]

Figure 4-5 shows a comparison of the current-voltage characteristics of two digitally graded mirrors with the abrupt-interface mirror shown previously. For the linearly graded mirror, the 170 angstrom graded region was broken up into six 10 monolayer sections with duty cycles varying from 10 to 90 %. For the quasi-parabolic

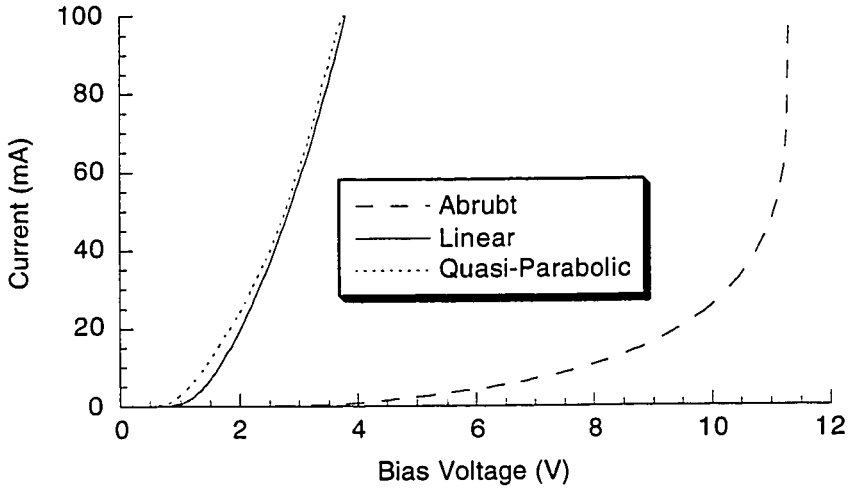

Figure 4-5: Comparison of graded junctions with abrupt junctions in p-type DBR mirrors.

graded mirror, the 136 angstrom graded region was broken up into 8 sections of different thickness, with the duty cycle also ranging from 10 to 90 %. In these mirrors, the average composition, x, of the $Al_xGa_{1-x}As$ digital alloy was varied linearly or parabolicly with distance. This is in contrast to later work to be presented where the composition is graded in a manner to produce a parabolic change in the valence band energy. Even with the short graded region, the reduction in voltage is significant. The two grading schemes yield very similar results, except at low current densities where the quasi-parabolic grading is slightly better. The nonlinearity of the I-V curves, however, indicates there are still barriers for the carriers to surmount, leading to a voltage drop which is still twice that required across the active region.

As one extends the width of the transition region to reduce the potential barriers further, continuous grading becomes a viable option. Chalmers, et. al., reported resistivities as low as $1.8x10^{-5}$ Ω-cm^2 for 20 period mirrors using piecewise linear continuous grading and relatively high, $5x10^{18}$ cm^{-3}, doping.[45] More recently, this group has reported specific mirror resistance as low as $0.8\ x10^{-5}$ Ω-cm for 10 period mirrors with lower doping using longer graded regions grown by Metal-Organic Vapor Phase Epitaxy (MOVPE).[46] The major drawback to longer grading, however, is the lower reflectivity per mirror pair. The best mirrors reported by Lear, et. al., had a reflectivity of only 0.90 from a ten period DBR stack as opposed to the 0.96 expected from abrupt interfaces. The lower reflectivity per pair translated into larger mirror stacks and increased penetration of the optical field into the mirror. The latter can lead to increased losses from free-carrier absorption, scattering, and diffraction.

4.2.2 Increasing Doping

Probably the simplest method to reduce the voltage drop across the DBR mirrors in VCSELs is to increase the doping. By narrowing any potential spikes to aide tunneling and, in the extreme, even making the material degenerate, less additional energy is required to force the carriers across the junction. As one might expect, the doping only needs to be

increased in the graded region to see the reduced voltage drop.[47] Yoffe points out, however, that even with very high doping, some compositional grading is still needed.[48] Furthermore, the high free-carrier densities associated with the higher doping raises the concern of higher free-carrier absorption losses in such mirrors.

4.2.3 Modulation Doping

A more elegant technique for reducing valence band discontinuities in p-type DBR mirrors involves compensating the change in crystal potential across a graded junction with the built-in field caused by a modulated doping profile.[49] The excess free carriers from the more heavily doped regions redistribute into the more lightly doped regions, theoretically producing a nearly flat valence band. Although first applied to VCSEL mirrors by Schubert, et al., [50] this idea had previously been used for the realization of three-dimensional electron gases in GaAs/AlGaAs parabolic wells.[51]

Peters, et al., extended this idea to produce the mirror design shown in Figure 4-6. The aluminum concentration is graded between the two mirror layers so that the crystal potential varies parabolicly with distance from either endpoint to the middle of the junction. The graded region on the GaAs side of the junction is left undoped, while the other half is doped at twice the doping of the rest of the mirror.

The situation can be roughly analyzed by first assuming that the valence band is indeed flattened. Because the difference between the Fermi level and the valence band is then constant, there will be a constant concentration of free holes through the graded

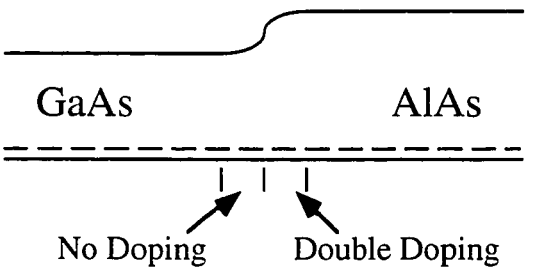

Figure 4-6: Schematic of modulation doped GaAs/AlAs junction.

region. This implies that there will be an excess of positive charge density equal to the average doping density on the undoped side of the junction due to free holes and an equal and opposite charge on the more heavily doped side due to an excess of ionized acceptors. As can be seen from Poisson's equation, this charge distribution will cause a parabolic band bending that compensates for the change in crystal potential due to the compositional grading. Thus, the sum of the doping potential and the crystal potential yields a flat valence band as we assumed. One would expect some residual valence band variation due to small changes in material constants, such as dielectric permitivity and valence band effective density of states, with composition.

Other combinations of doping distribution and crystal potential profile are also possible. For example, one could use a linearly graded crystal potential with a delta-doped excess charge density spike on either side. Although the excess charge sheets would cause a constant electric field in the region leading to a linear change in potential, achievable delta-doping levels would require an unacceptably large graded region to achieve a flattened valence band. The constant doping / parabolic grading combination is thus attractive because it provides the prospect of flattening the valence band with simple, realizable doping and grading profiles.

For reasonable free carrier levels, 1-2 $x10^{18}$ cm^{-3}, to avoid large free carrier absorption, this scheme still relies on fairly large graded regions which will reduce the mirror reflectivity. In the Peters paper for example, with an average free carrier concentration of $1x10^{18}$ cm^{-3} the transition region needed was 224 Å thick to grade from GaAs to $Al_{0.67}Ga_{0.33}As$, the composition used for the low index mirror layer. The combination of graded regions and reduced Al composition dictates that 30 or more periods are needed for very high reflectivity mirrors.

4.2.4 Addition of Si Doping

Applying the above technique to GaAs/AlAs mirrors would require approximately 400Å long graded regions, more than half the mirror length. To reduce the

grading length, one must increase the charge density in the transition region. Although this can be accomplished by raising the average doping, the free carrier concentration is proportional to the doping, whereas the grading length is inversely proportional only to the square root of the doping. As a result, one would need to quadruple the doping to reduce the grading length by a factor of two.

A solution is to use Si (n-type) doping on the GaAs side of the junction to increase the obtainable negative charge density for a given average doping concentration. The p-type doping on the other side of the junction is increased as well to compensate. Although the doping is increased, because of the redistribution of carriers and compensation, the free carrier concentration should be maintained at the average doping level that exists outside the graded regions. With the addition of $7x10^{18}$ cm^{-3} Si atoms, one can grade from GaAs to AlAs in 130Å with a free carrier concentration of only $2x10^{18}$ cm^{-3}.

4.2.5 Carbon Doping

As the donor doping on the GaAs junction is increased, so must the acceptor doping on the AlAs side. For the mirror presented, this requires a p-type doping level of $1.1x10^{19}$ cm^{-3} for the 65 angstroms of the graded region on the AlAs side. While this is easily obtainable in GaAs with Be, high diffusivity and low solubility limit the doping level of Be in AlAs to about 5×10^{17} cm^{-3}.[40]

To obtain the high doping levels needed for this work, carbon doping from an ohmic heated graphite filament was used. Fischer and Ploog demonstrated that the free-hole concentration from C doping does not saturate until $3x10^{19}$ cm^{-3} in GaAs and $6x10^{19}$ cm^{-3} in AlAs.[52] Short minority-carrier lifetimes experienced with carbon-doped heterojunction bipolar transistors[53] should not be a problem with carbon-doped laser diodes because the n- and p-type dopants are generally confined to the cladding region where the minority-carrier concentrations should be very small. In fact, very low

threshold current density carbon-doped edge-emitting lasers have been demonstrated[54] which tends to support this point.

4.3 Low Resistance P-type Mirrors

Two ten-period p-type mirrors were grown to test the effectiveness of adding an n-type doping to p-type DBR mirrors. The graded regions of both mirrors follow the design of Figure 4-7. The excess charge density dipole in the graded region is $q \cdot 9x10^{18}$ cm^{-3}, which allows the grading between GaAs and AlAs layers to be completed in 130 Å. For one sample, #3910, the average doping, X, is held constant at $2x10^{18}$ cm^{-3}. The corresponding doping levels in the graded region are $7x10^{18}$ cm^{-3} (silicon) on the GaAs side and $1.1x10^{19}$ cm^{-3} (carbon) on the AlAs side. For the other sample, #3899, the average doping is varied from $2x10^{18}$ cm^{-3} for the first period, to $4x10^{18}$ cm^{-3} for the next three periods, to $8x10^{18}$ cm^{-3} for the last 6 periods. The n- and p-type doping levels in the graded regions for these average doping concentrations are $7x10^{18}$ cm^{-3}/$1.1x10^{19}$ cm^{-3}, $5x10^{18}$ cm^{-3}/$1.4x10^{19}$ cm^{-3}, and undoped/$1.7x10^{19}$ cm^{-3} respectively.

4.3.1 Growth

A digital alloy was used to perform the compositional grading. The graded region was divided into 8.5Å regions and the duty cycle of the Al and Ga shutter openings was varied so the average AlGaAs composition for the region corresponded to the target for the center of the region. The growth rates for the Ga and Al sources were matched, so the doping concentration would be independent of the duty cycle.

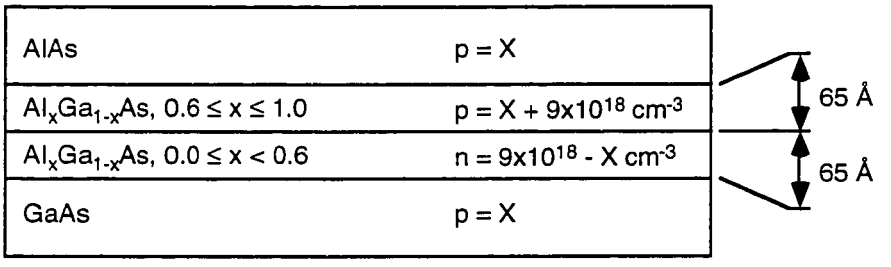

Figure 4-7: Schematic of doping in graded regions of Si/C doped p-type mirrors.

At the start of a transition from GaAs to AlAs, the carbon shutter was closed, the silicon shutter was opened, and the current through the carbon filament was adjusted for the higher doping level on the AlAs side of the junction. At the midpoint of the graded region, a growth interruption of 15-60 seconds, depending on the change in current level, was included to allow the carbon source to stabilize at its new temperature. The rest of the graded region was then grown. Upon completing the graded region, another growth interruption was performed to return the carbon source to the lower doping level for the ungraded regions. For the transitions from AlAs to GaAs, this sequence was performed in the reverse order.

4.3.2 Electrical Measurements

The specific resistance of the mirrors was measured by the Transmission Line Method (TLM).[55] The resistance between contacts separated by different spacings are measured with a four point resistance measurement and the results are used to determine the specific contact resistance and sheet resistivity. In order to separate the contribution of the metal-semiconductor contact resistance from the mirror resistance, two adjacent sets of TLM pads were used, Figure 4-8. From the first set of pads, the specific contact resistance is measured normally. The mirror is etched away between the contacts of the second set of pads, however, so a measurement on this set reveals the series addition of the contact resistance with the mirror resistance. Subtraction of the two results yields the

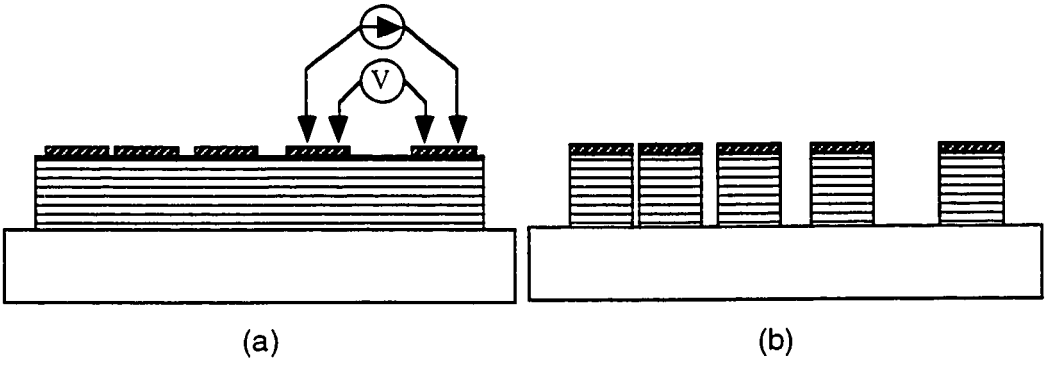

Figure 4-8: TLM pads for measuring the specific mirror resistivity. Set a) measures contact resistance, while set b) measures the sum of contact plus mirror resistance.

resistivity of the mirror.

4.3.3 Results

A typical I-V curve of two 10 period mirrors in series, Figure 4-9, illustrates that the mirrors are very ohmic and that the voltage drop is reduced by about two orders of magnitude compared to the mirrors of Figure 4-5. Averaged measurements of the resistivity with standard deviation for modulation doped mirrors are listed in Table 4-1. Although the resistivity of both mirrors is very low, the factor of five difference in the resistivity is larger than the factor of 3 expected from the difference in the average doping level.

A possible source of this discrepancy is the higher contact resistance of sample #3910. The doping of the contact layer in this sample was only $2x10^{19}$ cm^{-3}, leading to a measured contact resistivity of $1.3x10^{-4}$ Ω-cm^2, as compared to $1.1x10^{-5}$ Ω-cm^2 for sample #3899. Since the contact resistance was so large compared with the mirror resistance, a small error in either of the TLM measurements on this sample would

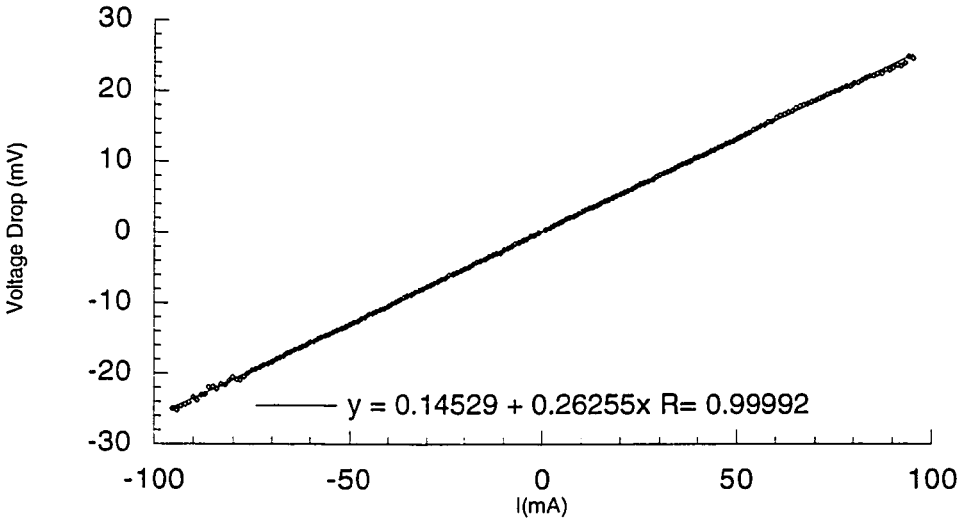

Figure 4-9: Current-voltage curve of two 10-period mirrors in series.

Table 4-1: Characteristics of p-type Si/C modulation doped mirrors.

Wafer #	Doping	Resistivity	Reflectivity
3899	1-2x10^{18} cm^{-3} 3-4x10^{18} cm^{-3} 6-8x10^{18} cm^{-3}	4x10^{-6} Ω-cm^2	0.946
3910	10-2x10^{18} cm^{-3}	2x10^{-5} Ω-cm^2	0.958

produce a much larger error in the calculated mirror resistance.

The peak reflectivity of the mirrors was measured to be 94.6% for sample #3899 and 95.8% for sample #3910. To correct for the system response in these reflectivity measurements, the results were divided by the measured reflectivity of a gold sample (>1200 Å of gold deposited on a flat substrate under high vacuum conditions). The reflectivity of the gold was assumed to be 98% for wavelengths just under one micron. Figure 4-10, shows a comparison of these mirrors with the best reported mirrors in the literature.[43] The mirrors in the comparison were grown by Metal-Organic Vapor Phase Epitaxy (MOVPE) using long grading regions. As can clearly be seen, the reflectivity is

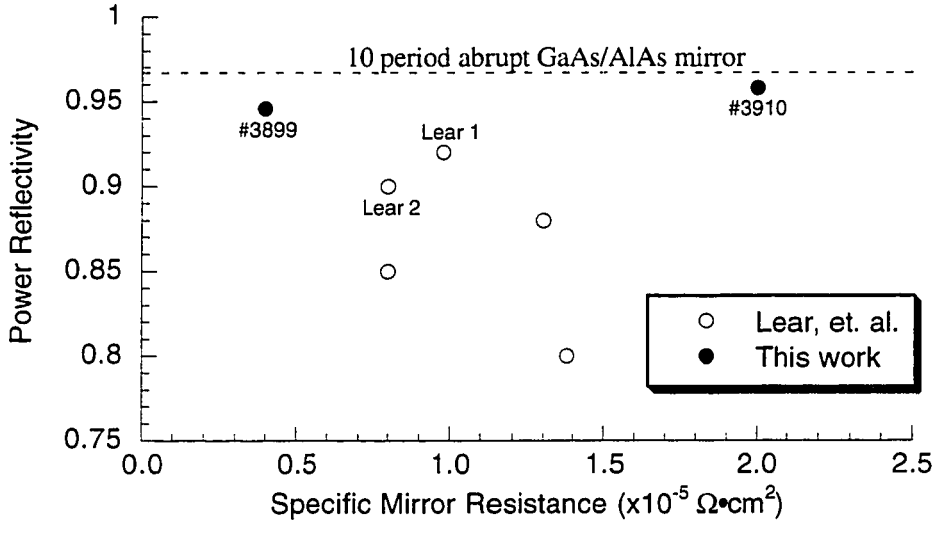

Figure 4-10: Comparison of ten period DBR mirrors from this work with those in reference 46.

significantly lower for mirrors with long graded regions. The addition of silicon in a modulation doped, parabolicly graded, p-type DBR mirror allows the simultaneous achievement of very low mirror resistivity with a high reflectivity per mirror pair.

4.3.4 Optical Simulations

To compare the free-carrier absorption of different mirror designs, it is important to consider the optical penetration depth of the mirror. In an abrupt junction mirror, for example, the optical wave will decay faster and thus will experience less free carrier absorption than in a graded-junction design with the same doping levels. One can take advantage of the optical decay by raising the doping levels in the mirror away from the active region.[56] This, however, makes the comparison of loss expected from different mirror designs more complicated than just comparing the free carrier levels in the mirror.

The optical penetration depth can be characterized by an effective reflectivity per mirror pair.[57] This allows a way of comparing different grading schemes by modeling the distributed reflectance by a lumped reflectance at the interface. In effect, the graded junction is replaced by an abrupt junction with an index difference such that it gives the same aggregate reflectivity.

Using this approach, the free carrier absorption as a function of the per-period mirror reflectivity of twenty period DBR mirrors was simulated for four different doping schemes. Table 4-2 summarizes the doping schemes examined. For all mirrors, the lowest doping is near the cavity where the optical field is the largest. Mirrors number 1 and 4 are meant to mimic the doping of the mirrors in the previous section, except for double the number of periods. The higher the mirror number, the more quickly the doping

Table 4-2: Summary of doping schemes in absorption simulation.

Mirror #	Doping Scheme (# of periods @ doping level)
1	20 @ $2x10^{18}$ cm^{-3}
2	10 @ $2x10^{18}$ cm^{-3}, 10 @ $8x10^{18}$ cm^{-3}
3	4 @ $2x10^{18}$ cm^{-3}, 6 @ $4x10^{18}$ cm^{-3}, 10 @ $8x10^{18}$ cm^{-3}
4	2 @ $2x10^{18}$ cm^{-3}, 6 @ $4x10^{18}$ cm^{-3}, 12 @ $8x10^{18}$ cm^{-3}

levels are raised with distance from the cavity.

The absorption coefficient due to free holes is taken from Casey and Panish[58] to be,

$$\alpha\ (cm^{-1}) \approx 7 \times 10^{-18} p,$$

where p is the density of free holes per cubic centimeter. From this, an extinction coefficient of 5.3×10^{-5} per 10^{18} cm^{-3} of holes can be determined. This is taken as the imaginary part of the index of refraction in the simulations.

The results of the simulation are shown in Figure 4-11. For reference, the R values indicated correspond to the power reflectivity for a ten period mirror with the given reflectance per interface and the two arrows on the left correspond to the best mirrors from Lear[46] shown in Figure 4-10. This enables the comparison among the mirrors to include the anticipated optical absorption in addition to the specific resistance and reflectivity. As expected, the modulation doped mirror with constant average free-

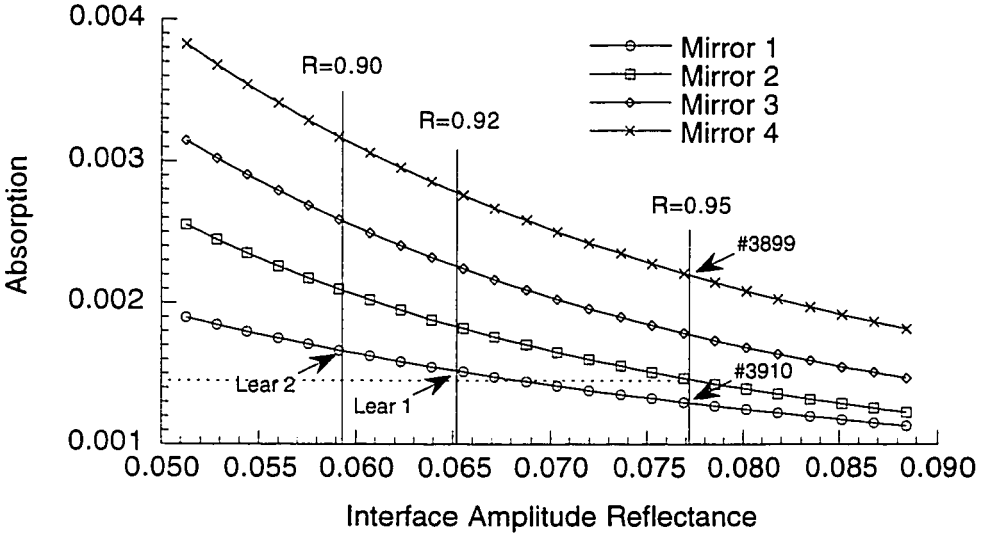

Figure 4-11: Simulated absorption as a function of reflectance per interface.

carrier levels from the previous section, wafer #3910, has the lowest absorption because of its low doping and high reflectivity per interface. It is also evident that the doping levels of wafer #3899 were increased too aggressively, so that the expected absorption is almost double that from wafer #3910. The doping scheme in the simulated mirror #2 seems to be a good compromise. By doping the first half of the mirror at $2x10^{18}$ cm^{-3} and the second half at $8x10^{18}$ cm^{-3}, one should be able to realize an MBE grown mirror that has higher reflectivity, lower resistance, and lower optical loss than any of the mirrors presented in reference 46.

5. VCSEL Processing

Since the cavity and gain region in a VCSEL are incorporated in the epitaxial design, all that remains to fabricate a device is a means to achieve population inversion in a controlled area of the active region in which the optical mode is confined. The conventional gain-guided design[59] relies on a high-energy proton implantation to funnel current into the active region. The change in index associated with the resulting gain profile provides lateral confinement to the optical mode. The performance of lasers fabricated in this manner is limited by factors associated with the implantation. Unintentional damage to the surface layers can increase the resistivity of such devices, especially those employing annular contacts for top surface emission.[60] Additionally, lateral ion-straggle limits the diameter of the devices to $\geq$ 5 microns and care must be taken to ensure that active region is not damaged. The following sections show an alternative method for achieving lateral current confinement in a top-surface-emitting VCSEL without resorting to implantation. This design, which takes advantage of the low resistance p-type mirrors of the previous chapter and a low resistance n-type intracavity contact, should enable the realization of very high-efficiency vertical-cavity top-surface-emitting lasers.

5.1 Intracavity Contacts

Intracavity contacts have been examined to reduce the series resistance associated with the p-type DBR mirror:[6162] The idea is to use an annular contact to inject current underneath the top mirror as opposed to through it. Because of the low hole mobility and large lateral distance carriers must travel to reach the center of the active region, contact layers 1 micron thick and high p-type doping were needed to reduce the threshold voltages. One would thus expect high optical losses from these intracavity contact designs..

With the advent of very low resistance p-type DBR mirrors,[63] bypassing the p-type mirror is no longer necessary. These mirrors, in fact, have lower series resistance than convential, linearly-graded n-type mirrors. For an n-type mirror, because a conduction-band electron scatters from the Γ-valley in GaAs to the X-valley in AlAs to travel through the mirror, the band-flattening technique of the previous chapter might have less applicability. Electrons, however, have a much higher mobility and lower free-carrier absorption, and thus are more suited for use in an intracavity contact layer. As will be demonstrated, this will enable a very low resistance contact to both the n- and p-type sides of the active region.

A schematic of a structure which uses an intracavity contact is shown in Figure 5-1. Because the top mirror is no longer in the current injection path, it can be left undoped to reduce free-carrier absorption. Current is injected through the n-type contact layer and confined by undercutting the AlAs layer beneath. These two layers actually form the bottom mirror period and must be an odd multiple of 1/4 wavelength in thickness. For mechanical integrity, the contact layer should be at least 3λ/4, approximately 200 nanometers, for GaAs at wavelengths just under 1 micron. The undercut layer is kept at

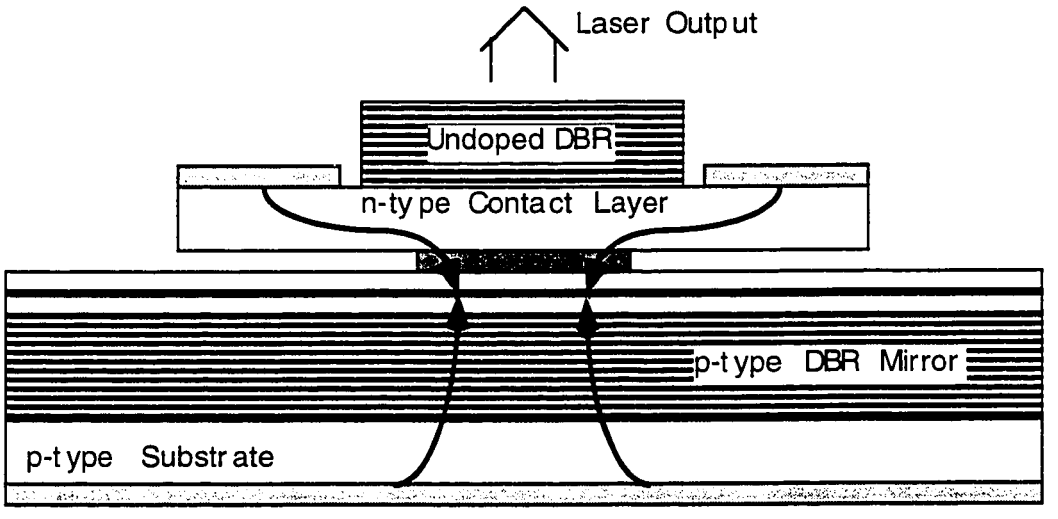

Figure 5-1: Schematic of intracavity contact VCSEL.

$\lambda/4$ minimum value.

In order to realize such a design, two problems must be overcome. First, one must be able to etch through more than two microns of the top DBR mirror and make ohmic contact to a relatively thin contact layer. Non-uniformity or inaccuracy in the etching will degrade device performance- overetching will increase the series resistance of the contact layer by unnecessarily thinning it, while underetching will preclude making contact at all because the top DBR mirror is undoped. Second, the injected current must be confined laterally so that gain is only created in the region under the top DBR mirror. Solutions to these problems will be presented in the following sections and should enable the realization of the intracavity contact design.

5.2 Selective Etching

In order to make contact to the n-type layer at the bottom of the top DBR stack, the mirror must be etched away very accurately and uniformly. Since the more than 2 microns of material must be etched and the contact layer may only be 0.2 microns thick, even a ±5% error in the etch depth will leave little chance of making a reliable contact. To make a reliable contact, a two-step selective etching process was developed which removes the mirror pairs one layer at a time. This technique relies on the periodic nature of the DBR mirrors to produce a much more accurate and uniform etch depth across the sample than can be obtained with timed etching.

A selective etchant is used to etch the top GaAs layer of a mirror stack and stop on the underlying AlAs. After a short, 2-5 second rinse, a different selective etchant is used to etch the now exposed AlAs layer. The two step etch process is then repeated for each mirror pair until the desired number of layers have been removed.

The first etchant, citric acid (citric acid monohydrate and water 1:1 by weight) and hydrogen peroxide in a 4:1 ratio, was used to etch GaAs preferentially over AlAs. It etches GaAs at greater than 4000Å/min. and AlAs at less than 3Å/min.[64] The second

etchant, used to etch AlAs preferentially over GaAs, consists of phosphoric acid, hydrogen peroxide and water[65] in a 3:1:50 ratio. This solution etches GaAs at approximately 800Å/min. and AlAs greater than 6000Å/min. Both etchants are reaction rate limited and isotropic.

Patterned pieces of bare GaAs were etched in the citric acid etch for times ranging from 10-60 seconds to characterize the citric acid etch. The resulting etch depths, measured with a Tencor Alphastep, are plotted in Figure 5-2. The linear relationship between etch depth and time reveals an etch rate of 89Å/s, while the offset from the origin indicates a delay of slightly more than 2 seconds before etching commences. This could correspond to the time needed to remove a surface oxide and must be taken into account when such a layer is allowed to form on the wafer.

Measurement of the AlAs etch rate by the phosphoric acid etchant is complicated by fact that the AlAs surface is not stable in the atmosphere. The time needed to etch the

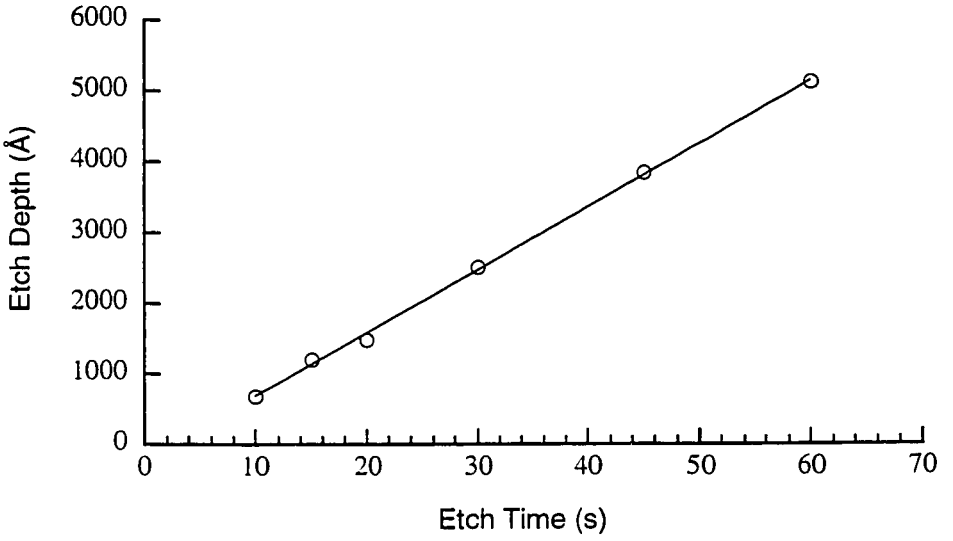

Figure 5-2: Etch depth vs. Etch time for etching GaAs with citric acid/hydrogen peroxide (3:1) etchant.

AlAs layer can be approximated visually, however. Etching AlAs in both this phosphoric acid based etch and a number of sulfuric acid based etchants produces a noticeably dark surface. When the AlAs has been completely removed, the exposed GaAs surface returns to its original mirror-like appearance.

The citric acid etch was used to expose an AlAs surface which was then etched with the phosphoric etch for various lengths of time. Examination of the resulting surface with an optical microscope revealed that it took between 7 and 8 seconds to remove an 810Å AlAs layer, corresponding to an average etch rate of approximately 110Å/s.

To allow for variations in the etch rate across the sample, one wants to overetch slightly with each etchant; however, overetching for too long will produce a large degree of undercutting. Figure 5-3 shows an SEM micrograph of 10 periods etched through a DBR mirror. Both GaAs and AlAs layers were etched for 11 seconds, about 1.5 times that necessary to etch through the layer. The mirror layers are 680Å GaAs/810Å AlAs and the patterns were aligned parallel to the natural cleavage planes. Although the etch depth is accurate, there is a large degree of undercutting, 4.3 microns, compared with the amount of vertical etching, 1.5 microns. Furthermore, there is a lot of debris on the surface and the AlAs layers are preferentially undercut.

These observations indicate that we may have drastically underestimated the AlAs etch rate. Simply reducing the etch time, however, results in an incompletely removed AlAs layer. A closer examination of the AlAs etching reveals that the "blackness" that forms on the surface is a porous layer that tends to lift off in large (greater than 100's of microns) sheets rather than being etched through. This layer seems to inhibit the vertical etching and only lifts off when the GaAs layer beneath is reached. The aspect ratio of the AlAs sidewall, less than 0.1 microns high by many microns wide, might allow this layer to lift off or break up easier than on the sample surface during etching leading to severe undercutting.

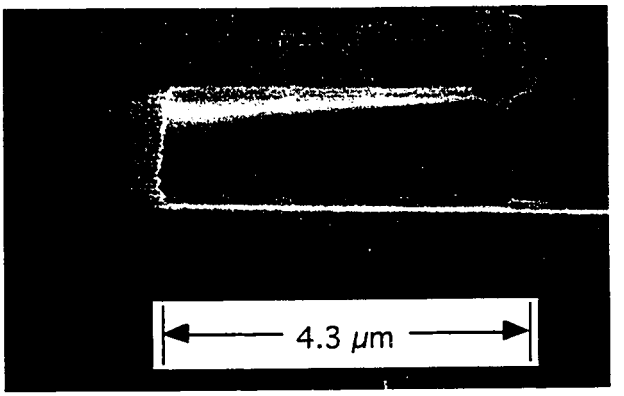

Figure 5-3: Cross-section SEM micrograph of ten periods of a 680Å GaAs/810Å AlAs DBR mirror etched with the selective etching process. Each layer is etched for 11 seconds in the appropriate selective etch.

We attempted to encourage the breakup and removal of the layer on the surface by doing the AlAs etch in an ultrasonic bath. Under these conditions, we were able to etch through the AlAs layers in 3-4 seconds. The improvements of the reduced AlAs etching times are shown in Figure 5-4. This figure represents etching through 14 mirror periods as opposed to the 10 mirror pairs in Figure 5-3. Here the AlAs etch time has been reduced to 4 seconds and the undercut is now only 1.6 times the vertical etch depth. The

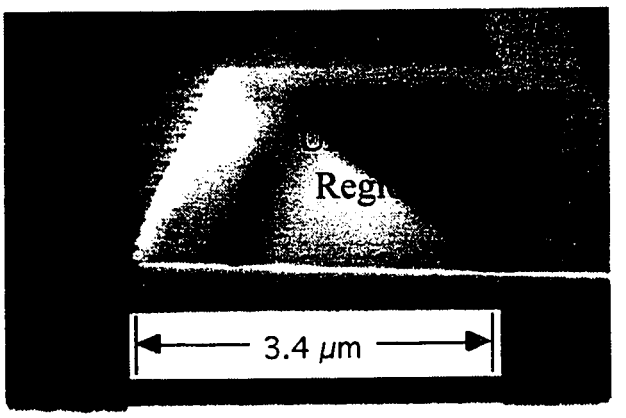

Figure 5-4: Cross-section SEM micrograph of 14 pairs of 680Å GaAs/810Å AlAs DBR mirror etched with the selective etching process. The GaAs layers were etched 12 seconds and AlAs layers 4 seconds.

sidewall profiles are characteristic of reaction rate limited etches.

In order to characterize the usefulness of this etch for intracavity contact VCSELs, a structure, Figure 5-5, consisting of 15 pairs of 810Å AlAs/680Å GaAs layers on a semi-insulating substrate was grown by molecular beam epitaxy. All layers were undoped except the top and bottom GaAs layers which were doped at $8x10^{18}$ cm^{-3} with Si. After growth, a sample (1/4 wafer) was cleaved and half of its surface protected with photoresist. The exposed region was etched through 14 mirror periods. At this point the advantages of the ultrasonic etching had not been realized, so the longer 11 second etching time was used for the AlAs layers. After etching, transmission line method (TLM) pads were simultaneously defined on both top (unetched) and bottom (etched) regions. N-type contacts were formed by alloying AuGe/Ni/Au metalization for 20 seconds at 400°C.

Ideally, both etched and unetched regions should be identical: 680Å of doped GaAs over 810Å of undoped AlAs. Five sets of contact pads were measured in each region and the results averaged to determine an average sheet resistance and specific contact resistance. The values along with standard deviations are shown in Table 5-1. The contacts on the GaAs layer exposed with the etching exhibited lower contact

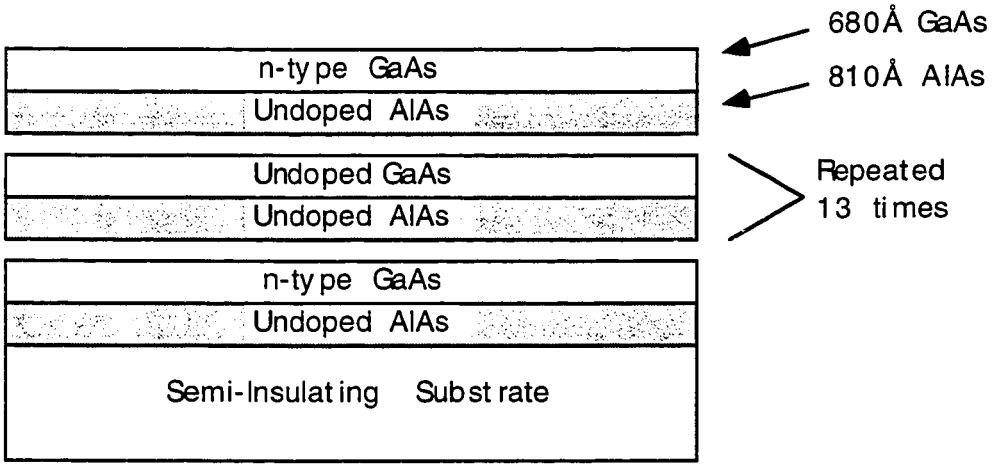

Figure 5-5: Schematic of structure to test contacting intracavity layer.

Table 5-1: Sheet resistance and specific contact resistance of contacts to etched and unetched regions of test sample.

Contact Set	Sheet Resistance	Specific Contact Resistance
Etched	171 ± 15 Ω/square	$1.4 \pm 0.5 \times 10^{-6}$ Ω-cm^2
Unetched	134 ± 10 Ω/square	$2.7 \pm 0.8 \times 10^{-6}$ Ω-cm^2

resistance and slightly higher sheet resistance than equivalent contacts on the surface layer.

The lower contact resistance might indicate that the etched layer, although appearing smooth and mirror-like under a microscope, might have increased roughness on a very small scale which increases the contact surface area. The increased sheet resistance, on the other hand, is probably due to slight etching of the GaAs contact layer reducing the cross-sectional conducting area. If the entire increase in sheet resistance is attributed to thinning of the contact layer, it would indicate overetching of only 100 Å, including surface depletion effects. This corresponds to an etch depth accuracy for the total 2.1 micron DBR mirror of 0.5%. In a real device, the contact layer would be at least three times thicker for mechanical stability and low series resistance, so the effects of this amount of overetching should have a small impact on device performance.

The overetching estimate of 100 Å corresponds to etching a GaAs layer for 7.5 seconds. This would indicate that the GaAs layer becomes exposed to the etchant only 3.5 seconds after the AlAs layer has started etching and while the brownish surface layer is still present. The numbers are consistent, however, with the etching under ultrasonic excitation where it took only 3-4 seconds to etch the AlAs layer and remove the brownish surface layer as well.

5.3 Current Confinement

Once contact is made to the intracavity layer, additional processing must be performed to limit the current injection in the active region to the area under the DBR mirror stack. Although this might be done simply with a self-aligned implantation using

the undoped top DBR mirror as a mask, as stated before, such an implantation can degrade device performance. An alternative method is to undercut a layer beneath the contact layer to physically confine the injected current.

An extremely selective etchant is needed so as not to destroy the contact layer in the process of undercutting it. Hydrofluoric acid/water and hydrochloric acid/water were examined as candidates to perform the undercut. Since these solutions do not contain an oxidizer (e.g. hydrogen peroxide), neither etches GaAs appreciably.[66] Both solutions, however, etch AlAs rapidly.[67,68]

Figure 5-6 shows a light emitting diode test structure for evaluating the undercut etchants and current confinement. First, an annular contact is deposited on the wafer with the lift-off technique. A photoresist mask is then used to protect the central region while the GaAs contact layer is etched to expose the AlAs undercut layer. The sample is then exposed to the undercut etchant. In order for the undercut to work properly, it is important not to leave the AlAs undercut layer exposed to air for long after the first etch is performed. The oxides that form on the sidewall can protect the AlAs layer and inhibit the undercut etch.

If the contact layer is relatively thin, the pillar of undercut AlAs can be examined with an optical microscope to estimate the undercut rate and the determine the smoothness of the undercut walls. Furthermore, the electroluminescence from the device can be used to determine if the undercut is indeed confining the current injection.

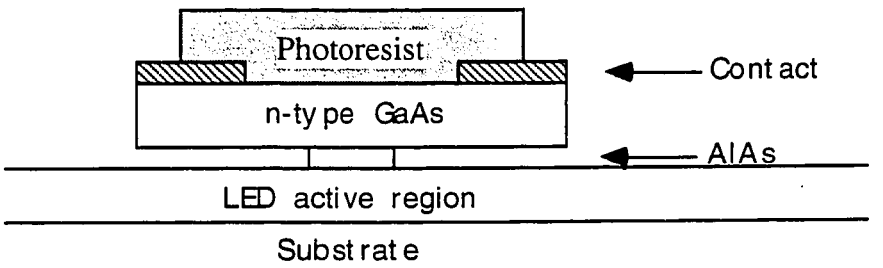

Figure 5-6: Schematic of undercut etch test structure

Hydrofluoric acid and water in concentrations from 2% to 10% were examined. This solution worked fine on test structures where no photoresist was left on the wafer from etching through the contact layer. When the photoresist was left on, however, the hydrofluoric acid etch produced very jagged edges on the undercut pillar. Hydrofluoric acid is known to attack photoresist and leave remnants on the surface of a sample after etching, so it is quite possible that some of this photoresist scum is protecting the sidewalls from undercutting. Since photoresist will be used to protect the AlAs in the top DBR mirror during the undercut process, another etchant was sought that would not have this problem.

Hydrochloric acid (38%) and water in a 1:5 ratio was also examined as an alternative undercut etchant. This etchant does not attack photoresist masks and produces undercut pillars with smooth sidewalls. Figure 5-7 shows optical micrographs looking down through two processed test devices. The darker region in the center of the annular contact is the pillar of AlAs that remains under the GaAs contact layer. The undercutting proceeds at different rates along different crystallographic planes. This can be seen as a gradual change from the square shape of the contact to an intermediate hexagonal and a final diamond shape. When the wafer is dried after etching, the released part of GaAs contact layer is pulled down by surface tension to lie flat on the layer below the undercut AlAs layer.

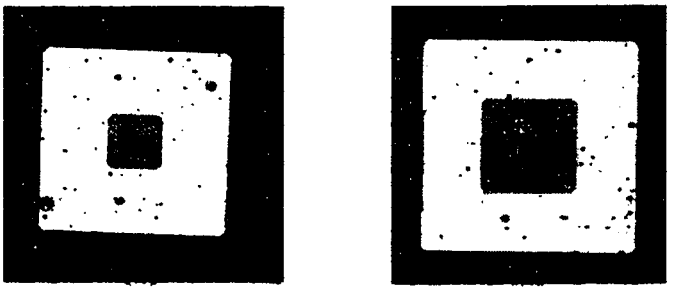

Figure 5-7: Optical micrographs of processed test devices. The hole in the annular contact is 8 microns square in (a) and 14 microns square in (b). The device on the right has been etched for a longer time.

Even with this physical contact, however, the undercut etch serves to confine injected current. Figure 5-8 shows an optical micrograph of a test device along with its electroluminescense captured with a CCD camera. The luminescence is slightly blurred because, without an aperture stop, it was not possible to have both the surface and active region in focus at the same time at this magnification on the microscope attached to the probe station. It is still clear that the current injection is being confined to the central region by the undercut of the AlAs layer.

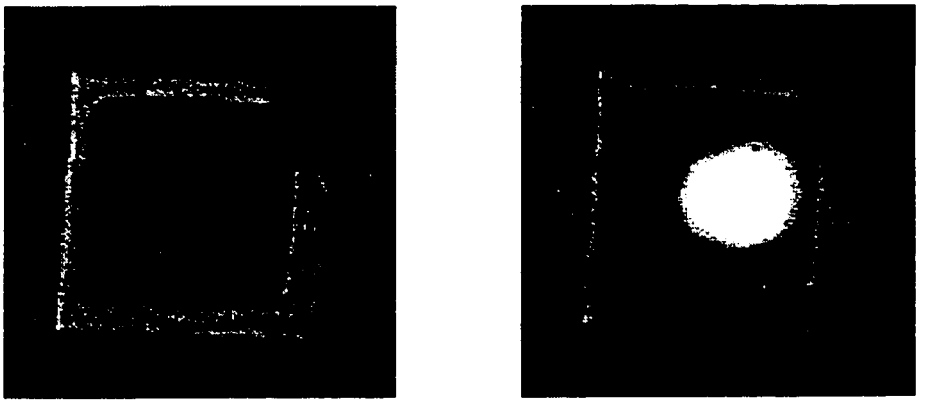

Figure 5-8: Infrared optical micrograph of a large test device. The opening in the annular contact is 100 microns on a side. The electroluminescense shows that current is confined to the central region by the undercut of the AlAs layer.

5.4 Analysis of Current Confinement Undercut

In order to be of use in VCSELs, the intracavity contact must provide a uniform, reliable, low resistance current path to the center of the active region. In an attempt to quantify these attributes, light emitting diodes (LEDs) identical to the proposed VCSELs except without the DBR mirrors were fabricated. Uniformity of I-V curves were evaluated as well as the current handling capacity of the contact structure. Three wafers were processed- two with n-type contact layers, 3/4 and 5/4 wavelengths thick, and one with a p-type contact layer 5/4 wavelengths thick- to study the effects of the contact layer thickness and type.

The structure for the test devices is shown in Figure 5-9. The n-type contact devices were grown on p-type substrates. A p+ GaAs buffer layer is followed by a p-type $Al_{0.3}Ga_{0.7}As$ layer doped at $1x10^{18}$ cm^{-3}, an undoped active region, and an n-type $Al_{0.3}Ga_{0.7}As$ layer doped at $1x10^{18}$ cm^{-3}. The doping in the AlAs undercut layer and GaAs contact layer is varied in an attempt to avoid large free carrier absorption while maintaining high lateral conductivity. The bottom half of the quarter wavelength AlAs layer is doped $2x10^{18}$ cm^{-3}. For the top half of this layer and first 1/8 wavelength of the contact layer, the doping is increased to $5x10^{18}$ cm^{-3}. Subsequent quarter wavelengths are doped alternately at $2x10^{18}$ cm^{-3} and $5x10^{18}$ cm^{-3} until the last 1/8 wavelength which is doped $6x10^{18}$ cm^{-3} in an effort to keep the contact resistance reasonably low. Because of the alloyed nature of the n-type contacts, the increased surface doping is probably not necessary for low contact resistance and should be avoided to lower free-carrier losses. The doping levels in the p-type contact wafer were the same, with inverse type, except for the top 1/8 wavelength of the contact layer which was doped $4x10^{19}$ cm^{-3}. The higher surface doping is necessary to reduce the contact resistance of the non-alloyed p-type contacts.

All layers were grown at 620° C thermocouple temperature except the active region which was grown at 520° C. Growth interruptions were performed before the first

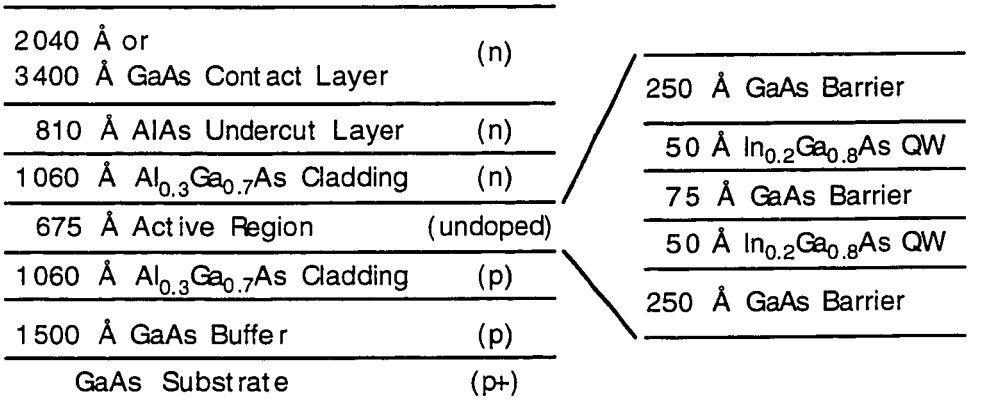

Figure 5-9: Layer structure for devices to test effects of contact layer thickness and type.

quantum well and 50 Å into the last barrier to change temperatures. Devices were processed using the process flow in appendix B, except that the mirror mesa definition step was not needed because the structures contain no DBR mirrors. For a given undercut time, the mesa defined by the annular contact determines the size and shape of the current confining AlAs pillar. Thus, by varying the extent of the contact as well size of the opening in it, the size of the AlAs pillar and the pillar to contact spacing can be varied independently.

The mask set has contact mesa squares varying from 20 to 34 microns on a side with square openings varying from 4 to 14 microns on a side. The 95 second undercut etch yielded approximately circular pillars, similar to that of Figure 5-7a, for the 26 micron contacts. Smaller pillars should be increasingly more diamond-like as in Figure 5-7b, while larger pillars should more closely resemble the original square contact mesas. Optical micrographs of typical completed devices are shown in Figure 5-10.

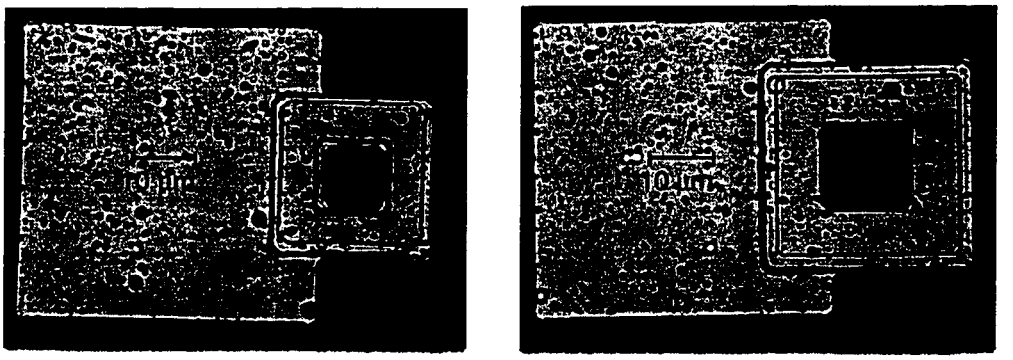

Figure 5-10: Devices to test intracavity contacts. Device (a) has a 26 micron contact mesa with 10 micron opening and device (b) has a 34 micron contact mesa with 14 micron opening.

5.4.1 Uniformity and Reliability

This analysis concentrates on devices with 10 micron square openings in a 26 micron contact mesa. As will be demonstrated later, the undercut etch produced an approximately circular AlAs pillar 9 microns in diameter centered in the 10 micron square opening in the annular contact. I-V curves were measured for twelve devices from the

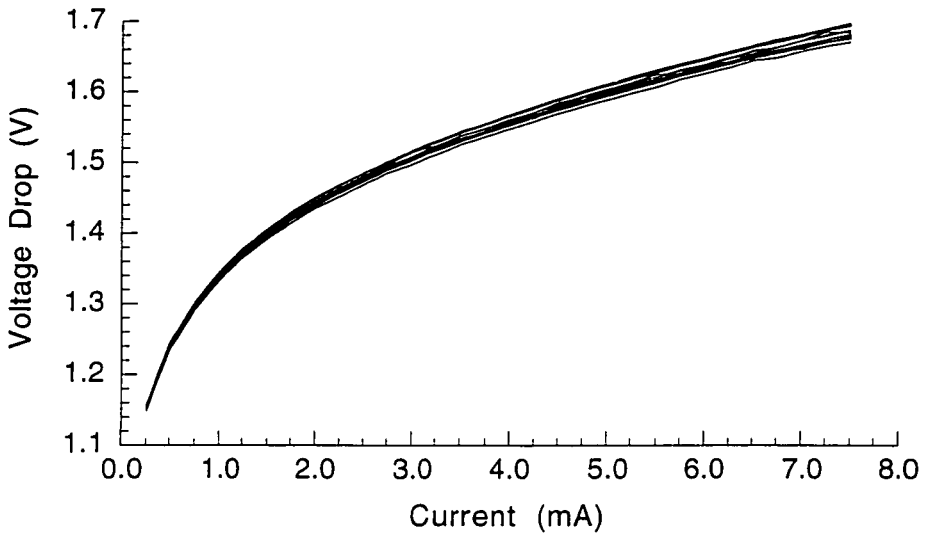

Figure 5-11: I-V curves of twelve devices- 26 micron contact mesas with 10 micron openings.

wafer with the 5/4 wavelength n-type contact layer and the results are shown in Figure 5-11.

The average and standard deviation of the voltage drop evaluated for several current densities of interest are shown in Table 5-2. The lowest two current densities correspond to conservative estimates of the threshold current densities broad-area and small devices, while the third is well above threshold for either case. It is clear that the current-voltage characteristics of the devices are very uniform, indicating a well controlled process. Furthermore, since these numbers include the metal / semiconductor contact resistance and more than 1.28 volts dropped across the active region, a PIN diode, this demonstrates that intracavity contact itself provides a very low-loss connection to the

Table 5-2: Voltage drop across test devices at selected current densities

Current Density (kA/cm^2)	Voltage Drop (V)
1.2	1.298 ± 0.003
3.1	1.442 ± 0.008
10.2	1.644 ± 0.007

active region.

An obvious concern for the reliability of this contact structure is its current handling capability. At high currents, one can imagine severe current crowding effects at the etched edge of the AlAs pillar leading to failure of the device. While device lifetime measurements were not performed, several devices were operated at excessive currents to determine a failure point and mechanism.

Figure 5-12 shows the high current failure of two devices with 10 micron openings in 26 micron contact mesas. The failure at just over 95 mA for both devices corresponds to a current density of over 150 kA/cm^2. This is an extremely high current density and one would expect a VCSEL to stop functioning long before reaching this point due to heating effects. As evidenced by the reduced voltage drop across failed devices and broader luminescent region, the failure mechanism seems to be a short from the GaAs contact layer directly to the AlGaAs cavity layer, bypassing the current constriction.

Visual inspection of a failed device with a larger contact opening, Figure 5-13,

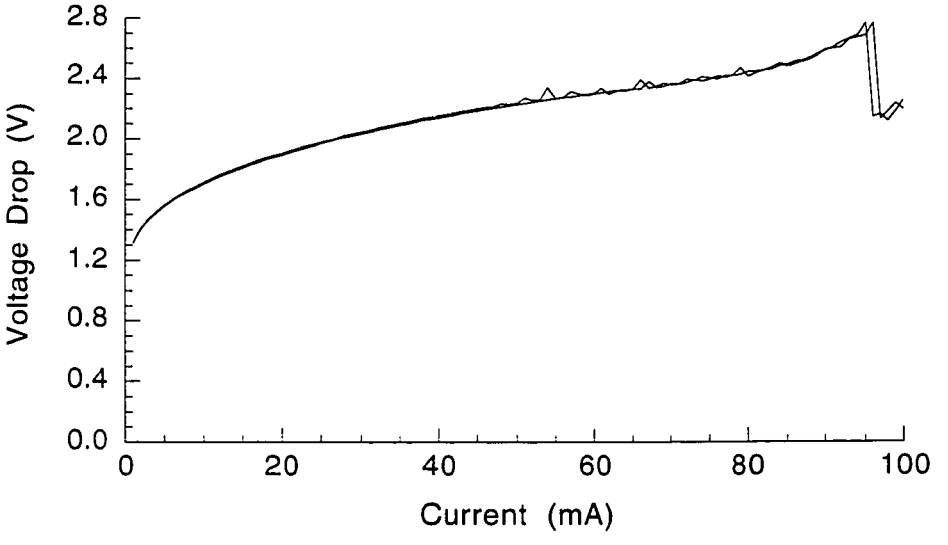

Figure 5-12: High current failure of 2 devices.

reveals an estimation of the AlAs pillar size. Assuming the visibly changed region is on the periphery of the AlAs current confinement pillar, where the current crowding is expected to be most severe, yields an estimate of 9 microns for the diameter of the AlAs pillar. This is consistent with estimates based on the luminescent region of working devices observed with a CCD camera.

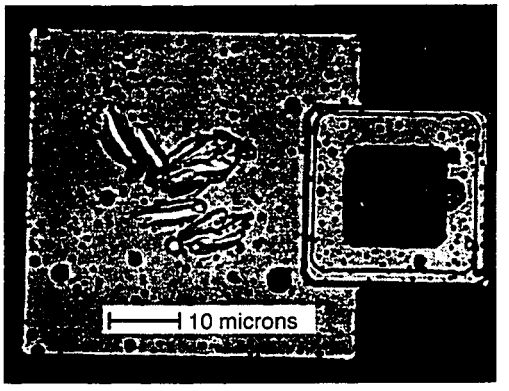

Figure 5-13: Optical micrograph (1000X) of a blown device with 26 micron contact mesa and 14 micron contact opening.

5.4.2 Effects of Contact Layer Thickness and Type

Although it seems clear that an n-type contact layer because of its lower contact resistance and higher mobility will prove superior to a p-type contact layer, both n- and p-type layers were grown to quantify this difference. In addition, both three-quarters and five-quarters wavelength n-type contact layers were evaluated.

Figure 5-14 shows the I-V characteristics for devices with 6 and 10 micron openings in 26 micron contacts. The unetched AlAs pillar is approximately 9 microns in diameter for all devices. The non-linearity of the curves can be attributed to the diode turn-on voltage, non-ohmicity of the contacts, and current crowding effects. The curves are linear at the higher currents shown indicating that the voltage drop is dominated by series resistance in this region. Linear fits of the region above 3 mA for the p-type contacts and 5 mA for the n-type contacts are shown in Table 5-3. For both contact dimensions, the differential series resistance of the p-type layer is five times that of the

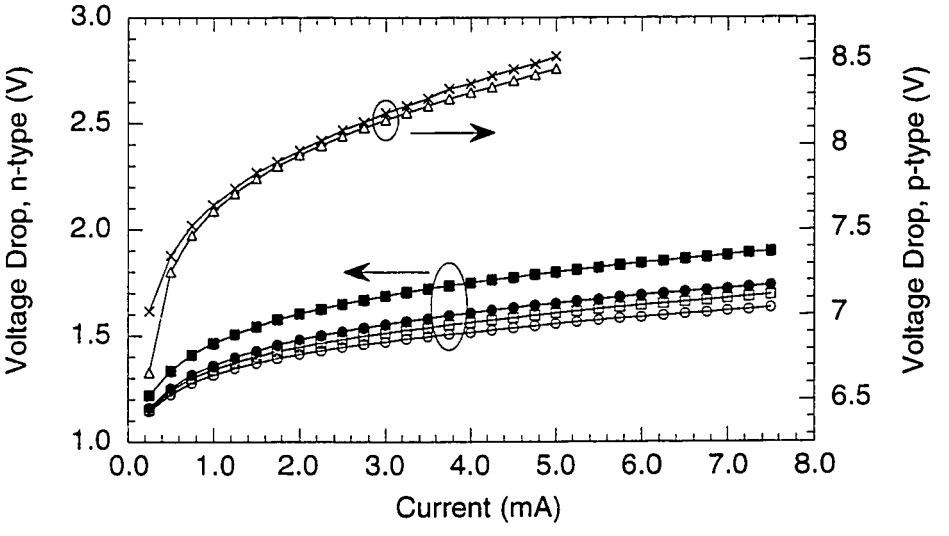

Figure 5-14: Current-voltage characteristics for devices with 6 and 10 μm contact openings above 9 μm AlAs conduction pillars. The solid symbols are for the 3/4 wavelength contact layer and the open ones are 5/4 wavelength contact layers. The circles and squares correspond to 6 and 10μm n-type devices while the triangles and "X's correspond to 6 and 10 micron p-type devices.

Table 5-3: Series resistance of selected intracavity contacts.

Contact Layer (Thickness:Type)	Contact Opening	Voltage Intercept	Slope
3/4 λ : n-type	6 μm	1.49 V	34 Ω
	10 μm	1.61 V	39 Ω
5/4 λ : n-type	6 μm	1.41 V	30 Ω
	10 μm	1.44 V	34 Ω
5/4 λ : p-type	6 μm	7.70 V	150 Ω
	10 μm	7.70 V	170 Ω

equivalently thick n-type layer. This is due in a large part to the factor of 16 between the mobilities of electrons and holes at doping levels used in these devices.[69] The large voltage drop across the p-type devices, as evident in the greater than 7 V intercept, is not explained by the larger series resistance however. Because the active regions should be virtually identical under the n- and p-type contacts, this increase must be caused by either non-ohmic metal-semiconductor contacts, current crowding, or barriers at the heterojunctions surrounding the AlAs current confinement layer. Since the barriers will both be less than the valence band discontinuity (~0.6 eV) and the voltage intercept is independent of the overlap between the contact and the AlAs current confinement pillar, the most likely culprit is non-ohmicity of the non-alloyed contacts.

As expected, the n-type layers are much more suitable for intracavity contact layers. The 10 micron case is of most interest for real VCSELs because the contact opening, and thus the top mirror, is slightly larger than the current confinement region. The equivalent series resistivities, 2.5×10^{-5} Ω-cm^2 for the 3/4 wavelength layer and 2.2×10^{-5} Ω-cm^2 for the 5/4 wavelength contact layer, are only slightly larger than those expected for full p-type mirrors based on the design presented in section 4.3.

Observing how the device characteristics change as the lateral current path gets longer can give an indication of the relative effects of vertical and lateral conduction through the contact layer. Figure 5-15 shows I-V curves for devices on the 26 micron mesas as a function of the lateral spacing between the contact edge and edge of the current

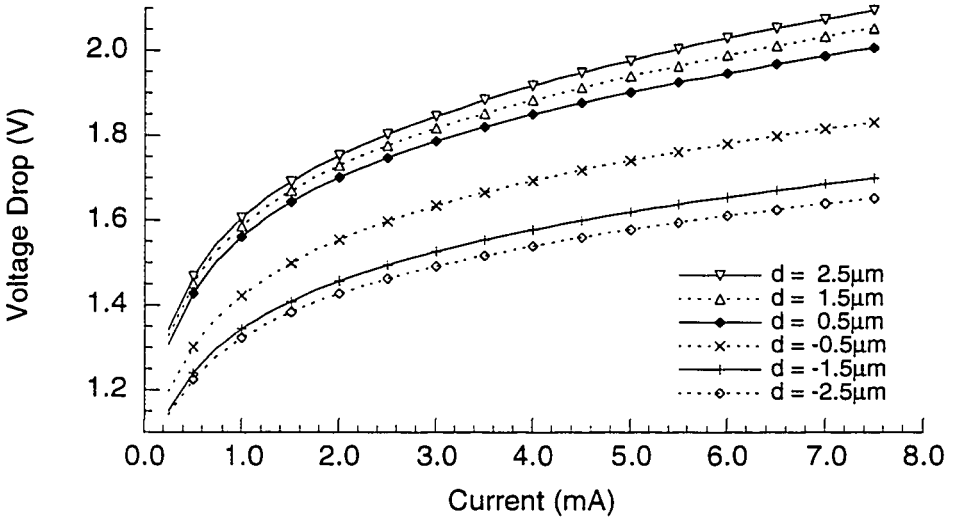

(a)

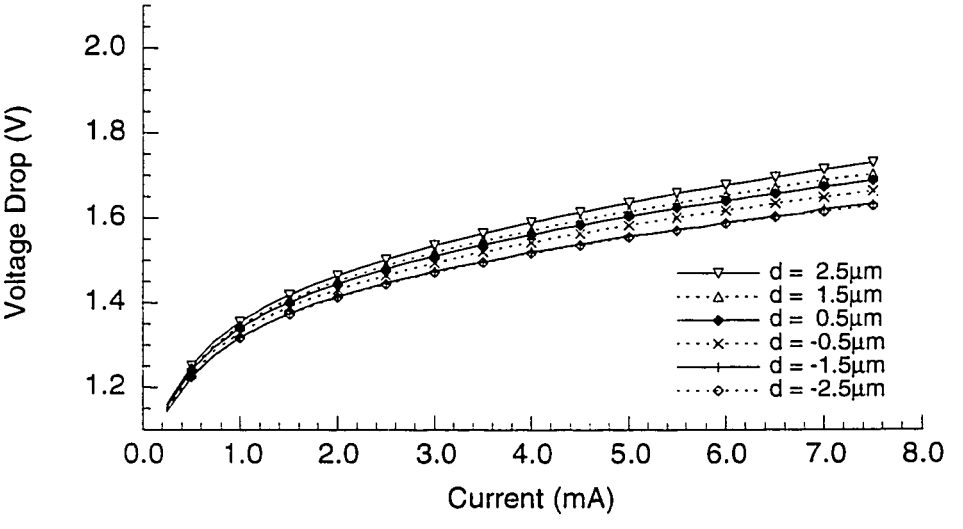

(b)

Figure 5-15: Current-voltage curves for devices with (a) 3/4 wavelength and (b) 5/4 wavelength n-type contact layers as a function of the spacing between the edges of the contact and current-confinement AlAs pillar.

confinement pillar of AlAs. The dimensions are illustrated in Figure 5-16. A negative value for the spacing, d, indicates that the contact overlaps the AlAs pillar and device active region. Because the contact opening is square and the current confinement pillar is roughly circular, there is only partial overlap in the d = -0.5 μm case.

At the largest overlap, the current conduction is primarily vertical and there is very little dependence on the layer thickness. As the overlap is decreased, however, the two samples show markedly different behavior. For the sample with the thinner contact layer, there is a slight increase in voltage drop even while there is significant overlap and an abrupt increase as soon as there is even partial lateral separation. This abrupt increase could be due to the onset of significant current crowding effects. At larger separations, the voltage drop increase is smaller- that which would be expected due to the increased path length for lateral current conduction through the contact layer.

The thicker contact layer, on the other hand, is much less effected by the crossover from vertical to lateral current conduction. There is no increase in voltage drop at all while there is significant overlap. As the separation begins, rather than an abrupt increase, there is a much smaller, smoother voltage drop increase due to the increased length of the current path. This seems to indicate that the layer is thick enough to

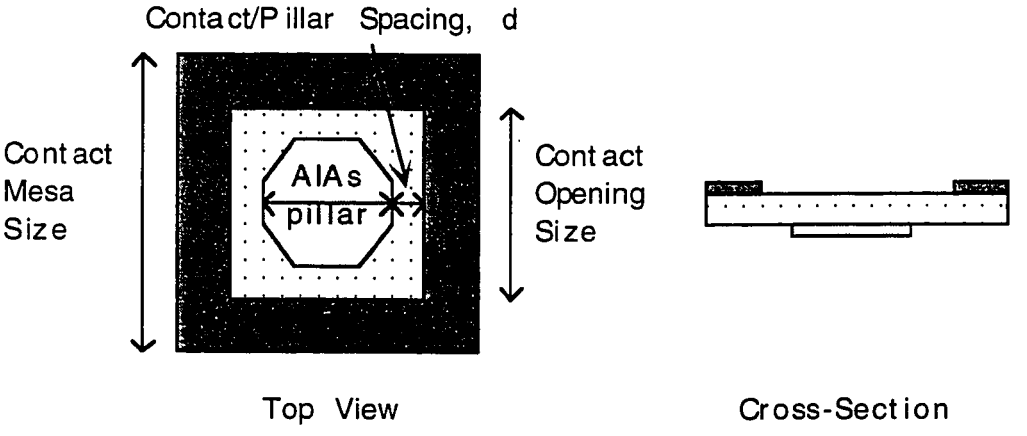

Figure 5-16: Dimensions of intracavity contact test devices.

efficiently transport current from the contact to the current confinement region.

Because the contact layer is doped and will lead to some free-carrier absorption, one wants to use the thinnest layer possible consistent with small ohmic losses.[70] The comparisons in Figure 5-15 indicate that a 5/4 wavelength contact should be the ideal contact layer thickness for the doping levels used in these test devices.

6. Conclusion

6.1 Summary

This thesis has demonstrated improvements in the growth, mirror design, and processing toward realizing high-efficiency vertical-cavity surface-emitting lasers. Specifically, a growth correction technique has been developed which enables the operating wavelength of the VCSELs, determined by the epitaxial layer thicknesses, to be positioned accurately so that it coincides with the peak of the material gain at the operating point. Ensuring higher material gain at the lasing wavelength increases the optimum output coupling and thus, with proper designs, enables one to optimize the efficiency of a design. Additionally, two improvements were made to lower the electrical losses experienced by these lasers. Since these approaches do not require high free-carrier levels in regions with high optical intensity, they should decrease the voltage necessary to achieve a given output power, increasing the wallplug efficiency.

The first electrical improvement was the demonstration of very low resistivity p-type MBE grown distributed Bragg reflectors. The use of a p-n doping dipole at each interface allows the valence band variations to be flattened with a relatively short compositional grading region at the interface. With the improved doping profile discussed in section 4.3.4, this design should allow the fabrication of DBR mirrors which offer better performance- lower resistance and optical absorption for a given reflectivity- than the best results published in the literature.

The second improvement involves processing for achieving a very low resistance n-type intracavity contact to the VCSEL. A selective etching technique was demonstrated which enables the intracavity layer to be contacted reliably and an undercut process was developed for lateral confinement of the injected current. Measurements

made on test devices illustrate that a five-quarters wavelength n-type contact layer should provide a low resistance current path to the central area of the active region.

The combination of these two improvements should enable lasers to be fabricated with very low operating voltages, even in designs with higher output coupling. The last point is important because it differentiates lasers optimized for extremely low threshold current from those optimized for high-efficiency operation. The former can have low threshold voltages because little current flows, but generally have poor differential and wallplug efficiency because the low output coupling limits the output power.

From the test devices measured in this work, one can make an estimate of the voltage drops which can be expected from VCSELs based on these designs. Even assuming a threshold current density of 3 kA/cm^2, one would expect 1.44 volts to be dropped across the active region and n-type intracavity contact and 0.05 volts to be dropped across the bottom p-type DBR mirror leading to a threshold voltage of 1.5 volts. It is difficult to estimate the maximum wallplug efficiency that could be achieved with such a design without measurements on working devices; however, it is not unrealistic to assume that a threshold current density of under $1kA/cm^2$ is obtainable with a differential quantum efficiency of 70%. When operated at 3 times threshold , such a laser based on this design would have over 40% wallplug efficiency.

6.2 Future Work

Although the improvements presented in this work will increase the efficiency of lasers in which they are incorporated by lowering losses, measurements on working devices are needed to optimize the design. It is necessary to know the peak material gain and optical losses, including scattering and diffraction, as well as the free-carrier losses examined here, to determine the optimum output coupling for the top DBR mirror and optimum number of quantum wells in the active region. Conceivably one could grow a structure with extra mirror pairs and etch back the top DBR mirror to determine the optimum coupling. The selective etching technique from section 5.2 would be useful for

this purpose, however, one would probably want to use a more selective etchant for the AlAs layers (such as $HCl:H_2O$) to insure an abrupt stop each mirror period. Measurement of the slope efficiency and optimum output coupling at different injection levels could then be used to determine the optical loss and material gain for the laser.

The fabrication of the intracavity contact could potentially be improved as well. Recent work into oxidation of AlAs layers[71,72] has shown promise as an alternative method for achieving efficient current confinement without either etching or implantation. This oxidation process converts AlAs into a stable, transparent, and electrically insulating material.[73] MacDougal, et al.,[74] demonstrated that the oxidized AlAs could also be utilized for the low index layer of a distributed Bragg reflector mirror. With indices of 1.6 for oxidized AlAs and 3.5 for GaAs, very high reflectivity mirrors could be fabricated with only four mirror pairs. One could combine these two uses to create a simple and elegant extension to the VCSEL design presented in this thesis.

During the current confinement step of the process, the oxidation would be used instead of undercut etching. If, additionally, the top DBR mirror is left unprotected during this step, the AlAs mirror layers will be oxidized at the same time as the confinement layer. By providing a wider contact mesa the oxidation time could be adjusted so that the AlAs mirror layers are completely oxidized, while a conduction path still remains in the current confinement layer. Such a device is illustrated in Figure 6-1. Because the index of the oxidized material is only 1.6, very high reflectivity GaAs/AlAs-oxide mirrors can be formed with as few as four mirror pairs. Such a DBR mirror would have the additional advantages of lower phase dispersion, lower optical penetration, higher bandwidth, shorter growth time, easier fabrication, and potentially improved reliability.

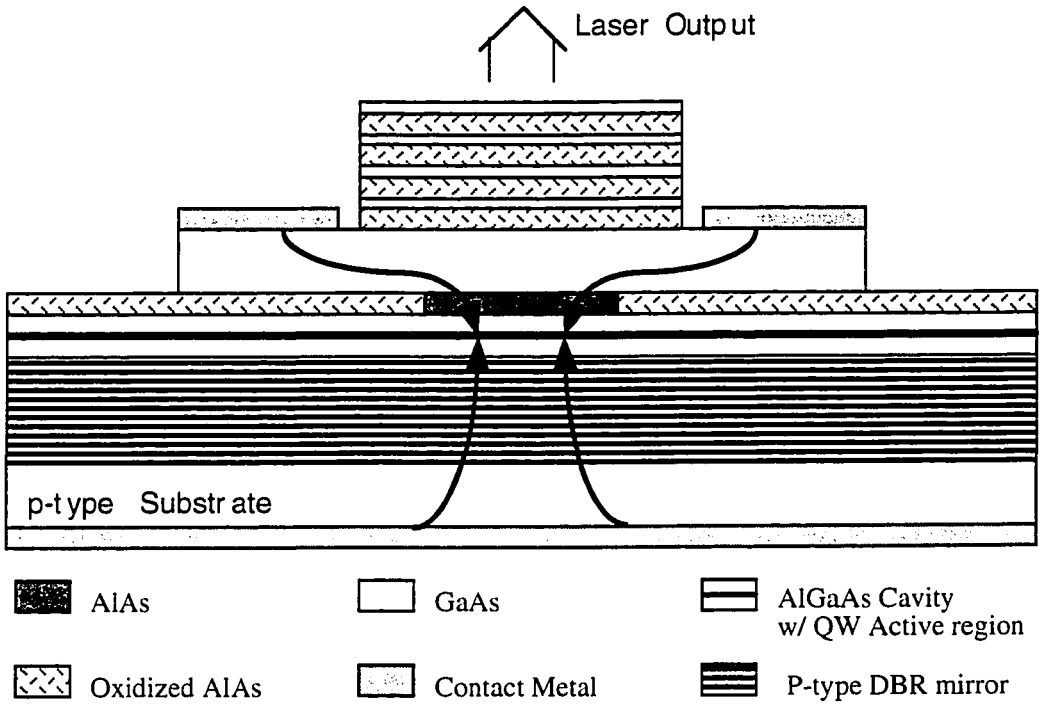

Figure 6-1: Schematic of VCSEL design using oxidized AlAs.

Appendix A: In-Situ Reflectivity Measurements

Reflectivity measurements can be of great use in general to Molecular Beam Epitaxy (MBE) in addition to their specific application to the growth correction of vertical cavity optical devices. In particular, through the index of refraction, measurement of the wafer reflectivity can be used to determine layer thicknesses and absorption spectra which, in turn, can be used to determine growth rates, spectral position of quantum wells optical properties, and substrate temperature. The following sections will examine these uses for in-situ reflectivity measurements.

Thickness Measurement (System Calibration)

Initial calibration of an MBE system involves measuring the factor that relates Beam Equivalent Pressure (BEP) to growth rate. This factor is dependent on geometrical factors in addition to the material properties of the species being measured and so must be performed each time the sources are loaded or the substrate position is altered (e.g. because the positioner is removed from the machine during bake-out). After calibration, a BEP measurement, which is easily performed with an ionization gauge in the substrate position, can be used before each growth run to determine growth rates.

Traditionally, the initial calibration is performed by measuring growth rates with Reflection High-Energy Electron Diffraction (RHEED) oscillations. Although this technique yields an extremely accurate measurement of the growth rate, [16] in practice, its incompatibility with substrate rotation limits its effectiveness.[75] In particular, the measurement can usually only be performed during the initial 10 or 20 monolayers of a layer's growth when shutter transients cause the growth rate to be momentarily higher.

Reflectivity measurements, by contrast, are applicable to much thicker layers and thus give a more accurate picture of the average growth rate. Using index of refraction

data and the position of Fabry-Perot nodes in the reflectivity spectrum, the thickness of a layer can be determined to the accuracy of the index data.

The aluminum sources are most easily calibrated. A one micron thick layer of AlAs is grown on a GaAs substrate and a reflectivity spectrum is taken in-situ. The in-situ measurement is necessary because the rapid oxidation of AlAs in the atmosphere would affect the measurement. Looking at wavelengths where the substrate is absorbing, less than 870 nm, one has a simple three layer, GaAs/AlAs/vacuum, problem. Figure A-1 shows a typical reflectivity spectrum for a nominally one micron thick AlAs layer on GaAs. The refractive index of AlAs at the nodes is taken to be 3.116 @ 637 nm, 3.064 @ 700 nm, and 3.018 @ 782 nm from Adachi.[22] A reflectivity simulation (section 3.1) using these values fits all three node to within 1 nanometer assuming an actual thickness of 0.963 microns. Given the 2.15 hour growth time for the layer, a growth rate of 0.448

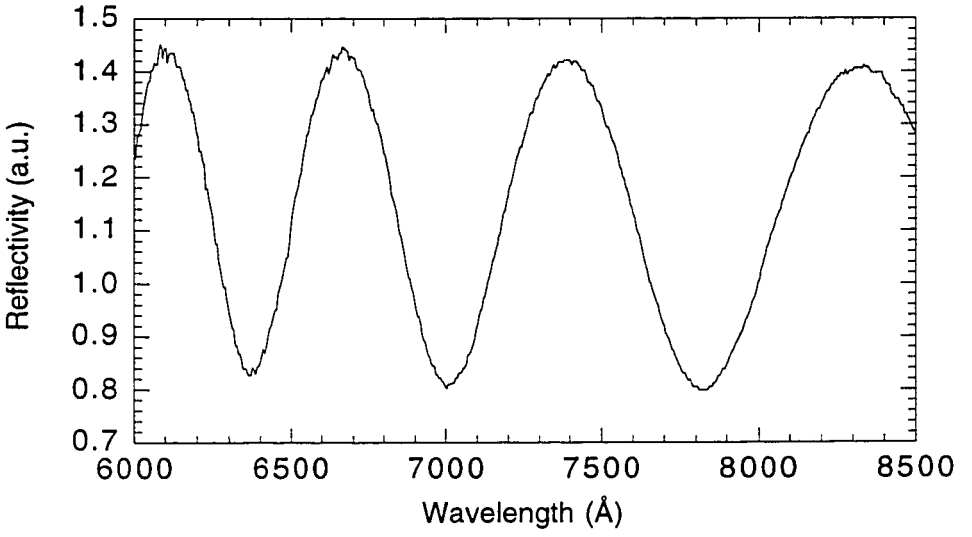

Figure A-1: In-situ reflectivity spectrum of 1 micron thick AlAs layer on GaAs substrate. The reflectivity has been normalized by dividing out the reflectivity of a bare GaAs substrate.

microns/hour is determined.

To calibrate a gallium source a thick GaAs layer is grown over a thin AlAs layer on a GaAs substrate. The AlAs layer is needed to provide a reflection from the back side of the calibration layer. If the aluminum calibration has just been performed, one expects the AlAs layer thickness to be very accurate. Because more accurate refractive index information is available for GaAs below the band edge, reflectivity data for wavelengths longer than about 900 nm is used. Figure A-2, shows a typical reflectivity spectrum from a nominally 0.711 μm thick GaAs layer over 847 Å of AlAs layer on a GaAs substrate. These thicknesses are chosen so as to produce a reflectivity node at 1 μm if all layers are accurate. The refractive indices of GaAs and AlAs at the reflectivity nodes are taken to be 3.591 and 2.976 at 904 nm and 3.497 and 2.945 at 1047 nm. Both nodes are fit to within 1 nm for an assumed GaAs layer thickness of 0.751 μm.

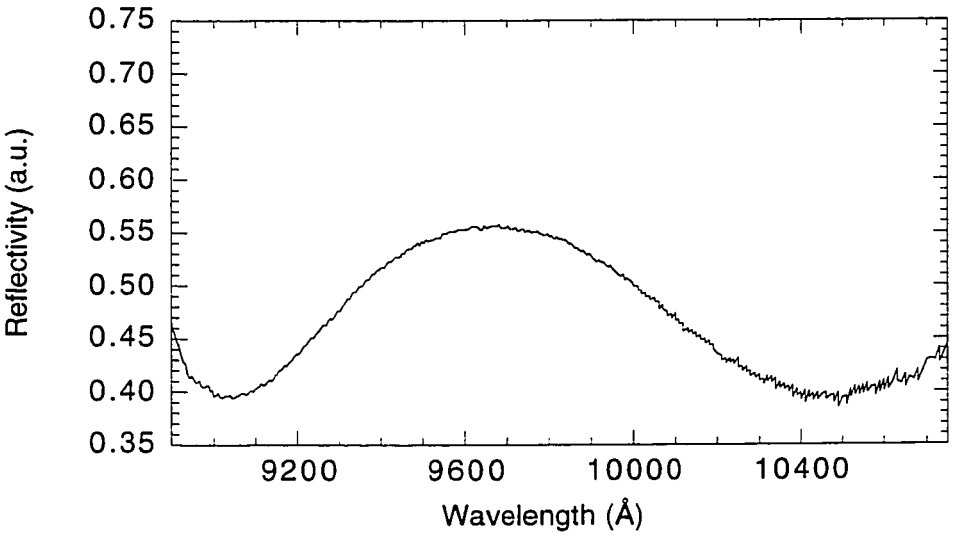

Figure A-2: In-situ reflectivity of a nominally 0.7 micron GaAs layer over 847 Å of AlAs on a GaAs substrate. The spectrum has been normalized by dividing out the measured reflectivity of a bare GaAs wafer.

For optical devices, where optical length, index of refraction times physical length, is more important than physical thickness, optical calibrations have the advantage of measuring the more important parameter directly. Using in-situ reflectivity to calibrate our systems and automated BEP measurements just before growth, we typically see less than 1% deviation from target wavelengths for DBR mirror stacks.

Calibration of the indium source is generally not accomplished with this method because of the large mismatch between the lattice constants of GaAs and InAs. Instead, a thick, approximately 0.5 micron, relaxed layer of $In_yGa_{1-y}As$ ($y \sim 0.5$) is grown once the gallium source is calibrated. From a measurement of the lattice constant by X-ray diffraction, the composition, y, can be accurately determined. Since the GaAs growth rate is known from the optical calibration, the InAs growth rate can then be calculated.

Absorption Measurements

Since refractive index changes between materials in the GaAs/AlAs/InGaAs

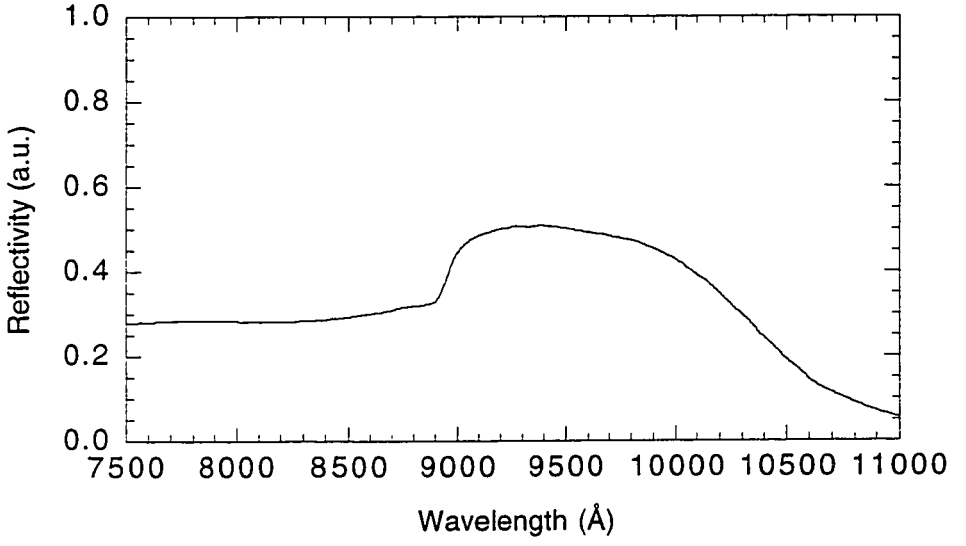

Figure A-3: Reflectivity spectrum of a bare GaAs wafer.

material system are relatively small (~0.5) compared with that between semiconductor and vacuum (~2.5), in the absence of coherent interference effects, the dominant reflections will be from the front and back surface of the wafer. As a result, the absorption properties of the substrate and epi layers can often be seen as a modulation of the light reflected from the back surface of the wafer. Figure A-3 shows the reflectivity spectrum of a bare GaAs wafer at room temperature. Above the bandgap of GaAs, wavelengths less than 870 nm, one only sees the 30% reflection from the front surface of the wafer. At the band-edge, however, the reflectivity increases due to light transmitted through the substrate and reflected off the back surface. The signal decreases at long wavelengths do to the reduced efficiency of the Si detector.

Since the bandgap varies with temperature, a measurement of the absorption edge can therefore be correlated with the substrate temperature.[76,77] Figure A-4, shows reflectivity spectra at different thermocouple substrate temperatures clearly showing this

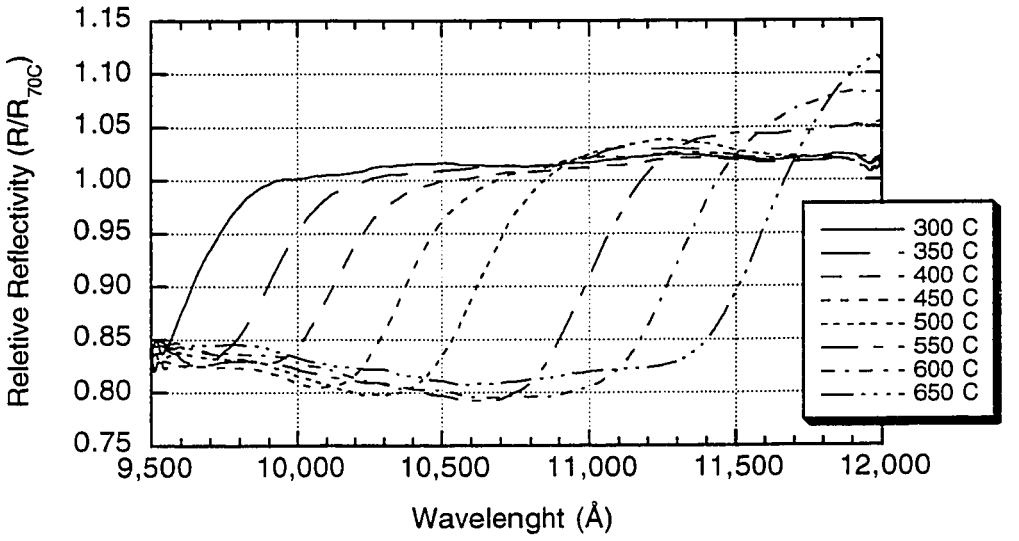

Figure A-4: Normalized reflectivity spectra at different substrate thermocouple temperatures.

effect. These spectra were taken with an InGaAs detector, enabling the measurement at the longer wavelengths. At substrate temperatures of 550°C and higher, one starts to see additional signal due to transmission through the substrate from the substrate heater's radiation. Since this light is transmitted through the substrate as well, its spectrum also carries the substrate absorption information.

The reflectivity spectrum at wavelengths longer than the substrate absorption edge can be used to examine the absorption properties of epitaxial layers. In particular, the absorption from InGaAs quantum wells can measured and used to estimate the spectral position of the emission from such wells. Figure A-5, shows the reflectivity spectrum of ten $In_{0.2}Ga_{0.8}As$ quantum wells separated by 150Å GaAs barriers. The absorption peak at 954 nm is clearly seen as a reduction in the light reflected from the back surface of the substrate.

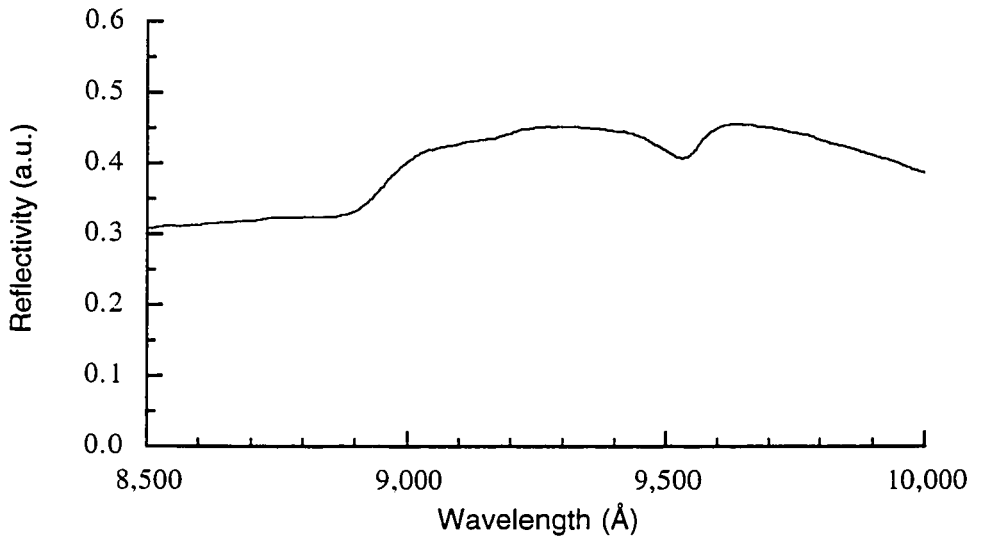

Figure A-5: Reflectivity from ten InGaAs quantum wells with GaAs barriers on a GaAs substrate.

Appendix B: Process Flow for Intracavity Contact VCSELs

A process flow for realizing intracavity contact VCSEL was developed consisting of mesa definition, top-side contact, current confinement undercut, and back-side contact:

Mirror Mesa Definition (top-emitting lasers)

- Prebake wafer in 120°C oven for 30 minutes
- Spin on AZ1813 photoresist at 5000 rpm for 30 seconds
- Remove photoresist from back side of wafer
- Bake in 88°C oven for 20-30 minutes
- Expose photoresist though Mask 1, MESA.
- Develop
- Postbake in 88°C oven for 10 minutes
- Etch through top mirror to contact layer using selective etching technique (see section 5.2).
- Remove photoresist with acetone followed by methanol. Blow dry.

Mirror Mesa Definition (bottom-emitting lasers)

- Prebake wafer in 120°C oven for 30 minutes.
- Spin on AZ1813 photoresist at 3500 rpm for 30 seconds.
- Remove photoresist from back side of wafer.
- Bake in 88°C oven for 20-30 minutes.
- Soak in chlorobenzine for 10-15 minutes.

- Bake in 88°C oven for 5 minutes.
- Expose photoresist through Mask 2, MESALIFT.
- Develop.
- Postbake in 88°C oven for 10 minutes.
- Evaporate Au or Ti/Au for reflector and mesa definition.
- Liftoff.
- Etch through top mirror to contact layer using selective etching technique (see section 5.2).
- Remove photoresist with acetone followed by methanol. Blow dry.

Top Contact

- Prebake wafer in 120°C oven for 30 minutes.
- Spin on AZ1813 photoresist at 3500 rpm for 30 seconds.
- Remove photoresist from back side of wafer.
- Bake in 88°C oven for 20-30 minutes.
- Soak in chlorobenzine for 10-15 minutes.
- Bake in 88°C oven for 5 minutes.
- Expose photoresist through Mask Level 3, CONTACT.
- Develop.
- Postbake in 88°C oven for 10 minutes.
- Dip in 1:1 $HCl:H_2O$ for 10 seconds to remove oxide.

- Blow dry and wipe back side.
- Evaporate AuGe/Ni/Au 350Å/150Å/1500Å contacts.
- Liftoff. Rinse acetone with methanol and blow dry.
- Anneal contacts in RTA using KEN405.RCP (405°C for 20 seconds).

Current-Confinement Undercut

- Prebake in 120°C oven for 30 minutes.
- Spin on AZ1813 photoresist at 3500 rpm for 30 seconds.
- Bake in 88°C oven for 20-30 minutes.
- Expose photoresist using Mask Level 4, PROTECT.
- Develop.
- Postbake in 88°C oven for 15 minutes (important).
- Etch through contact layer and undercut layer using either

  1:1:10 H_2SO_4:H_2O_2:H_2O (easiest), or

  Selective etches for mirror etch.
- Immediately after rinsing perform undercut with 1:5 HCl:H_2O

  The undercut proceeds at 5.4 microns/minute to greater than 6.5 microns/minute depending on the crystallographic alignment of the features.
- Remove photoresist with acetone followed by methanol. Blow dry.

Oxide and Vias

- Deposit 2000Å thick oxide on sample with Plasma Enhanced Chemical Vapor Deposition (PECVD).

- Prebake in 120°C oven for 30 minutes.
- Spin on AZ1813 photoresist at 5000 rpm for 30 seconds.
- Bake in 88°C oven for 20-30 minutes.
- Expose photoresist using Mask Level 5, VIA.
- Develop.
- Postbake in 88°C oven for 10 minutes.
- Etch via holes in oxide with RIE: 100 sccm CHF_3, 10 sccm O_2, 100 mTorr, 100 watts, 10 minutes.
- Remove polymerized photoresist in RIE: 20 sccm O_2, 100 mTorr, 50 watts, 90 seconds.
- Remove photoresist with acetone followed by methanol. Blow dry.

Top Metalization Pads

- Prebake in 120°C oven for 30 minutes.
- Spin on AZ1813 photoresist at 3500 rpm for 30 seconds.
- Bake in 88°C oven for 20-30 minutes.
- Expose photoresist using Mask Level 6, METAL.
- Develop.
- Postbake in 88°C oven for 10 minutes.
- Dip in 1:1 $HCl:H_2O$ for 10 seconds to remove surface oxide.
- Blow dry and wipe back side.
- Evaporate Ti/Au 350Å/3000Å metalization.

- Liftoff. Rinse acetone with methanol and blow dry.

Back Side Contact

- Heat Ti/Au covered glass slide to 170+°C.
- Place small ball of indium on the slide and push down lightly with wafer when melted. Be careful not to block lasers for bottom-emitting design.

References

[1] Motorola has announced plans to market a 10-line optical bus based on VCSEL/fiber-optic technology later this year.

[2] A. Siegman, *Lasers* (Mill Valley, California: University Science Books, 1986), pp. 400-1.

[3] J.T. Verdeyen, *Laser Electronics* (Englewood Cliffs, New Jersey: Prentice-Hall, Inc., 1981), pp. 287-92.

[4] A. Nussbaum and R. Phillips, *Contemporary Optics for Scientists and Engineers*, (Englewood Cliffs, New Jersey: Prentice-Hall, 1976) pp.1 182.

[5] see section 3.1.

[6] H. A. MacLeod, *This Film Optical Filters* (New York, New York: Macmillan, 1986), p. 167-170.

[7] see section 3.1.2 for the derivation leading to equation (3-39).

[8] H.C. Casey and M.B. Panish, Jr. , *Heterostructure Lasers, Part A: Fundamental Principles*, (San Diego, California: Academic Press, 1978), pp. 175.

[9] R.S. Geels, S.W. Corzine, and L.A. Coldren, "InGaAs Vertical-Cavity Surface-Emitting Lasers," IEEE Photonics Technology Letters, Vol. 26, No. 6, pp. 1359-67, 1991.

[10] A. Siegman, *Lasers* (Mill Valley, California: University Science Books, 1986), pp. 428-29.

[11] ibid, pp. 479.

[12] Z.R. Wasilewski, G.C.Aers, A.J. SpringThorpe, and C.G. Miner, Growth uniformity studies in molecular beam epitaxy," Journal of Crystal Growth, Vol. 111, pp. 70-4, 1991.

[13] J.P.A. van der Wagt, K.L. Bacher, G.S. Solomon, and J.S. Harris, Jr., "Geometrical growth rate nonuniformity effects on reflection high-energy electron signal intensity decay," Journal of Vacuum Science Technology B, Vol. 10, No. 2, pp. 925-8, 1992.

[14] O.D. Patterson, J.J. Heyob, S.J. Adams, V. Hunt, P.H. Garrett, K.R. Currie, K.G. Eyink, T.W. Haas, S.R. Leclair, "Progress toward a comprehensive control system for molecular beam epitaxy," Wright Laboratory Materials Directorate Interim Report, pp 4-7, Aug 1992.

[15] J.L. Jewell, J.P. Harbison, A. Scherer, Y.H. Lee, and L.T. Florez, "Vertical-Cavity Surface-Emitting Lasers: Design, Growth, Fabrication, Characterization," IEEE Journal of Quantum Electronics, Vol. 27, No. 6, pp. 1332-46, 1991.

[16] J.H. Neave and B.A. Joyce, "Dynamics of Film Growth of GaAs by MBE from RHEED Observations," Applied Physicas A, Vol. 31, pp. 1-8, 1983.

[17] See the section on thickness measurements in Appendix A.

[18] J.L. Jewell, J.P. Harbison, A. Scherer, Y.H. Lee, and L.T. Florez, "Vertical-Cavity Surface-Emitting Lasers: Design, Growth, Fabrication, Characterization," IEEE Journal of Quantum Electronics, Vol. 27, No. 6, pp. 1332-46, 1991.

[19] D.B. Young, J.W. Scott, F.H. Peters, B.J. Thibeault, S.W. Corzine, M.G. Peters, S.-L. Lee, L. A. Coldren, "High-Power Temerature-Insensitive Gain-Offset InGaAs/GaAs Vertical-Cavity Surface-Emitting Lasers," IEEE Photonics Technology Letters, Vol. 5, No. 2, pp. 129-32, 1993.

[20] H. A. MacLeod, *This Film Optical Filters* (New York, New York: Macmillan, 1986), p. 17-40.

[21] An arbitrary input polarization can be decomposed into TE and TM components which are then treated seperately.

[22] S. Adachi, "GaAs, AlAs, and $Al_xGa_{1-x}As$: Materials parameters for use in research and device applications," Journal of Applied Physics, Vol. 58, No. 3, pp. R1-R29, 1985.

[23] H.C. Casey and M.B. Panish, Jr. , "Heterostructure Lasers, Part A: Fundamental Principles," (San Diego, California: Academic Press, 1978), pp. 44.

[24] S.A. Chalmers, K.L. Lear, and K.P. Killeen, "Low resistance wavelength-reproducible p-type (Al,Ga)As distributed Bragg reflectors grown by molecular beam epitaxy," Applied Physics Letters, Vol. 62, No. 14, pp. 1585-7, 1993.

[25] H. A. MacLeod, *This Film Optical Filters* (New York, New York: Macmillan, 1986), p. 32-40.

[26] A.E. Siegman, *Lasers* (Mill Valley, California: University Science Books, 1986), p. 413-23.

[27] K. Bacher, B. Pezeshki, S. Lord, and J.S. Harris, "Molecular beam epitaxy growth of vertical cavity optical devices with in-situ corrections," Applied Physics Letters, Vol. 61, No. 12, pp. 1387-9, 1992.

[28] See appendix A.

[29] L.E. Eng, K. Toh, K. Bacher, J.S. Harris, and C.J. Chang-Hasnain, "Periodic Mode-Shift in Vertical Cavities Grown by Molecular Beam Epitaxy," IEEE Photonics Technology Letters, Vol. 7, No. 3, pp. 235-7, 1995.

[30] R, Fischer, J. Klem, T.J. Drummond, R.E. Thorne, W. Kopp, H. Morkoç, and A.Y. Cho, "Incorporation rates of gallium and aluminum on GaAs during molecular beam epitaxy substrate temperatures," Journal of Applied Physics, Vol. 54, No. 5, pp. 2508-10, 1983.

[31] R.S. Geels, S.W. Corzine, J.W. Scott, D.B. Young, and L.A. Coldren, "Low Threshold Planarized Vertical-CAvity Surface-Emitting Lasers," IEEE Photonics Technology Letters, Vol. 2, No. 4, pp. 234-6, 1990.

[32] M.G. Peters, F.H. Peters, D.B. Young, J.W. Scott, B.J. Thibeault, and L.A. Coldren, "High Wallplug Efficiency Vertical-Cavity Surface-Emitting Laser Using Lower Barrier DBR Mirrors," Electronics Letters, Vol. 29, No. 2, 170-2, 1993.

[33] K.L. Lear, S.A. Chalmers and K.P. Killeen, "Low Threshold Voltage Vertical Cavity Surface-Emitting Laser," Electronics Letters, Vol. 29, No. 7, pp. 584-6, 1993.

[34] The shift in the electroluminescence spectra which is similarly related to the bandgap energy was measured from 15 °C to 95 °C to determine this value. The luminescence was from 50 Å $In_{0.2}Ga_{0.8}As$ quantum wells in a P-i-N LED structure.

[35] W.-S. Lee, "Thin Barrier Type AlGaAs/GaAs Heterojunction Bipolar Transistor Structure with Reduced Surface Effects," Ph. D. thesis, Department of Electrical Engineering, Stanford University, pp. 120-2, 1990.

[36] K.D. Choquette, N. Tabatabaie, and R.E. Leibenguth, "Detector-Enclosed Vertical-Cavity Surface Emitting Lasers," Electronics Letters, Vol. 29, No. 5, pp. 466-7, 1993.

[37] S. Adachi, "GaAs, AlAs and $Al_xGa_{1-x}As$: Material parameters for use in research and device applications." Journal of Applied Physics, Vol. 58, No. 3, pp. R1-R28, 1985.

[38] D. Arnold, A. Ketterson, T. Henderson, J. Klem, and H. Morkoç, "Electrical characterization of GaAs/AlGaAs semiconductor-insulator-semiconductor capacitors and application to the measurement of the GaAs/AlGaAs band-gap discontinuity," Journal of Applied Physics, Vol. 57, No. 8, pp. 2880-5, 1985.

[39] G.W. Yoffe, "Rectification in heavily doped p-type GaAs/AlAs heterojunctions," Journal of Applied Physics, Vol. 70, No. 2, pp. 1081-3, 1991.

[40] R.F. Kopf, E.F. Schubert, S.W. Downey, and A.B. Emerson, "N- and P-type dopant profiles in distributed Bragg reflector structures and their effect on resistance," Applied Physics Letters, Vol. 61, No. 15, pp.1820-2, 1992.

[41] Y.H. Wang, G. Hasnain, K. Tai, J.D. Wynn, B.E. Weir, N.K. Dutta, and A.Y. Cho, "Molecular beam epitaxy growth of high performance AlGaAs/GaAs quantum well top emitting lasers," Journal of Vacuum Science and Technology B, Vol. 10, No. 2, pp. 1002-5, 1992.

[42] M. Kawabe, M. Kondo, N. Matsuura, and K. Yamamoto, "Photoluminescence of $Al_xGa_{1-x}As/Al_yGa_{1-y}As$ Multigunatum [sic] Wells Grown by Pulsed Molecular Beam Epitaxy," Japanese Journal of Applied Physics, Vol. 22, No. 2, pp. L64-6, 1983.

[43] D.L. Mathine, G.N. Maracas, D.S. Gerber, R. Droopad, R.J. Gram, and M.R. McCartney, "Characterization of an AlGaAs/GaAs asymetric triangular quantum well grown by a digiatal alloy approximation," Journal of Applied Physics, Vol. 75, No. 9, pp. 4551-6, 1994.

[44] S.Y. Chou and J.S. Harris, Jr., "Room-temperature observation of resonant tunneling through an AlGaAs/GaAs quasiparabolic quantum well grown by molecular beam epitaxy," Applied Physics Letters, Vol. 52, No. 17, pp. 1422-4, 1988.

[45] S.A. Chalmers, K.L. Lear, and K.P. Killeen, "Low resistance wavelength-reproduccible p-type (Al,Ga)As distributed Bragg reflectors grown by molecular beam epitaxy," Applied Physics Letters, Vol. 62, No. 14, pp. 1585-87, 1993.

[46] K.L. Lear, R.P. Schneider, Jr., S.P. Kilcoyne, J.J. Figiel, "Mirror designs for low-voltage vertical-cavity surface-emitting lasers by metalorganic vapor phase epitaxy," Conference on Lasers and Electro-Optics, CM14, 1994.

[47] M. Sugimoto, H. Kosaka, K. Kurihara, I. Ogura, T. Numai, and K. Kasahara, "Very Low Thrshold Current Density in Vertical-Cavity Surface-Emitting Laser Diodes with Periodically Doped Distributed Bragg Reflectors," Electronics Letters, Vol. 28, No. 4, pp. 384-7, 1992.

[48] G.W. Yoffe, "Rectification in heavily doped p-type GaAs/AlAs heterojunctions," Journal of Applied Physics, Vol. 70, No. 2, pp. 1081-3, 1991.

[49] M.G. Peters, B.J. Thibeault, D.B. Young, J.W. Scott, F.H. Peters, A.C. Gossard, and L.A. Coldren, "Band-gap engineered digital alloy interfaces for lower resistance vertical-cavity surface-emitting lasers," Applied Physics Letters, Vol. 63, No. 25, pp. 3411-13 1993.

[50] E.F. Schubert, L.W. Tu, G.J. Zydzik, R.F. Kopf, A. Benvenuti, and M.R. Pinto, "Elimination of heterojunction band discontinuities by modulation doping," Applied Physics Letters, Vol. 60, No. 4, pp. 466-68, 1992.

[51] M. Sundaram, A.C. Gossard, and P.O. Holtz, Modulation doped graded structures: Growth and characterization," Journal of Applied Physics, Vol. 69, No. 4, pp. 2370-5, 1991.

[52] A. Fischer and K.H. Ploog, "Heavy Carbon Doping of AlAs by Elemental-Source Molecular Beam Epitaxy," Applied Physics A, Vol. 57, pp. 217-19, 1993.

[53] H. Ito, O. Nakajima, and T. Ishibashi, "Carbon doping for AlGaAs/GaAs heterojunction bipolar transistors by molecular-beam epitaxy," Applied Physics Letters, Vol. 62, No. 17, pp. 2099-101, 1998.

[54] M. Micovic, P. Evalsson, M. Geva, G.W. Taylor, Vang, and R.J. Malik, "Quantum well lasers with carbon doped cladding layers grown by solid source molecular beam epitaxy," Applied Physics Letters, Vol. 64, No. 4, pp. 411-3, 1994.

[55] H.H. Berger, "Models for Contacts to Planar Devices," Solid-State Electronics, Vol. 15, pp. 145-58, 1972.

[56] K.I. Lear and S.A. Chalmers, "High Single-Mode Power Conversion Efficiency Vertical-Cavity Top-Surface-Emitting Lasers," IEEE Photonics Technology Letters, Vol. 5, No. 9, pp. 972-5, 1993

[57] R.S. Geels, S.W. Corzine, and L.A. Coldren, "InGaAs Vertical-Cavity Surface-Emitting Lasers," IEEE Journal of Quantum Electronics, Vol. 27, No. 6, pp. 1359-67, 1991.

[58] H.C. Casey and M.B. Panish, Jr. , "Heterostructure Lasers, Part A: Fundamental Principles," (San Diego, California: Academic Press, 1978), pp. 175.

[59] K. Tai, Y. Lai, K.F. Huang, T.C. Huang, T.D. Lee, and C.C. Wu, "Transverse more emission characteristics of gain-guided surface emitting lasers," Applied Physics Letters, Vol. 63, No. 19, pp. 2624-6, 1993.

[60] K.L. Lear, S.P. Kilcoyne, and S.A. Chalmers, "High Power Conversion Efficiencies and Scalling Issues for Multimode Vertical-Cavity Top-Surface-Emitting Lasers," EE Photonics Technology Letters, Vol. 6, No. 7, pp. 778-80, 1994.

[61] T.G. Dziura, Y.J. Yang, R. Fernandez, and S.C. Wang, "5Ghz modulation of a mushroom mesa surface emitting laser," Applied Physics Letters, Vol. 59, No. 10, pp.1147-9, 1991.

[62] A. Scherer, J.L. Jewell, M. Walther, J. P. Harbison, and L.T. Florez, "Fabrication of Low Threshol Voltage Microlasers," Electronics Letters, Vol. 28, No. 13, pp.1224-6, 1992.

[63] This work, section 4.3, and reference 46.

[64] M. Tong, D.G. Ballegeer, A. Ketterson, E.J. Roan, K.Y. Cheng, and I. Adesida, "A Comparitive Study of Wet and Dry Selective Etching Processes for GaAs/AlGaAs/InGaAs Pseudomorphic MODFETs," J. Of Electronic Materials, Vol. 21, No. 1, pp. 9-15, 1992.

[65] Y. Mori and N. Watanabe, "A New Etching Solution System, H_3PO_4 : H_2O_2 : H_2O, for GaAs and Its Kinetics," Journal of the Electrochemical Society, Vol. 125, No. 9, pp. 1510-1514, 1978.

[66] R.E. Williams, *Gallium Arsenide Processing Techniques*, (Dedham, Massachusetts: Artec House, 1984), pp. 102-103.

[67] E. Yablonovitch, T. Gmitter, J.P. Harbison, and R. Bhat, "Extreme selectivity in the lift-off of epitaxial GaAs films," Applied Physics Letters, Vol. 51, No. 26, pp. 2222-24, 1987.

[68] W.P. Dumke, J.M. Woodall, and V.L. Rideout, GaAs-GaAlAs Heterojunction Transistor for High Frequency Operation," Solid-State Electronics, Vol. 15, pp. 1339-43, 1972.

[69] S.M. Sze, *Physics of Semiconductor Devices*, (New York, New York: John Wiley & Sons, 1981), pp. 29.

[70] Optical simulations of a mirror with a 5/4 wavelength contact layer doped as in the test devices indicate that it should have about 1/3 the free-carrier absorption of the p-type mirror #2 from section 4.3.4. This is a consequence of the lower free-carrier absorption for electrons and mostly undoped mirror.

[71] D.L. Huffaker, D.G. Deppe, K. Kumar, and T.J. Rogers, "Native-oxide defined ring contact for low treshold vertical-cavity lasers," Applied Physics Letters, Vol. 65, No. 1, pp. 97-9, 1994.

[72] K.D. Choquette, R.P. Schneider, Jr., K.L. Lear, and K.M. Geib, "Low threshold voltage vertical-cavity lasers fabricated by selective oxidation," Electronics Letters, Vol. 30, No. 24, pp. 2043-4, 1994.

[73] J.M. Dallesasse and N. Holonyak, Jr., "Native-oxide stripe-geometry $Al_xGa_{1-x}As$-GaAs quantum well heterostructure lasers," Applied Physics Letters, Vol. 58, No. 4, pp. 394-6, 1991.

[74] M. MacDougal, P.D. Dapkus, V. Pudikov, H. Zhao, and G.M. Yang, "Ultralow Threshold Current Vertical-Cavity Surface-Emitting Lasers with AlAs Oxide-GaAs Distributed Bragg Reflectors," IEEE Photonics Technology Letters, Vol. 7, No. 3, pp. 229-31, 1995.

[75] J.P.A. van der Wagt, "Reflection High-Energy Electron Diffraction During Molecular-Beam Epitaxy," Ph. D. thesis, Department of Applied Physics, Stanford University, pp. 71, 1994.

[76] E.S. Hellman and J.S. Harris, Jr., Infra-red Transmission Spectroscopy of GaAs During Molecular Beam Epitaxy," Journal of Crystal Growth, Vol. 81, pp. 38-42, 1987

[77] W.-S. Lee, "Thin Barrier Type AlGaAs/GaAs Heterojunction Bipolar Transistor Structure with Reduced Surface Effects," Ph. D. thesis, Department of Electrical Engineering, Stanford University, pp. 107-120, 1990.